

**GENCORP  
AEROJET**

1

**AD-A231 935**

**DEVELOPMENT OF LIFE PREDICTION  
CAPABILITIES  
FOR LIQUID PROPELLANT ROCKET ENGINES**

**TASK 2.0  
ENGINE THROAT/NOZZLE OPTICS FOR PLUME SPECTROSCOPY**

**Contract NAS 3-25883**

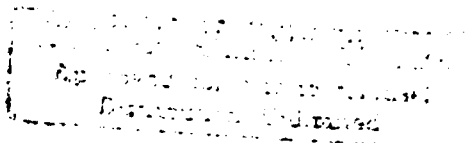
\*Original contains color  
plates: All DTIC reproductions  
will be in black and  
white\*

**FINAL REPORT**

**DTIC  
ELECTE  
FEB 22 1991**

**Prepared for: National Aeronautics and Space Administration  
Lewis Research Center, MS 500-219  
21000 Brookpark Road  
Cleveland, OH 44135**

**Submitted by: Aerojet Propulsion Division  
P.O. Box 13222  
Sacramento, CA 95813-6000**



**1 February 1991**

**Propulsion Division**

**91 2 13 095**

## EXECUTIVE SUMMARY

The Task 2.0, Engine Throat/Nozzle Optics for Plume Spectroscopy, effort was performed under the NASA LeRC Development of Life Prediction Capabilities for Liquid Propellant Rocket Engines program. This Task produced the engineering design of an optical probe to enable spectroscopy measurements within the SSME main chamber. The probe mounts on the SSME nozzle aft manifold and collects light emitted from the throat plane and chamber. Light collected by the probe is transferred to a spectrometer through a fiberoptic cable. The design analyses indicate that the probe will function throughout the engine operating cycle and is suitable for both test stand and flight operations. By detecting metallic emissions that are indicative of component degradation or incipient failure, engine shutdown can be initiated before catastrophic failure. This capability will protect valuable test stand hardware and provide enhanced mission safety.

*25 \* Liquid propellant rocket  
engines - throat/nozzle optics*



Accession For	
NTIS	CRA&I <input checked="" type="checkbox"/>
DTIC	TAB <input type="checkbox"/>
Unannounced <input type="checkbox"/>	
Justification	
By	
Distribution /	
Availability Codes	
Dist	Avail and/or Special
A-1	

## TABLE OF CONTENTS

	<u>Page</u>
1.0 INTRODUCTION .....	1
2.0 TECHNICAL DISCUSSION .....	2
2.1 Subtask 1: Feasibility and Requirements Analysis .....	2
2.1.1 Subtask 1.1 Optical Requirements .....	2
2.1.2 Subtask 1.2 Environmental Analysis .....	21
2.1.3 Subtask 1.3 Interface to Spectrometers .....	27
2.1.4 Subtask 1.4 Conceptual Designs .....	31
2.1.5 Subtask 1.5 Baseline Design Selection .....	34
2.2 Subtask 2: Design and Analysis .....	36
2.2.1 Subtask 2.1 Flowfield and Heat Transfer Analysis .....	36
2.2.2 Subtask 2.2 Optical Design .....	40
2.2.3 Subtask 2.3 Hardware Configuration .....	43
2.2.4 Subtask 2.4 Engine Throat/Nozzle Optic Analysis .....	51
2.2.5 Subtask 2.5 Spectrometer Interface .....	72
2.2.6 Subtask 2.6 Alignment System .....	73
2.3 Subtask 3: Development Plan for Fabrication & Testing .....	74
2.3.1 Nozzle Optic Fabrication and Check-Out .....	74
2.3.2 Test Stand Instrumentation Packaging Design (Optional) ....	78
2.3.3 Test Stand Design Review and Approvals .....	79
2.3.4 Test Stand Instrumentation Procurement, Assembly, and Inspection .....	79
2.3.5 TTBE Nozzle Optic Testing .....	80
3.0 CONCLUSIONS .....	80
4.0 RECOMMENDATIONS .....	81

## FIGURES

<u>Number</u>		<u>Page</u>
1.	Engine Optic Mounts to the Aft Manifold and Collects Light Emitted Through the Throat Plane into a Fiberoptic Cable . . . . .	1
2.	Analysis Steps used to Determine Engine Optic Aperture Size . . . . .	4
3.	Temperature Profile as a Function of Axial Position Within the SSME . . . . .	5
4.	Density Profile as a Function of Axial Position Within the SSME . . . . .	5
5.	Radiant Power Density Profile Along the Axis of the SSME . . . . .	6
6.	Pressure Broadened and Shifted Emission Line is not Concurrent with Low Pressure Emission Lines . . . . .	10
7.	OH Mass Fraction Variation along the SSME Axis . . . . .	11
8.	Approximate Spectra from Hydrogen/Oxygen Combustion Products within the SSME. . . . .	12
9.	Approximate Refractive Index of the Plume Gas vs. Radial Position within the SSME . . . . .	15
10.	Ray Deflection through SSME Nozzle Barrel Shock as a Function of Incident Angle . . . . .	15
11.	Field-of-View for the Engine Optic Looking at the Throat Plane . . . . .	16
12.	Ray Trace of 2.5-mm Lens with 0.8-mm Diameter Fiberoptic Cable . . . . .	18
13.	Ray Trace of a 6-mm Diameter Lens Showing a 0.8-mm diameter Spot formed on a 1.6-mm Diameter Fiber Bundle . . . . .	19
14.	Diode Signal-to-Noise Ratio as a Function of Aperture Diameter . . . . .	20
15.	Pressure Field in SSME Plume at Sea Level Conditions . . . . .	22
16.	Temperature Field in SSME Plume at Sea Level Conditions . . . . .	23
17.	Power Spectral Density for the SSME Nozzle . . . . .	25
18.	Transient Acceleration Spectra for SSME Nozzle . . . . .	25
19.	Acoustic Pressure Level Near SSME Nozzle . . . . .	26
20.	Fiberoptic Cable will be Attached to a Drain Line . . . . .	28
21.	Drain line locations relative to SLAM holes. . . . .	29
22.	The Engine Optic Mounts to Two SLAM Holes on the Aft Manifold Between the Drain Line and Hydrogen Downcomer, and the Fiberoptic Cable is Anchored to the Drain Line . . . . .	30
23.	Recommended Subtask 1.4 Conceptual Design . . . . .	32
24.	Alternative Subtask 1.4 Design Concepts Illustrated . . . . .	33
25.	Anchoring Approaches for Attaching Probe to Aft Manifold . . . . .	34
26.	Nozzle Optic is Outside the Compression Shock Boundary . . . . .	36
27.	Prandtl-Meyer Expansion Flow of SSME Nozzle at High Altitude . . . . .	39
28.	Ray Traces of Lens at Tolerance Limits . . . . .	41

## FIGURES (cont.)

<u>Number</u>	<u>Page</u>
29. Trace of Marginal Rays for 300 and 700 nm .....	42
30. Angular Rotation Caused by Differential Expansion at Various Locations on the Probe .....	42
31. Field-of-View Shift From Aft Manifold Distortion During Start Transient ....	44
32. 6101 T6 Aluminum Engine Optic Design .....	45
33. ZrCu Engine Optic Design .....	46
34. Fiberoptic Cable Dimensions and Specifications .....	48
35. Objective Lens Dimensions and Specifications .....	49
36. Peak Temperature, Weight, and Maximum Bending Stress as a Function of Cross Section Width for an Aluminum Probe .....	53
37. Peak Temperature, Weight, and Maximum Bending Stress as a Function of Cross Section Width for a Copper Probe .....	54
38. Convective Heat Transfer Coefficient Boundary Conditions used in Finite Element Analyses .....	55
39. Steady State Temperature Contours for the Aluminum Probe with Maximum Contact Area .....	57
40. Steady State Temperature Contours for the Copper Probe with Maximum Contact Area .....	58
41. Steady State Temperature Contours for the Aluminum Probe with Contact Limited to Bolt Region .....	59
42. Steady State Temperature Contours for the Copper Probe with Contact Limited to the Bolt Region .....	60
43. Optic Probe Transient Temperature Response for Site with Maximum Protrusion into the Flowfield .....	61
44. Thermal/Stresses in the Aft Manifold Resulting from the Probe Thermal Load .....	63
45. Bending Stresses in Copper Probe Resulting from 7500-g Static Acceleration .....	64
46. Bending Stresses in Aluminum Probe Resulting from 7500-g Static Acceleration .....	65
47. Stresses from Aluminum Probe Random Vibration .....	68
48. Stresses from Copper Probe Random Vibration .....	69
49. HeNe Laser Backlights Optic System to Check Probe Alignment .....	73
50. TTB Engine Nozzle Optic Demonstration .....	75

## TABLES

<u>Number</u>		<u>Page</u>
1.	Emission Properties of Metallic Species at SSME Chamber Operating Conditions for 1-ppm Concentration . . . . .	8
2.	Atomic Emission Flux Arriving at the Engine Optic from Metal Species Entrained in the Flowfield at the Minimum Detectability Limit Concentration . . . . .	9
3.	Comparison of Design Features for Recommended and Alternate Engine Optic Designs . . . . .	35
4.	Heat Transfer Coefficients Calculated for the Engine Optic Interacting with the SSME Plume Flowfield . . . . .	37
5.	Comparison of Zirconium-Copper and 6101 T6 Aluminum Thermal and Mechanical Properties . . . . .	50
6.	Natural Frequencies for Aluminum Probe . . . . .	66
7.	Natural Frequencies for Copper Probe . . . . .	66
8.	Stresses in the Aft Manifold Resulting from Various Loads . . . . .	70
9.	Comparison of Operational Properties for the 6101 Aluminum and Zr-Cu Designs . . . . .	72

## 1.0 INTRODUCTION

This report describes work performed under Task 2 of the Development of Life Prediction Capabilities for Liquid Propellant Rocket Engines program. Task 2 encompassed the engineering design for an optical probe to monitor spectral emissions originating in the SSME chamber. The probe mounts on the SSME aft manifold, collecting and focusing light into a fiberoptic cable which transports the light to a spectrometer. Figure 1 shows the engine optic mounted onto the SSME aft manifold and the throat plane field-of-view.

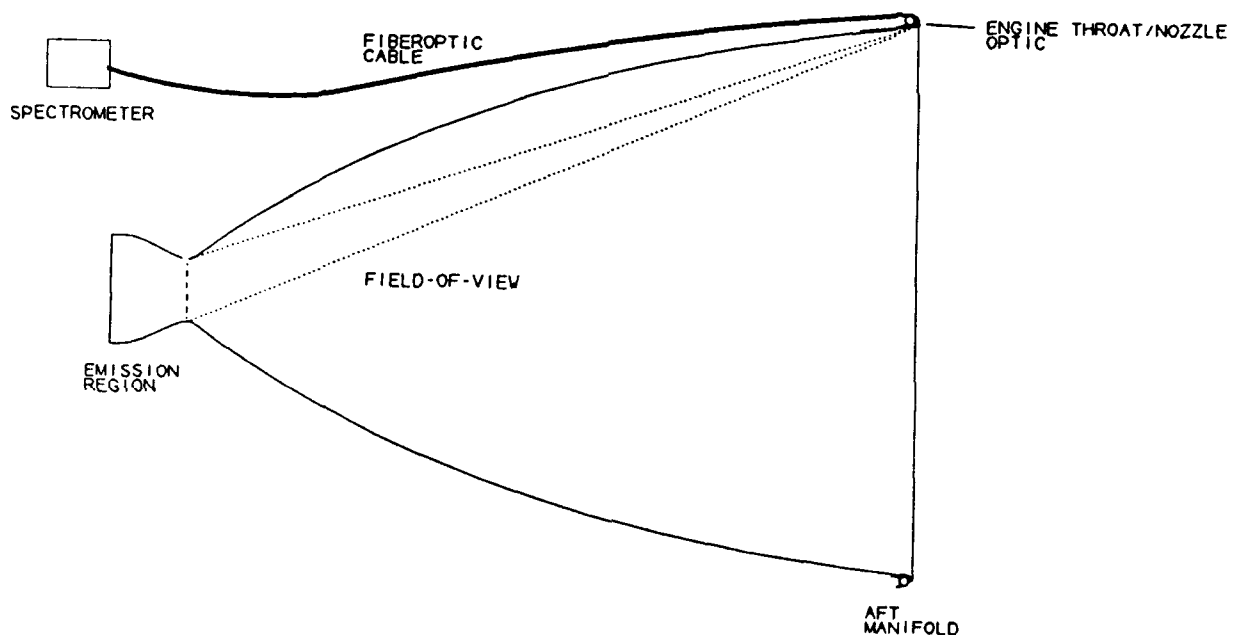


Figure 1. Engine Optic Mounts to the Aft Manifold and Collects Light Emitted Through the Throat Plane into a Fiberoptic Cable.

Visible emissions have been observed in plume flows prior to catastrophic failures within SSME engines. These emissions were caused by thermally excited metal atoms that were entrained in the hot plume gases. Subsequent measurements on the SSME and the Diagnostic Test Facility (DTF) engine have demonstrated that metal specie emissions can be detected electronically using spectrometers observing the plume Mach disc.

Spectral monitoring of external plume emissions can be effective for open air, sea level test stands. External plume emissions are difficult to observe when the engine exhausts

into a diffuser or at high altitudes where the high temperature Mach structure does not exist. Engine test stand qualification and optical flight instrumentation will require a method of monitoring emissions without depending on the Mach structure.

This program has supported the feasibility analysis and engineering design of an optical probe which can be retrofitted to the SSME. The probe will image the throat plane and collect light emitted from within the combustion chamber. This approach for optical monitoring is independent of the external plume characteristics so operation can be achieved on diffuser test stands and with the engine exhausting to a variable backpressure or vacuum.

## **2.0 TECHNICAL DISCUSSION**

The engineering design efforts performed during Task 2 are described in the following sections. Task 2 consisted of three subtasks, a feasibility and requirements analysis, detailed design and analysis, and developing recommendations for fabrication and testing of the design.

### **2.1 Subtask 1: Feasibility and Requirements Analysis**

The optical and environmental operating requirements were defined for an optical probe used to collect light emitted from the chamber, through the throat plane.

#### **2.1.1 Subtask 1.1 Optical Requirements**

The system optical requirements were defined in this subtask. The location, shape, and size of the window aperture were defined. Analyses were performed for the engine emission characteristics, losses and optical performance of the probe and fiberoptic cable, and the input requirements for spectrometers. The results were used to size the optic system.

In defining the optical requirements, the goal was to determine the minimum size optics required to transfer an adequate signal to a spectrometer. Oversizing the optics results in a larger probe which imparts excessive mechanical and thermal loads into the aft manifold. To size the optics, the minimum detectability requirements for the spectrometer must be known so that the minimum required light delivered through the optics can be calculated. Knowledge of the flux arriving at the objective lens from chamber emissions is also required. The objective lens size can then be calculated using the available flux into the optics, required intensity into the spectrometer, and losses in



the objective lens and fiberoptic cable. The design and analysis steps used to size the engine optic are illustrated in Figure 2. The key aspects of the optic sizing are described in the following sections after which a rationale for the objective lens diameter selection is provided.

Where possible the engine spectroscopy and system optics performance has been addressed quantitatively. Quantification is feasible for atomic emissions from metallic species, line shape and shift, transport optics performance, and spectrometer performance. The primary uncertainty lies in determination of the spectral background radiation intensity. A qualitative discussion is provided to suggest scaling trends that might be observed for plume measurements.

### Chamber Operating Conditions

The SSME combustion chamber operates at 205 atmospheres during 109% power conditions with a mixture ratio of 6:1. The engine is overexpanded at sea level and underexpanded in space. TDK runs, performed by AEDC, were used to produce temperature and density profiles shown in Figures 3 and 4 that start at the injector face and end at the nozzle exit.

The radiant power density was calculated for the chromium 425.4-nm line at a 1-ppm concentration using the TDK temperature and density profiles as shown in Figures 3 and 4. To account for oxide depletion of the atomic population, a beta term of 0.33 used, which describes the percentage of chrome atoms existing in an atomic state. This value from Handbook of Flame Spectroscopy by Parsons[1] is approximate since it applies to specific analytical O/H flame condition which is fuel rich, but not the same mixture ratio as the SSME nor the same pressure and temperature. A more comprehensive assessment of the kinetics would be required to further quantify beta term. The methods used to calculate radiate power density have been previously described in Reference [2].

For calculation of specie emission intensities, the combustion chamber gas is assumed to be optically thin. This assumption is valid at low atomic specie concentrations. Some self-absorption will occur at higher concentrations. Due the wide line widths existing at 205 atmospheres, self-absorption will be far less significant than for the same specie atom densities at atmospheric pressure.



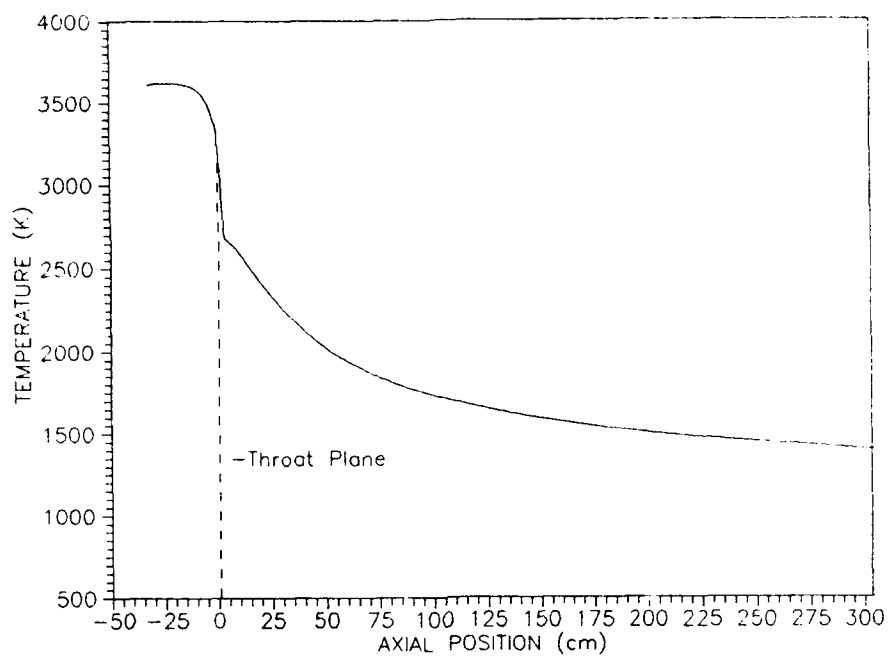


Figure 3. Temperature Profile as a Function of Axial Position Within the SSME.

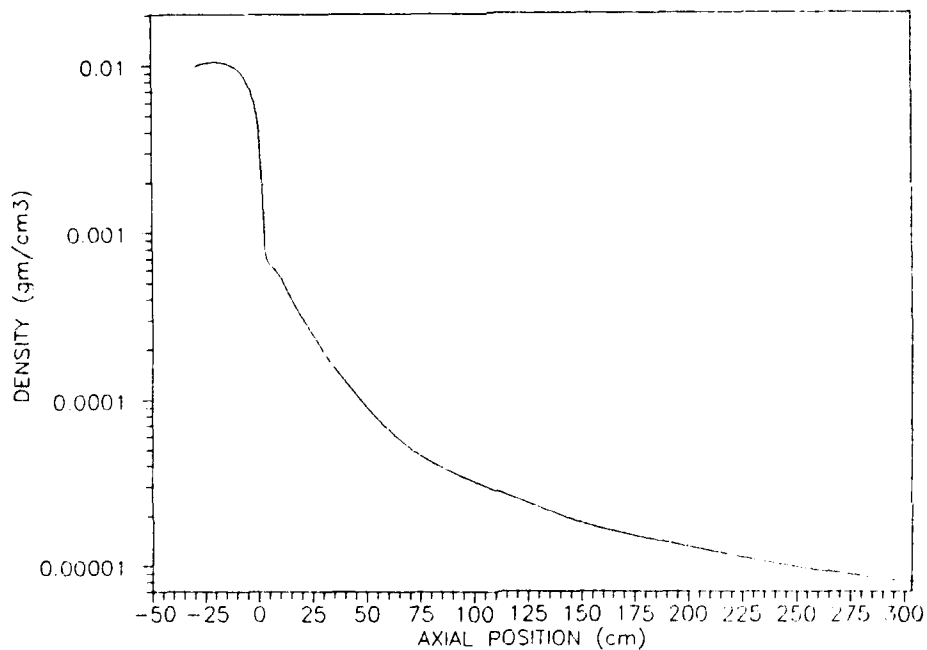


Figure 4. Density Profile as a Function of Axial Position Within the SSME.

The radiant power density profile shown in Figure 5 can be linearly scaled up or down for any specie concentration up to the point where self-absorption becomes significant. The basic shape applies to other metal species. The ratio of the amplitude within the chamber to the amplitude in the expansion region will be greater for shorter wavelength lines and smaller for longer wavelength lines due to the temperature dependence in the exponential term of the thermal emission equation.

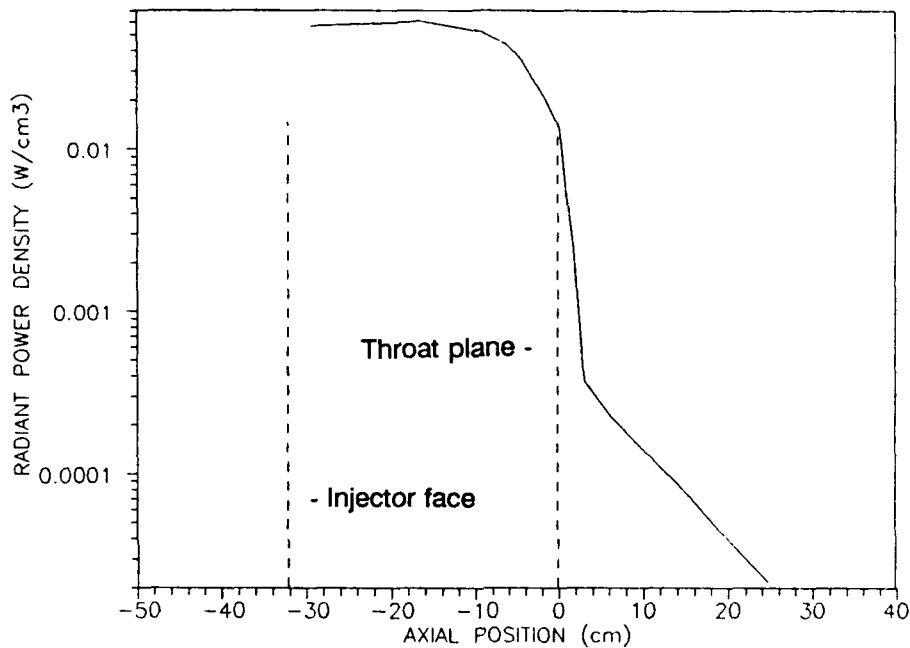


Figure 5. Radiant Power Density Profile Along the Axis of the SSME.

As shown in Figure 5, the radiant power density is constant within the combustion chamber up to the entrance region to the throat. Radiant power density decreases as the gas accelerates and both density and static temperature decrease. At the throat minimum, radiant power density has dropped a factor of 3. Radiant power density drops by a factor of 150 only three centimeters downstream of the throat.

Radiation in the expansion region is insignificant relative to the chamber. Erosion at or downstream of the throat will supply limited emissions since density and temperature are rapidly decreasing in the expansion region. Thus, emission spectroscopy is most suited to detection of metal species passing through the combustion chamber, not to copper eroded from the throat region.

SSME chamber pressure, volume, specie density at 1-ppm, and an analytical flame beta term were used to calculate the radiation terms in Table 1. A geometric shape factor of 0.7 was used to approximate the shadowing effects for chamber emissions due to the throat when calculating the flux arriving into optics at the nozzle lip. The chamber and expansion region flows were assumed to be optically thin. Reflections within the chamber were ignored which underestimates the fluxes. The steps used to calculate terms in Table 1 were: 1) calculate specie density by first calculating the mass density at 1 ppm and then calculating the metallic specie population per unit volume, 2) calculating radiation per particle at chamber temperature assuming thermal excitation is the dominate mechanism, 3) multiplying specie density and particle radiation together to obtain radiant power density, 4) multiplying radiant power density times the chamber volume to obtain radiant power, and 5) calculating flux using radiant power divided by the area of a sphere having a radius equal to the distance from the chamber to the nozzle lip.

The radiant power density within the chamber is 600-1000 times greater than the high temperature subsonic region downstream from the Mach disc. The total radiant power is 27-40 times greater, providing a brighter source for emission spectroscopy. The flux arriving at the foreoptic is 6-11 times greater looking into the engine than that emitted from the plume.

Table 2 shows the fluxes arriving at an optic mounted on the aft manifold for each atomic specie. These values are for atomic emissions at the minimum detectability limit concentration. Both the chamber and Mach disc fluxes are shown for comparison. Note that the MDL for the chamber and Mach disc are assumed to be constant, e.g, the relationship between atomic emission intensity and background radiation is invariant at a given specie concentration for both the chamber and Mach disc. The flux values shown in the fifth column of Table 2 were used in the signal-to-noise ratio calculations for selection of the engine optic aperture size.

The Mach disc plume emission region matches the field-of-view of a fused silica fiber so simple lenses do not increase the useful flux arriving at the fiber. The throat is much smaller than a fused silica fiber field-of-view so a lens can be used to increase the useful flux. If the fiber field-of-view is matched to the throat radius, the useful optical signal arriving in the fiber is 200-400 times greater than is obtained by looking at the Mach disc region from the nozzle lip.

Table 1. Emission Properties of Metallic Species at SSME Chamber Operating Conditions for 1-ppm Concentration.

Specie	Wave-length (nm)	Specie Density (pt./cm <sup>3</sup> )	Particle Radiation (uW/atom)	Radiant Power Density (w/cm <sup>3</sup> )	Radiant Power (watts)	Flux at Optic (W/cm <sup>2</sup> )	Line- width (nm)
Al	396.2	1.8E+10	7.4E-10	1.3E-05	0.44	1.96E-07	0.4
Ba	553.5	2.3E+11	7.9E-08	1.8E-02	579	2.59E-04	0.7
Cd	326.1	2.0E+13	3.9E-12	7.9E-05	3	1.15E-06	0.2
Ca	422.7	2.3E+13	2.6E-08	6.1E-01	19665	8.79E-03	0.5
Cr	357.9	3.7E+13	1.5E-09	5.5E-02	1802	8.05E-04	0.3
	359.3	3.7E+13	1.2E-09	4.6E-02	1480	6.62E-04	0.2
	425.4	3.7E+13	1.6E-09	5.8E-02	1870	8.36E-04	0.4
	427.5	3.7E+13	1.2E-09	4.5E-02	1470	6.57E-04	0.4
	429.0	3.7E+13	9.2E-10	3.4E-02	1106	4.94E-04	0.4
Co	345.4	2.2E+13	1.6E-10	3.5E-03	115	5.14E-05	0.3
	352.7	2.2E+13	3.7E-11	8.1E-04	26	1.17E-05	0.3
Cu	324.8	9.3E+13	8.4E-10	7.9E-02	2562	1.15E-03	0.2
	327.4	9.3E+13	4.6E-10	4.3E-02	1382	6.18E-04	0.2
Au	267.6	1.7E+13	4.7E-11	8.0E-04	26	1.16E-05	0.2
In	451.1	5.8E+13	1.7E-09	9.8E-02	3176	1.42E-03	0.5
Ir	351.4	3.2E+12	4.9E-11	1.6E-04	5	2.30E-06	0.2
Fe	372.0	9.1E+13	8.8E-11	8.0E-03	258	1.16E-04	0.3
	373.7	9.1E+13	6.4E-11	5.9E-03	190	8.50E-05	0.3
	386.0	9.1E+13	9.6E-11	8.7E-03	282	1.26E-04	0.4
Mg	285.2	1.7E+14	9.6E-10	1.6E-01	5162	2.31E-03	0.2
Mn	279.5	8.4E+13	2.5E-10	2.1E-02	672	3.01E-04	0.2
	403.1	8.4E+13	6.7E-10	5.7E-02	1845	8.25E-04	0.4
	403.3	8.4E+13	4.8E-10	4.1E-02	1318	5.89E-04	0.4
Mo	379.8	1.9E+12	9.6E-10	1.8E-03	60	2.68E-05	0.3
Ni	341.5	1.1E+14	6.0E-11	6.3E-03	206	9.21E-05	0.3
	352.5	1.1E+14	1.2E-10	1.3E-02	408	1.82E-04	0.3
Pd	340.5	5.8E+13	4.2E-10	2.4E-02	787	3.52E-04	0.2
	363.5	5.8E+13	4.2E-10	2.5E-02	797	3.56E-04	0.3
K	766.5	6.3E+13	1.1E-07	7.2E+00	232948	1.04E-01	1.5
	769.9	6.3E+13	5.7E-08	3.6E+00	117121	5.24E-02	1.5
Ag	328.1	4.9E+13	1.1E-09	5.3E-02	1715	7.67E-04	0.2
	338.3	4.9E+13	6.3E-10	3.1E-02	992	4.43E-04	0.2
Na	589.0	2.8E+14	5.1E-08	1.4E+01	469490	2.10E-01	1.0
	589.6	2.8E+14	2.5E-08	7.1E+00	232333	1.04E-01	1.0
Sr	460.7	1.2E+13	4.7E-08	5.7E-01	18482	8.26E-03	0.5
Sn	380.1	2.0E+13	1.3E-11	2.5E-04	8.2	3.66E-06	0.0
Ti	365.4	2.6E+11	3.2E-10	8.2E-05	2.7	1.19E-06	0.3
	399.9	2.6E+11	3.6E-10	9.2E-05	3.0	1.34E-06	0.4
W	400.9	2.4E+13	2.3E-10	5.4E-03	175	7.81E-05	0.4
V	437.9	2.2E+12	8.5E-10	1.9E-03	60	2.69E-05	0.5

Table 2. Atomic Emission Flux Arriving at the Engine Optic from Metal Species Entrained in the Flowfield at the Minimum Detectability Limit Concentration.

	Wave-length (nm)	Detect Limit (ppm)	Line- width (nm)	Flux arriving at optic foreoptic:	
				Chamber (W/cm <sup>2</sup> )	Mach Disc (W/cm <sup>2</sup> )
Ca	422.7	0.0023	0.5	2.1E-05	3.4E-06
Cr	357.9	0.0623	0.3	5.0E-05	5.8E-06
	425.4	0.0244	0.4	2.0E-05	3.4E-06
Co	345.4	1.4254	0.3	7.3E-05	5.8E-06
Cu	324.8	0.1081	0.2	1.2E-04	1.1E-05
	327.4	0.1486	0.2	9.2E-05	8.6E-06
Fe	372.0	0.3041	0.3	3.5E-05	4.5E-06
	386.0	0.2564	0.4	3.2E-05	4.5E-06
Mn	403.1	0.0330	0.4	2.7E-05	4.1E-06
Mo	379.8	1.1530	0.3	3.1E-05	4.1E-06
Ni	352.5	0.3418	0.3	6.2E-05	6.9E-06
Pd	363.5	0.1941	0.3	6.9E-05	4.8E-06
K	766.5	0.0001	1.5	1.4E-05	5.8E-06
	769.9	0.0003	1.5	1.4E-05	5.8E-06
Ag	328.1	0.1191	0.2	9.1E-05	8.6E-06
	338.3	0.1297	0.2	5.7E-05	5.8E-06
Na	589.0	0.0001	1.0	2.0E-05	5.8E-06
	589.6	0.0002	1.0	2.0E-05	5.8E-06
Sr	460.7	0.0036	0.5	3.0E-05	5.8E-06
Sn	380.1	41.214	0.0	1.5E-04	5.1E-06
Ti	365.4	36.631	0.3	4.4E-05	5.1E-06
W	400.9	0.4522	0.4	3.5E-05	4.1E-06
V	437.9	1.0520	0.5	2.8E-05	4.1E-06

Lorentz broadening of line widths scales linearly with pressure as shown in equation (1)

$$\delta \lambda_c = \frac{2\lambda_o^2 \sigma_c^2 P_f}{\pi c k T} \left[ 2\pi R T \left( \frac{1}{A_f} + \frac{1}{A_r} \right) \right]^{\frac{1}{2}} \quad (1)$$

where  $P_f$  is the pressure,  $\sigma$  is the collision cross section, and  $A_f$  and  $A_r$  are the atomic weights of the metallic specie and plume gas respectively.

At 205 atmospheres, line widths range from 0.2-0.4 nm for metallic species of interest. The spectral intensity decreases proportionally with pressure because of line broadening. This is only important for radiation measurements where the line width is greater than the spectrometer bandwidth. The breadboard Fabry-Perot interferometer will have a bandwidth of approximately 0.03-nm or roughly a factor of ten narrower than the emission

line widths at 205 atmospheres. This decreases the peak intensity observed since only a fraction of the line radiation is observed at any given time. Still, the high resolution will enable operation in a line mapping mode for better signal discrimination than can be gotten using signal amplitude within a fixed bandpass.

Besides broadening spectral lines, pressure also red shifts the emission (and absorption) lines. The amount of red shift and broadening is a function both of the metal specie and gas particle masses. Data on the collision cross sections are required to calculate pressure broadening. Generally the red shift is slightly smaller than the line width. Red shifts of 0.1-0.2 nm will be observed at 205 atmospheres. Red shift of emission lines and line broadening almost totally precludes any absorption by species in the expansion region. The absorption region is a narrow line out in the blue wing of the emission line as shown in Figure 6 (from Reference [3]). Even at high concentrations, absorption will be inconsequential. This is not so in the plume where the absorption and emission lines are coincident and of similar widths.

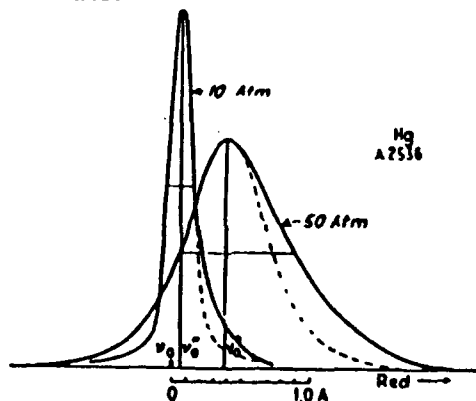


Figure 6. Pressure Broadened and Shifted Emission Line is not Concurrent with Low Pressure Emission Lines.

#### Background radiation

Background radiation can occur from rotation/vibration/electronic transitions forming molecular band radiation and from radiative recombination. Transitions of the OH radical are the primary source of band radiation in the UV range with a minor contribution from transitions of  $O_2$ . At the 3635K chamber operating temperature of the SSME, radiation from thermal excitation will dominate over the chemical reaction induced excitation. The OH radiation intensity will be proportional to the specie concentration and temperature. Figure 7 shows the OH mass fraction at the chamber temperature and pressure is roughly 10% of the OH concentration in the subsonic portion of the plume. This would suggest that background radiation from OH transitions should be lower than metallic specie emissions for the chamber compared to the plume.



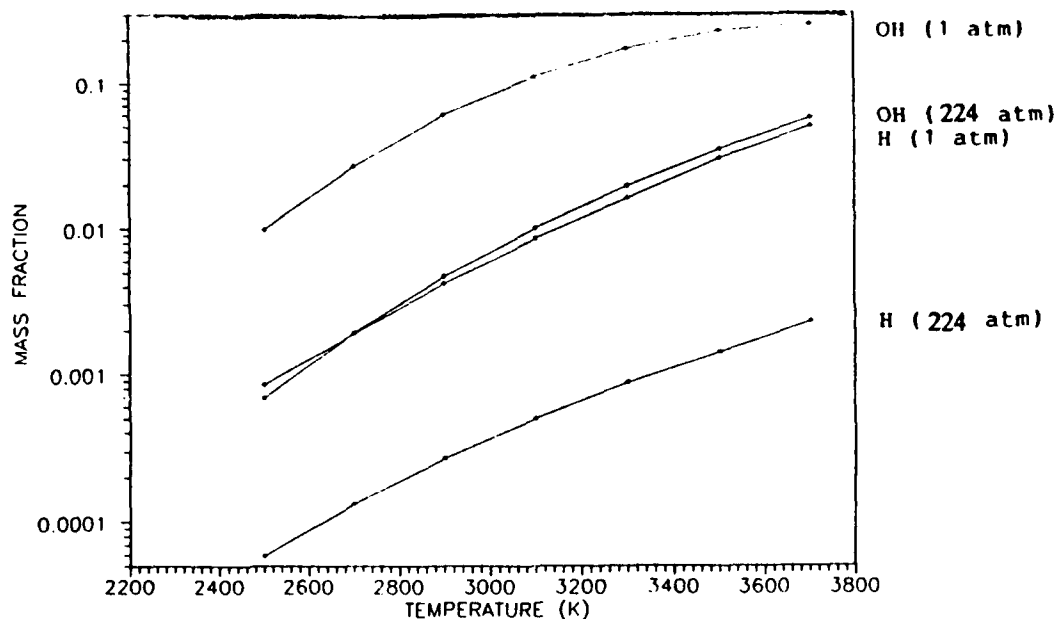


Figure 7. OH Mass Fraction Variation along the SSME Axis.

Like the atomic transitions, the vibration/rotation lines within the 306-nm OH band will be broadened to 0.1-0.2 nm. The spectrum from individual lines will start to overlap causing the band radiation to approach a local continuum. By broadening the electronic vibration/rotation lines, self absorption is significantly decreased. Self-absorption is significant for the 0-0 band of OH for small hydrogen/oxygen flames at atmospheric pressure so the band intensity at 205 atmospheres will be higher relative to an identical population density at the same temperature. However, it is unknown whether the increased signal from reduced self-absorption will be offset by the lower population density that will exist at 205 atmospheres relative to the one atmosphere condition within the plume.

SSME plume measurements made at Stennis and Marshall Spaceflight Centers show high level of radiation from 325-700 nm compared to laboratory hydrogen/oxygen flames. The ratio of the spectral intensity at 306-nm to the intensity in the 300-400 nm range is roughly 10 compared to a ratio of greater than 100 for an analytical flame. Several factors may explain to this observation: 1) self-absorption may be reducing the amplitude of the OH band, 2) an anomalous radiation source may exist, or 3) instrumentation noise may exist.

Self-absorption is almost certainly present but probably not severe because the shape of the band reasonably matches that from an analytical flame measurement. The most likely continuum source would be from the  $\text{OH} + \text{H}$  reaction described by Padley[4]. This radiative recombination reaction is frequently referenced in the literature. Experiments by Dean[5] and Zeegers[6] cast doubts on the spectral importance of this reaction since they were unable to measure any continuum at substantially higher H and OH concentrations than existed in Padley's experiments. Instrumentation noise may result from background radiation from surrounding light sources or from out-of-band radiation scattered within the OMAs used to make the measurements. Estimates of the stray light signal from the 900-1050 nm  $\text{H}_2\text{O}$  radiation using data from similar spectrometers suggests much of the measured signal could be due to stray light.

The SSME plume has large regions where temperatures are adequate to excite the near IR  $\text{H}_2\text{O}$  bands between 900 and 1050-nm. Atomic transitions are excited only in small, high temperature regions, therefore, the SSME plume will exhibit a much greater ratio of near IR to UV radiation relative to analytical flames. The high level of near IR in the SSME plume will increase measurement errors caused by stray radiation as compared to analytical flame measurements. The approximate spectra observed in the SSME plume is presented in Figure 8 which shows the relative amplitudes of the 306-nm OH band, the 325-425 nm background, and the 900-1050 nm  $\text{H}_2\text{O}$  bands.

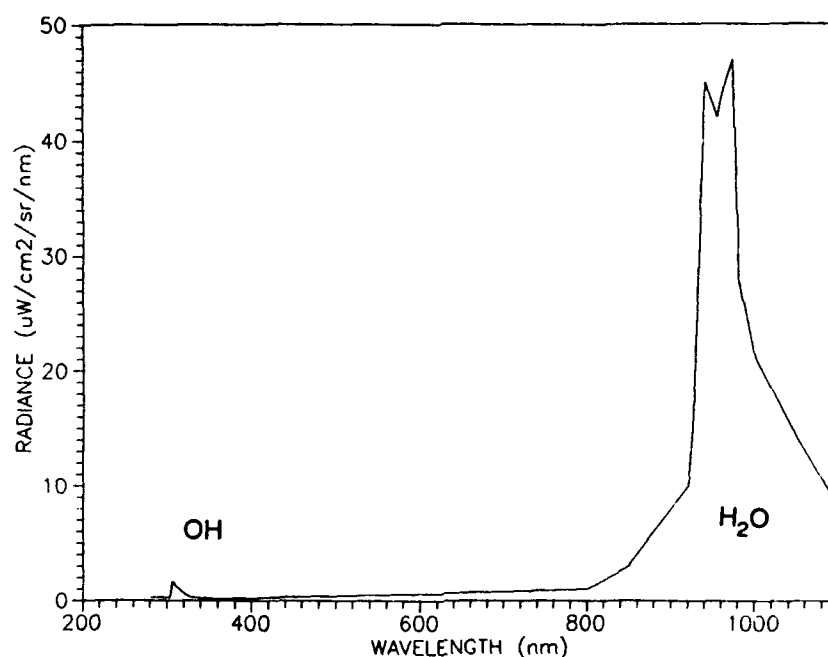


Figure 8. Approximate Spectra from Hydrogen/Oxygen Combustion Products within the SSME.

Stray light sensitivity can be determined by measuring the difference in signal level, first looking at a broad spectral source such as a tungsten filament, and then inserting a high pass color glass filter into the optical path blocking incoming spectra below a cutoff wavelength. Any signal measured below the cutoff wavelength will be the result of stray light.

The signal levels measured during SSME tests were used to calculate the minimum detectability limits for the NASA LeRC Fabry-Perot Interferometer program and in turn to determine the required optic aperture for this design. However, if instrument noise led to overestimation of background spectral radiation, then the minimum detectability levels will be proportionately lower.

Data on high pressure spectroscopy are extremely limited. Liveing and Dewar[7] showed that visible radiation increased very rapidly with pressure, however, their work did not describe behavior in the UV portion of the spectrum. For flames of O<sub>2</sub> burning in H<sub>2</sub>, the blue radiation increased with the square of pressure over the range from 1 to 3 atmospheres. Possible phenomena effecting emission at high pressure were discussed with Dave Chandler and Bob Lucht from the Combustion Research Facility at Sandia National Laboratories. Both expressed skepticism of the H + OH continuum and neither could think of any mechanism that would cause an abnormally high radiation background at 205 atmospheres. However, no real data has been identified so experiments will be required to quantify the background radiation. High resolution spectral mapping within the SSME chamber may be warranted from a scientific standpoint due to the unique opportunity to make oxygen/hydrogen combustion spectroscopy measurements at such an extreme pressure.

Looking at the OH + H continuum described by Padley,



the intensity should be proportional to the OH and H concentration. Figure 7, which was calculated using the STANJAN [8] kinetics code for hydrogen/oxygen equilibrium at various pressures and temperatures, shows OH and H populations which are lower at 205 atmospheres than at one atmosphere (the chamber and plume operating conditions are labelled on Figure 7). Based on this result, and if the continuum does exist, the continuum intensity should be lower relative to metallic specie emissions (at equal metallic specie concentrations) for the 205 atmosphere chamber pressure when compared to atmospheric pressure conditions.

Recirculation during underexpanded operations will entrain nitrogen into the plume boundary. Very low intensity radiation in the yellow-green spectrum from the radiative recombination reaction,



will be produced. However this should not interfere with atomic specie measurements in the UV. Other than the NO + O continuum, no other effects from recirculation should be present.

To summarize available information on background emissions and the effects of high pressure:

- 1) OH population at 205 atmospheres is 10% of the OH population at one atmosphere implying lower thermal excited emissions for the OH bands;
- 2) [OH][H] lower at 205 atmospheres than at one atmosphere implying less continuum radiation;
- 3) Emission and absorption lines significantly pressure broadened at 205 atmospheres implying less self-absorption of OH band emissions;
- 4) No quantitative data available for high pressure emissions from hydrogen/oxygen flames in the UV spectrum.

#### Refraction from Density Gradients

Refractive effects due to density gradients in the expanding nozzle gas were evaluated to decide if refraction was significant. The index of refraction variation was approximated using the axial density profile shown in Figure 4 and scaling the refractive index for air at standard atmospheric conditions for which  $n=1.0003$ . Figure 9 shows the approximate refractive index of the plume gas vs. axial position (the slight variation in refractive index between air and plume gases was not considered).

To evaluate refractive effects, a step change in density and therefore refractive index was assumed, which represents a shock structure. The angular deviation or ray bending caused by this step change in density was calculated as a function of the ray entrance angle from normal to the shock. Figure 10 shows rays entering normal or nearly normal are not effected. As the entrance ray becomes parallel with the shock structure, the ray is reflected.

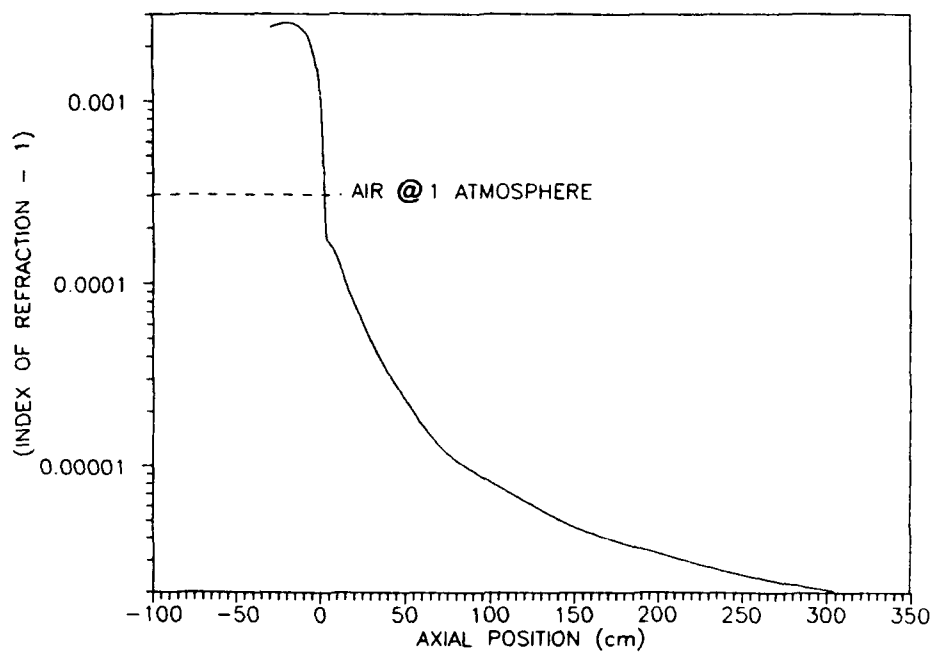


Figure 9. Approximate Refractive Index of the Plume Gas vs. Radial Position within the SSME.

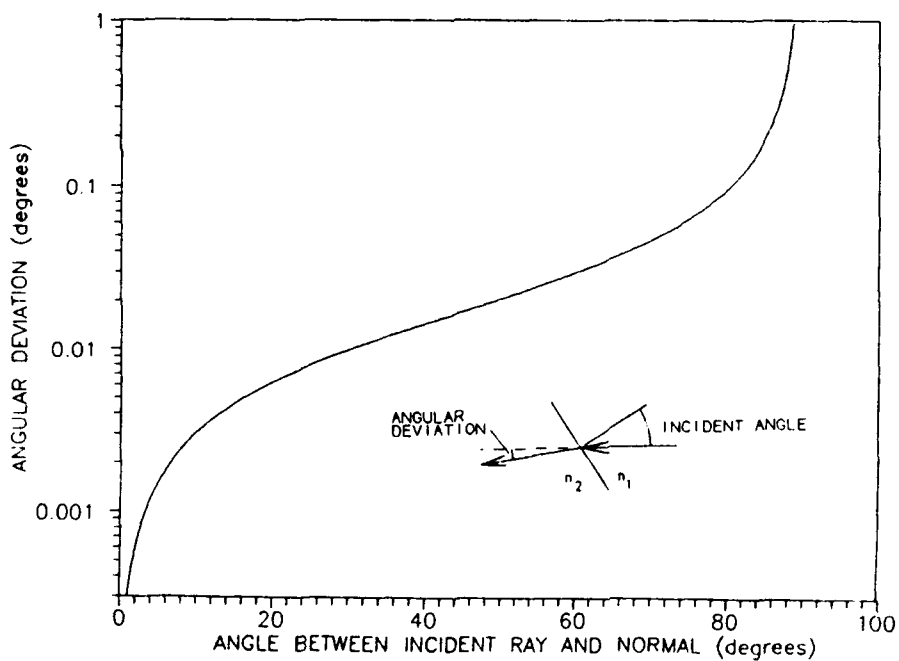


Figure 10. Ray Deflection through SSME Nozzle Barrel Shock as a Function of Incident Angle.

Sea level operation in underexpanded conditions will produce a barrel shock upstream from the optic. If the angle between the barrel shock and the optical path is greater than 80 degrees, no significant refraction will occur. At less than 10 degrees, refraction starts to displace the field-of-view. The angle between the barrel shock and optical path has to be less than about 2 degrees before refraction will degrade performance. It is unlikely such a low angle shock will exist or persist. Refraction should not affect the foreoptic performance.

### Aperture Selection

Most atomic specie emissions available to an optic at the nozzle exit will originate within the combustion chamber. The field of view is set by the throat area. Figure 11 shows the throat produces a field-of-view from the nozzle lip of  $4.1^\circ$ . A fused silica optical fiber has a numerical aperture of approximately 0.28 in the UV, or an acceptance angle of roughly  $30^\circ$ . Therefore, the light collection efficiency of the optic at the nozzle lip can be greatly improved using a lens to match the viewing angle with the fiber acceptance angle. In principal a gain of 7.5 could be achieved; however, this would exactly match the fiber to the throat area leaving no allowance for misalignment. To accommodate misalignment, lenses were evaluated that result in a field-of-view approximately twice the throat diameter.

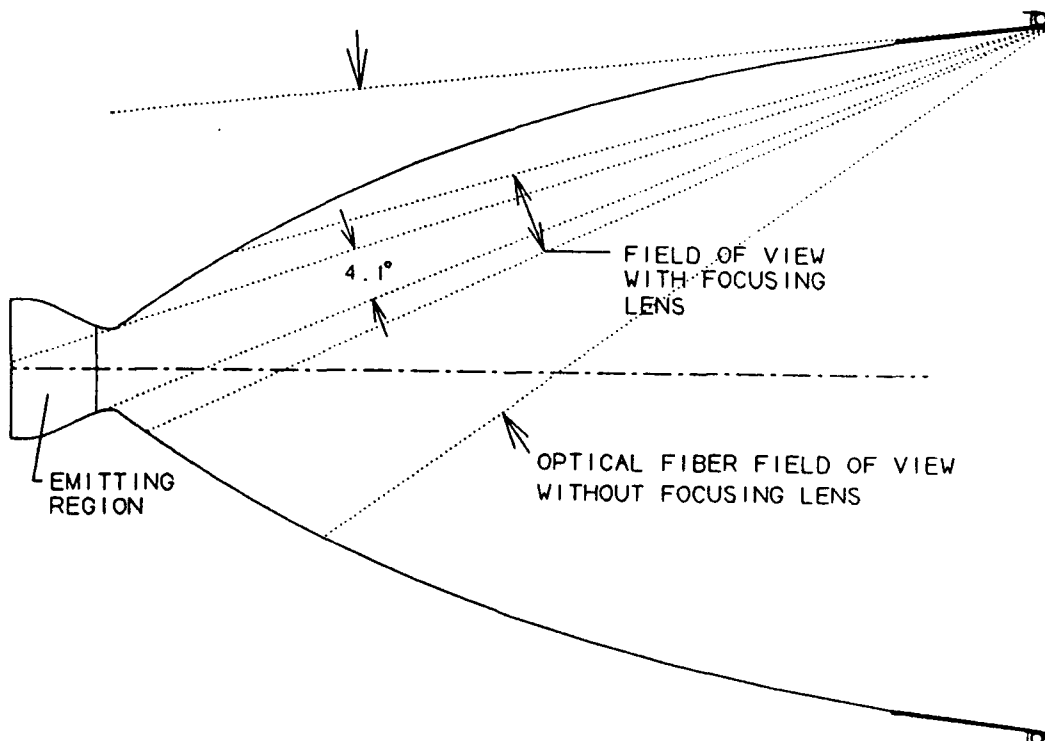


Figure 11. Field-of-View for the Engine Optic Looking at the Throat Plane.

Both the Fabry-Perot (F-P) Interferometric Spectrometer and grating spectrometers have apertures limited by the instrument bandwidths. For a F-P spectrometer with 1/2" optics and a resolution of 0.03-nm, the entrance pinhole diameter is 0.8-mm. A 1/4-m grating spectrometer with a 25 $\mu$ m wide slit and a 1200 line/mm grating has a resolution of 0.4-nm. Since the diode arrays have a height of 2-3 mm, the largest useful entrance aperture is 25 $\mu$ m x 2.5mm or 12% of the F-P aperture. Since the F-P aperture is larger, it was used for sizing the fiberoptic foreoptic aperture.

Three logical aperture choices are available, 1) an 0.8-mm diameter fiber, 2) a 2.5-mm diameter lens focused on a 0.8-mm diameter fiber, and 3) a 5-mm diameter lens focused on a 1.6-mm diameter coherent fiber bundle.

The 2.5-mm lens produces a throat image spot size of 0.4-mm. When focused on a 0.8-mm diameter bundle, this provides a field-of-view twice the diameter of the throat. A ray trace showing a 2.5-mm lens focused on a 0.8-mm bundle is shown in Figure 12.

By using a coherent bundle with a 6-mm diameter lens, a 0.8-mm diameter spot will be focused onto a 1.6-mm diameter fiber bundle. The coherent bundle transfers the 0.8-mm diameter spot through the fiber maintaining the pinhole size. Figure 13 shows how the 0.8-mm diameter spot is displaced on the fiber bundle as misalignment occurs. Unlike a grating spectrometer, interferometers are relatively insensitive to lateral displacement of entrance aperture.

The diode signal-to-noise ratio (S/N), defined as the available optical signal reaching the photodiode detector divided by the noise equivalent power (NEP), was calculated for various metal species as a function of aperture diameter. The results are shown in Figure 14, with the fiber bundle, lens, and lens plus coherent bundle diameters labeled on the figure. To calculate the available optical signal, the flux arriving at an aperture at the nozzle exit for the minimum detectability limit (MDL) was multiplied by the aperture area and transmittance of the optical train. MDL calculations were described in Reference [2]. The value for optical train transmittance was 0.01, described in Reference [9]. A NEP of  $1.4 \times 10^{-11}$  W was used, which is the NEP at 10kHz for a 5.1 mm<sup>2</sup> photodiode.

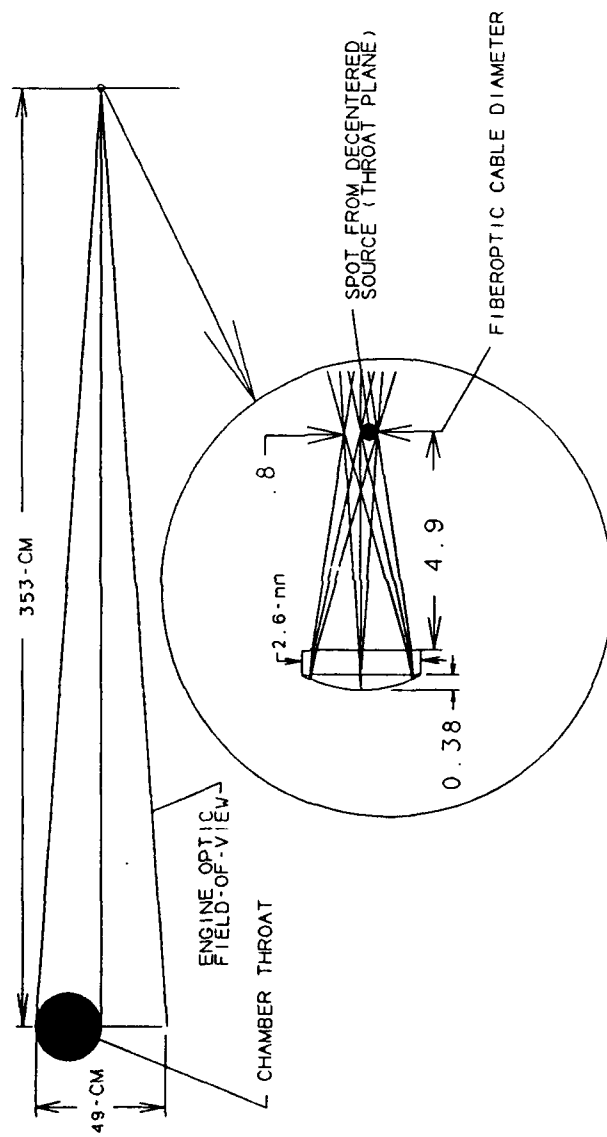


Figure 12. Ray Trace of 2.5-mm Lens with 0.8-mm Diameter Fiberoptic Cable.



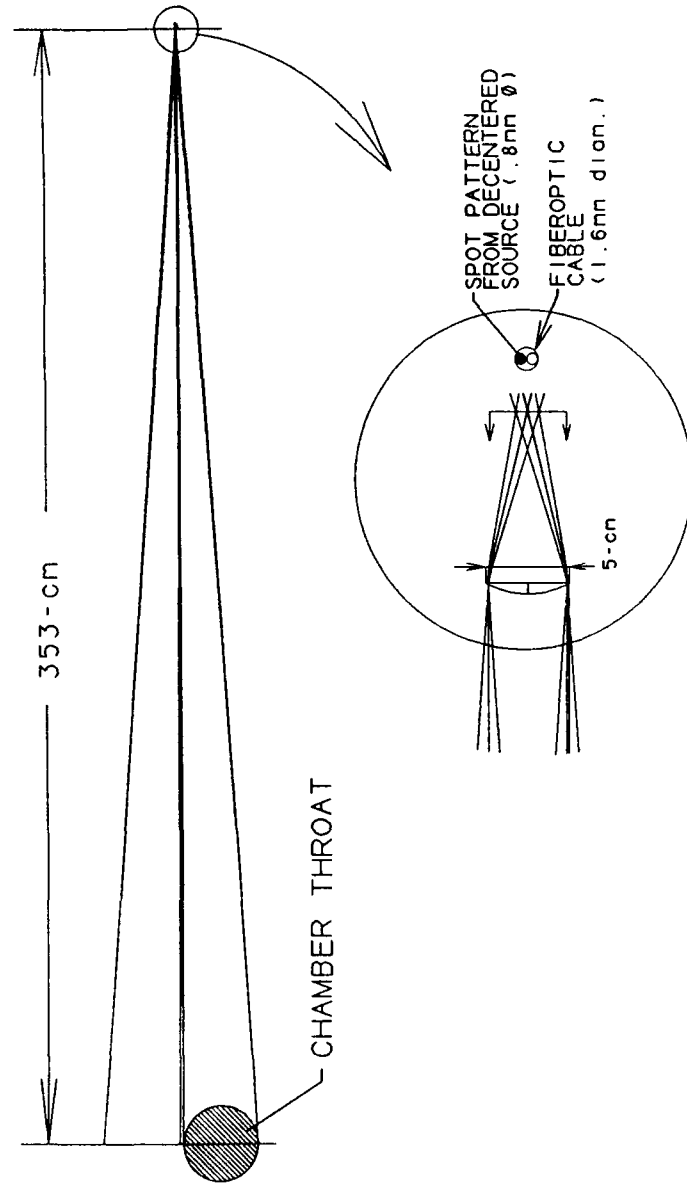


Figure 13. Ray Trace of a 6-mm Diameter Lens Showing a 0.8-mm diameter Spot formed on a 1.6-mm Diameter Fiber Bundle.

The MDL estimates described in Reference [2] were for emission line widths smaller than the instrument resolution. The entire line is accessible to the detector when the F-P interferometer is resonant with the emission line. For emissions from within the chamber, the line widths are roughly 10 times greater than the instrument resolution. Approximately 10% of the signal is accessible when the F-P interferometer transmission matches the emission line center. The Signal-to-Noise ratio (S/N) was calculated for Cu, Cr, Mn, Ca, Ni, and Co assuming the instrumentation resolution was a factor of 10 smaller than the emission line widths.

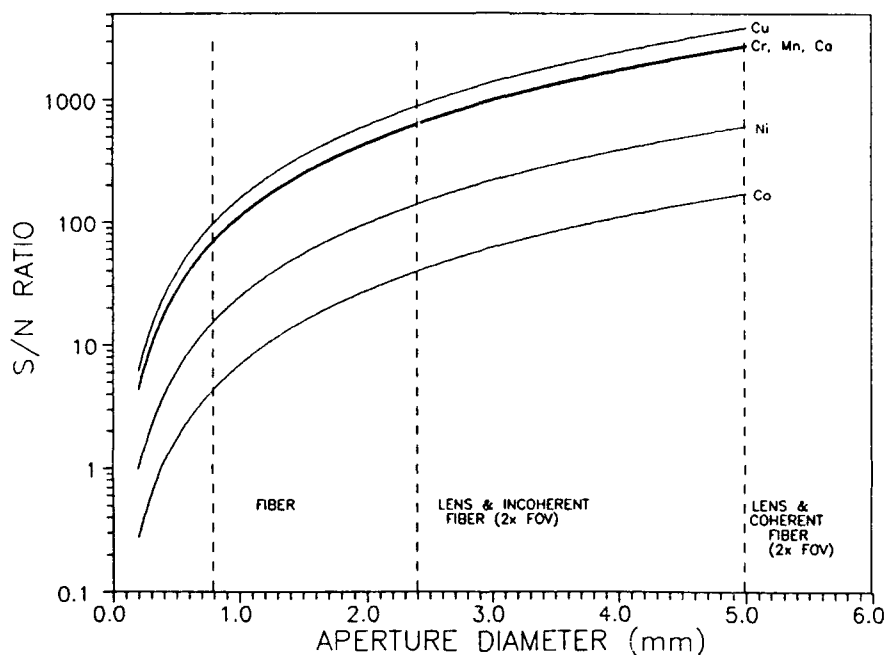


Figure 14. Diode Signal-to-Noise Ratio as a Function of Aperture Diameter.

Using a fiber without a lens, the S/N for Cu, Cr, Mn, and Ca is roughly 100. Ni and Co are substantially less. Therefore, bare fiber would supply adequate signal for emission line detection for strong emitters but would not be adequate for weaker emitters and does not give any margin for uncertainties in equipment performance or design predictions. The 2.5-mm lens increases the S/N for bright species to roughly 700, Ni to 100, and Co to 30. A 2.5-mm aperture supplies adequate signal and margin for uncertainties in specie emission intensities, background radiation levels, and optical system transmittance. Using a 5-mm lens and coherent fiber bundle, the S/N exceeds 100 for all metal species considered.

Use of the MDL calculated based on plume conditions to approximate chamber conditions is almost certainly incorrect; however, lack of data for background emission in the combustion chamber precluded calculating a MDL for the chamber. Instead the fiberoptic system was designed to supply adequate signal for detection if the MDL can be achieved. This prevents the diode S/N from limiting performance.

Based on the results described in the previous discussion, the following recommendations were made regarding aperture selection:

- 1) Develop conceptual designs for the 2.5 and 5 mm apertures;
- 2) Use a nominal 0.8-mm incoherent and a 1.6-mm coherent fiberoptic bundle to provide maximum illumination for a 1/2" optic F-P interferometric spectrometer and a grating spectrometer;
- 3) Maintain a field-of-view roughly twice the throat diameter to provide a balance between alignment tolerance and maximum signal strength.

#### 2.1.2 Subtask 1.2 Environmental Analysis

The thermal and mechanical environments at the SSME exit plane were defined based on engine operating conditions and configurations. Existing data on vibration and acoustic behavior were compiled.

##### Thermal Environment

Existing TDK and SPF (Standard Plume Flowfield) analyses for the SSME were used to define the thermal environment at the nozzle optics. The axial static temperature profile was shown in Figure 3. The pressure and temperature contours calculated by SPF at the sea level 109% power conditions are shown in Figures 15 and 16, respectively. Since the engine is overexpanded at sea level, the barrel shock extends from the nozzle lip to the downstream Mach disc as shown in Figure 15. The nozzle optics will be located outside the boundary of the barrel shock to avoid shock impingement. At high altitude, the engine is underexpanded and the barrel shock will be very weak or non-existent with low or no back pressure (vacuum). Since the optics will be located outside the barrel shock boundary shown in Figure 15, convective heating during sea level operation is the worst-case thermal environment effecting survivability of the nozzle optics.

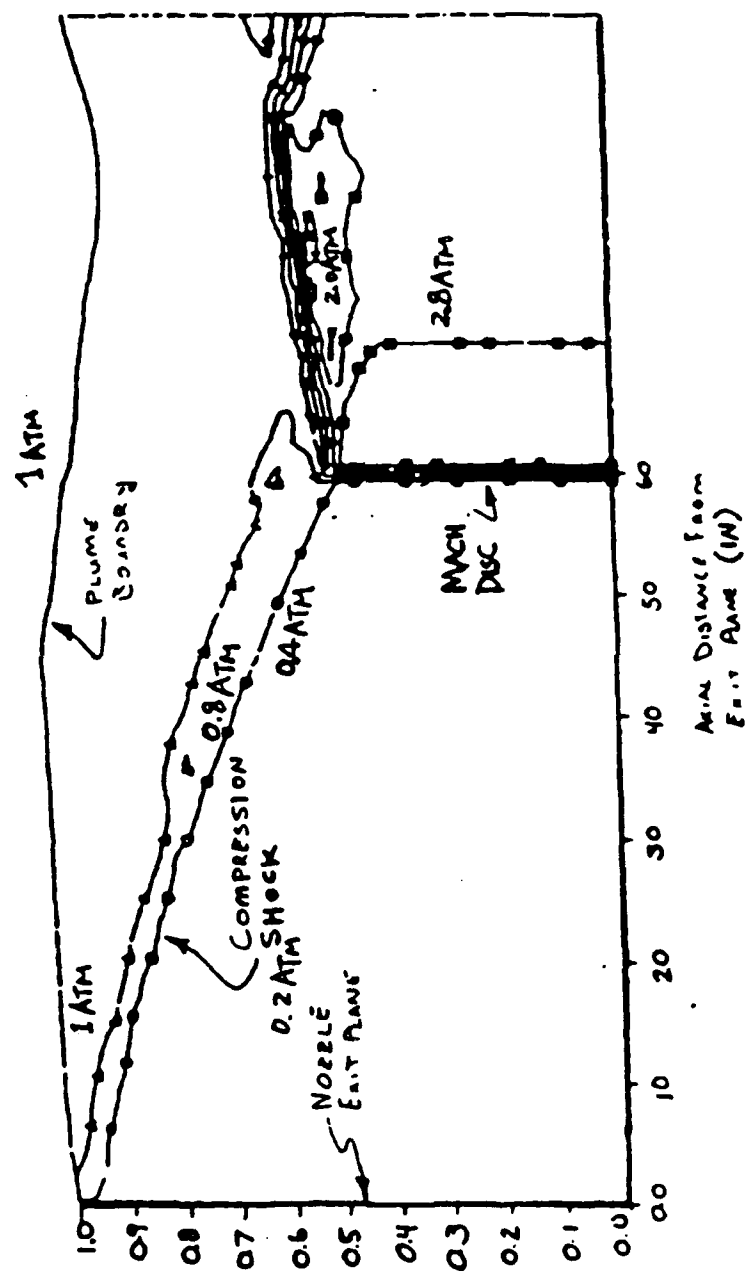


Figure 15. Pressure Field in SSME Plume at Sea Level Conditions.

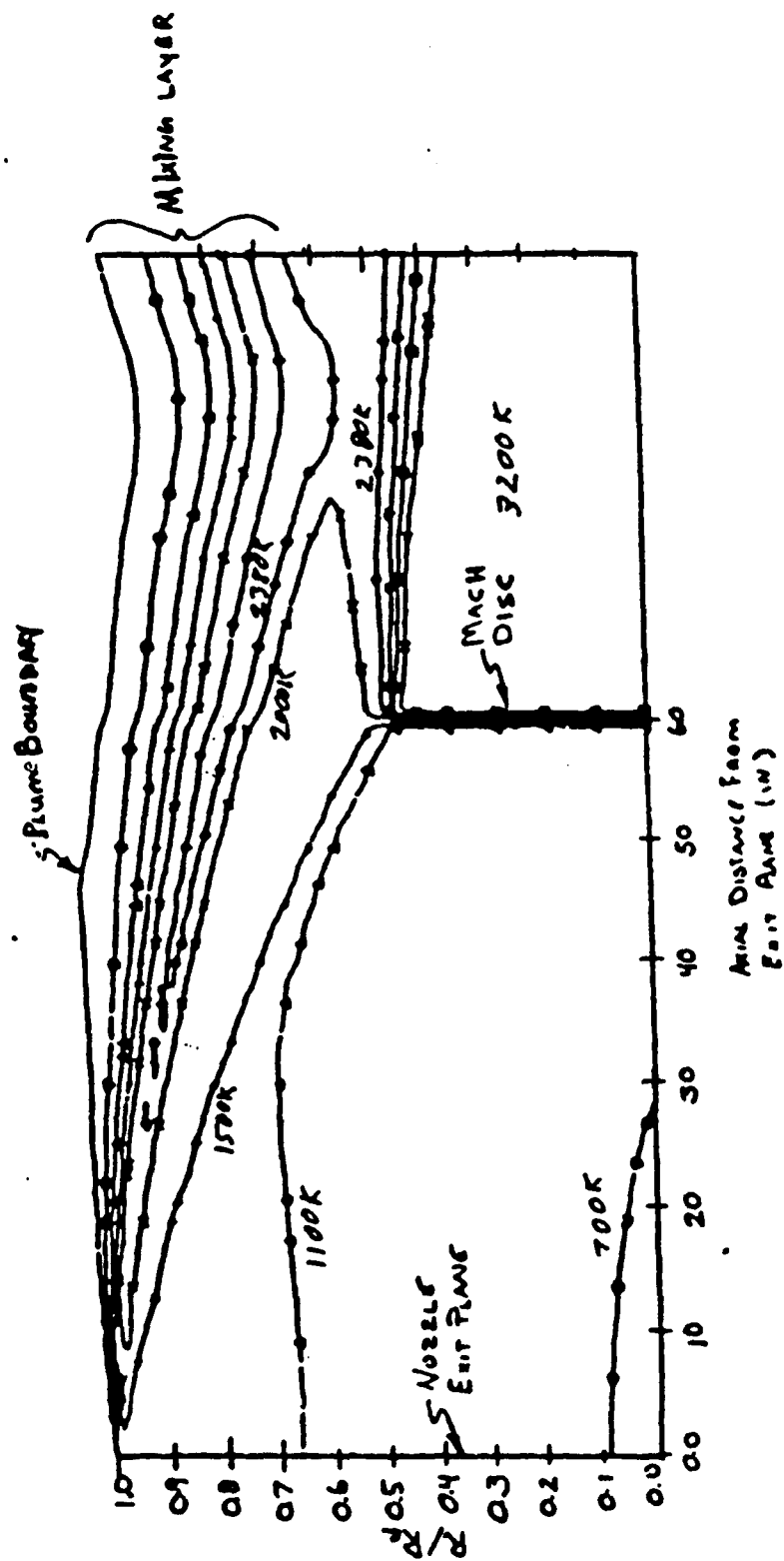


Figure 16. Temperature Field in SSME Plume at Sea Level Conditions.

At the nozzle exit plane, static temperature and pressure near the wall are calculated by TDK at 1430K and 0.4 atmospheres, respectively. However, based on recent tests with TTB Engine 0208 at Marshall Spaceflight Center [10], the measured steady state static temperature at the nozzle exit plane is 670K, which is considerably lower than the predicted TDK result of 1430K. The measured static pressure is on the order of 0.2 atmospheres. For conservatism, the results calculated by TDK, rather than the measurement results, were used in the optics design.

Based on the TDK analyses, the convective heat flux is  $2.7 \text{ MW/m}^2$ . This is approximately 1.6% of the throat heat flux for the SSME. Since the aft manifold is cooled to cryogenic temperatures by liquid hydrogen, conduction cooling from the nozzle optics into the aft manifold will be used to cool the optics. Thermal design parameters will be discussed in detail in Section 2.2.1 of this report.

During engine start and shut-down transients, both pressure and temperature may show over-shoot due to the movement of normal shock wave. The most recent tests on SSME Engine 0208 did produce both pressure and temperature spikes at the exit plane during engine start and shut-down. Since the normal shock wave moves outward from inside to outside the nozzle during engine start, the pressure at the exit plane exhibits a spike as the shock wave passes. The compression shock boundary shown in Figure 15 will be the outermost boundary of the barrel shock at sea level operation. A similar pressure spike should exist during engine shut-down since the normal shock wave will move back into the nozzle.

### Mechanical Environment

Published SSME vibration criteria for the nozzle exit plane were used to determine the mechanical environment for the nozzle optics. For the vibration analysis, the power spectral density (PSD) parallel to the engine centerline was used for design calculations. Figure 17 shows the steady state PSD. Very high amplitude transient accelerations are also experienced by the nozzle assembly as shown in Figure 18.

Figure 19 shows the Space Shuttle combined acoustic environment before liftoff at the SSME nozzle exit plane. The octave band sound pressure level is about 130 to 170 dB.

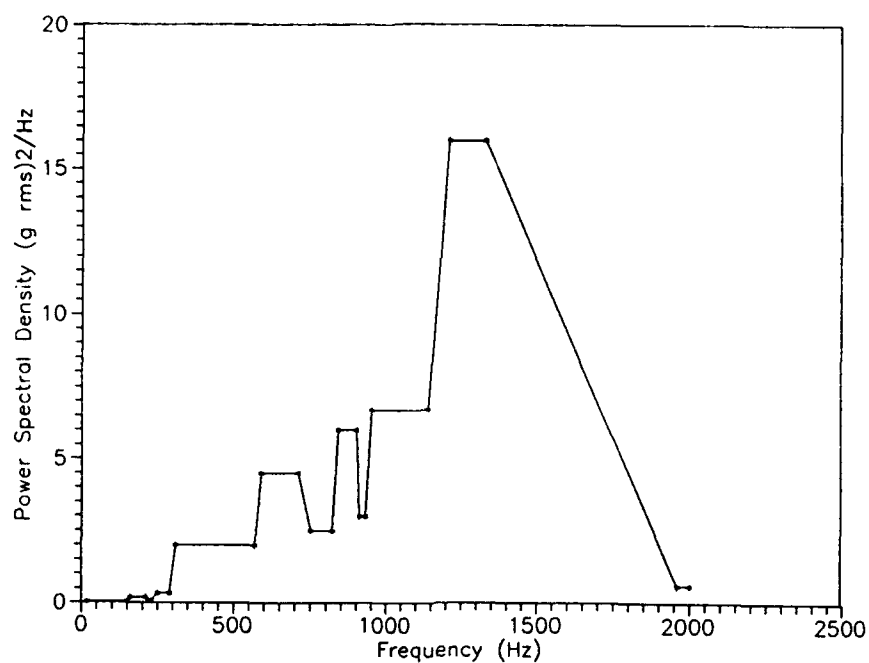


Figure 17. Power Spectral Density for the SSME Nozzle.

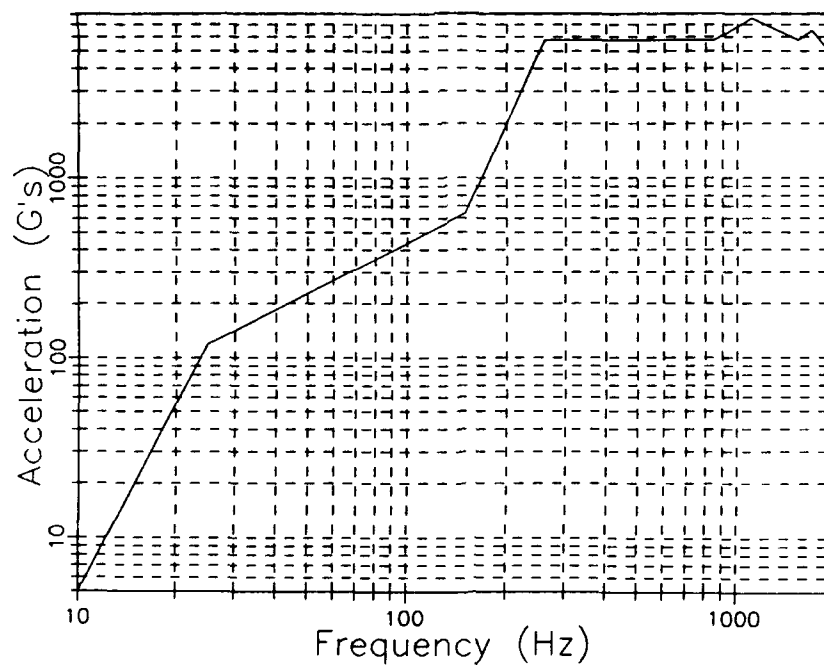


Figure 18. Transient Acceleration Spectra for SSME Nozzle.

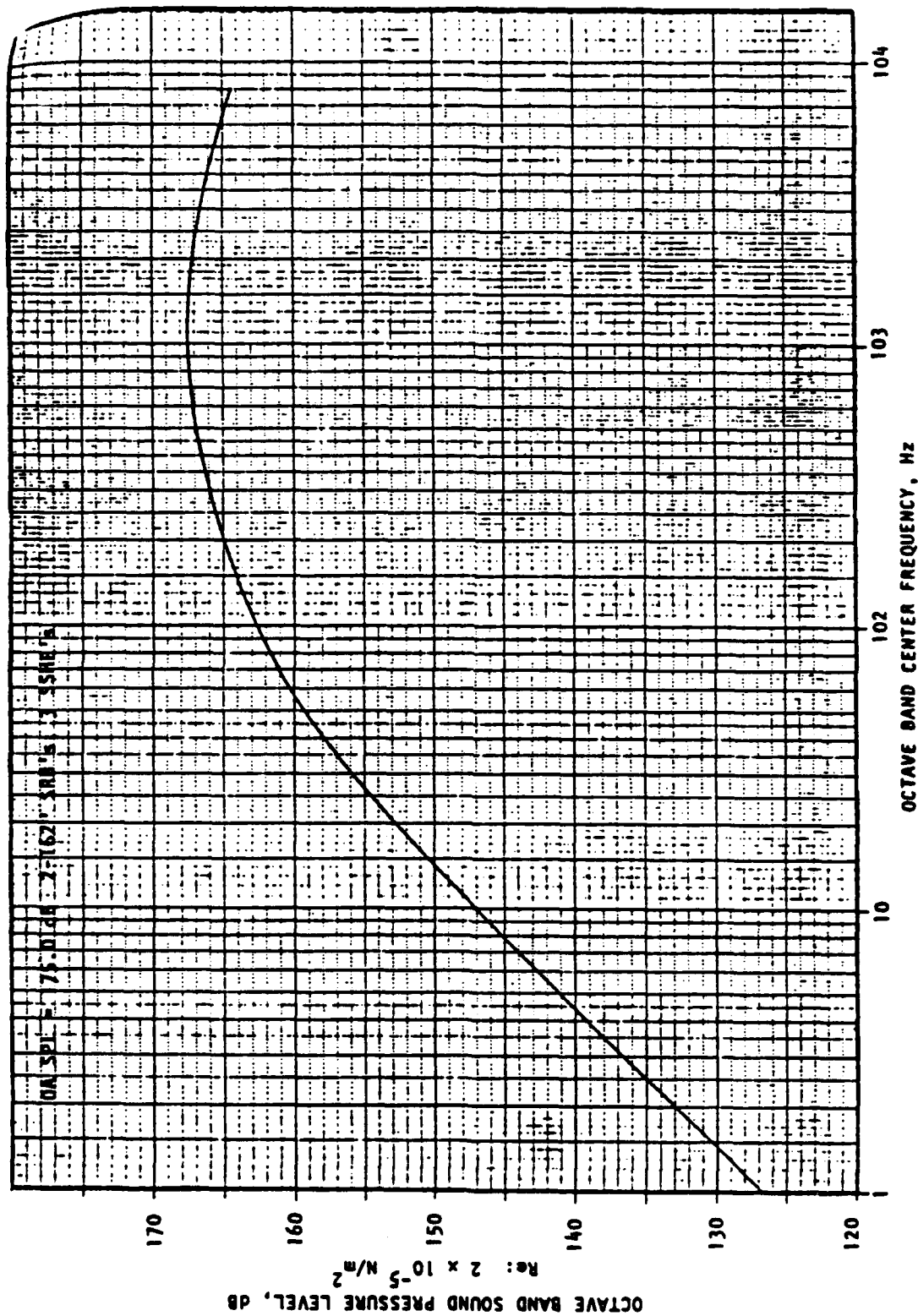


Figure 19. Acoustic Pressure Level Near SSME Nozzle.



### 2.1.3 Subtask 1.3 Interface to Spectrometers

In this subtask, the hardware mounting and optical interface to candidate spectrometers were defined. Features required to interface with various spectrometers are described including the routing and mounting of the fiberoptic cable from the probe to the spectrometer.

A fiberoptic bundle diameter was selected to match the spectrometer with the largest aperture anticipated, which is the Fabry-Perot Interferometric Spectrometer. Using 1/2 inch optics and a resolution of 0.03-nm, the interferometer entrance aperture is 0.8-mm diameter. The entrance aperture for a grating spectrometer depends on the slit width, blazing, and internal pathlength. A typical OMA 1/4 m grating spectrometer, with a 0.4-nm resolution has an entrance aperture equal to 0.3 mm diameter. By sizing the optical cable for the largest available aperture, spectrometers with smaller apertures can be accommodated. Only part of the bundle is used for smaller apertures which decreases the available light.

The engine optic design has a removable fiberoptic connector. This allows fiberoptic cables to be customized for specific spectrometer mounting. Fiber optic cable vendors have slit terminations available for mating to commercial grating spectrometers. The breadboard Fabry-Perot Interferometric Spectrometer has an adjustable mount design that can be readily modified to fit circular bundle terminators from most vendors. By making the fiberoptic cable detachable, the engine optic can be installed on the nozzle and cables selected with terminations matching the spectrometer.

The fiberoptic cable will require multiple anchor points along the nozzle to prevent vibration damage to the cable. The cable can be attached to a drain line or hydrogen duct as shown in Figure 20. Since the fiberoptic cable will have a similar mass to the thermocouple cable bundles on engine 3001, the similar straps may be used.

There are three locations on engine 3001 where drain lines are adjacent to SLAM holes. These locations are sketched on Figure 21 along with the approximate locations of the drain lines and hydrogen ducts. The three sites are numbered in order of preference. Site (1) is furthest from the ignitor, which could potentially damage the fiberoptic cable. Site (3) is adjacent to the ignitor. Figure 22 shows a photograph of a drain line. The preferred engine optic mounting location uses the two SLAM holes between the drain and hydrogen downcomer lines.

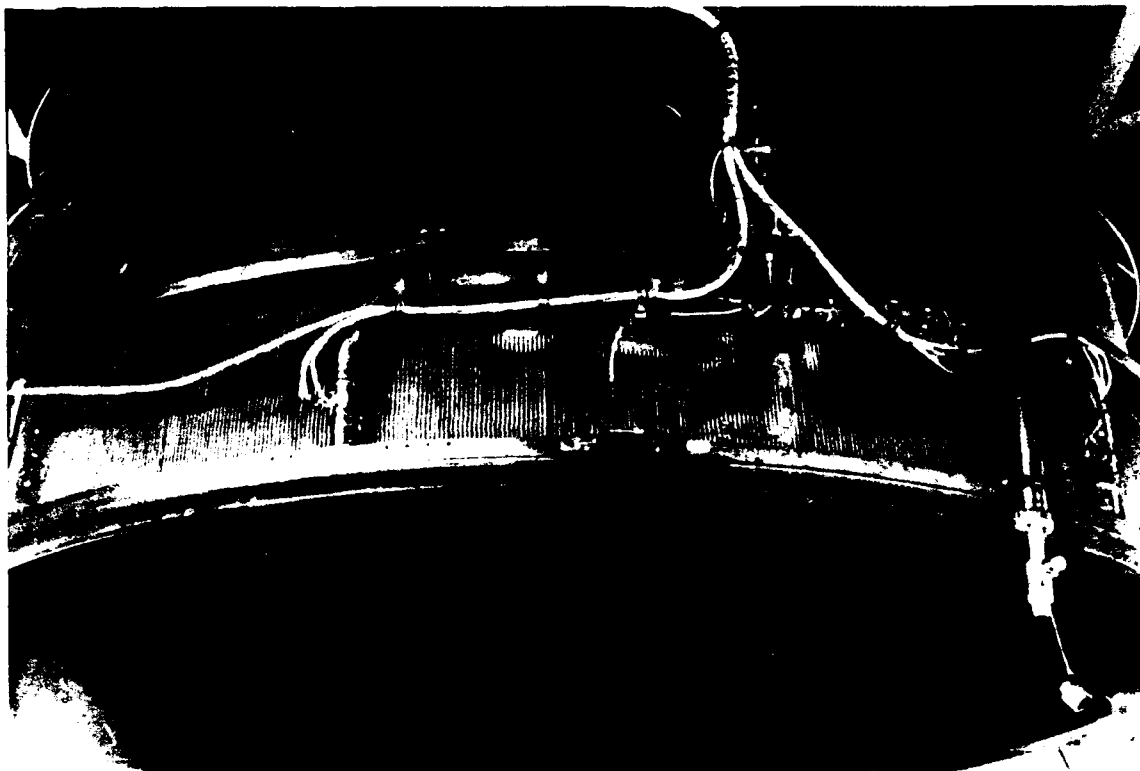


Figure 20. Fiberoptic Cable will be Attached to a Drain Line.



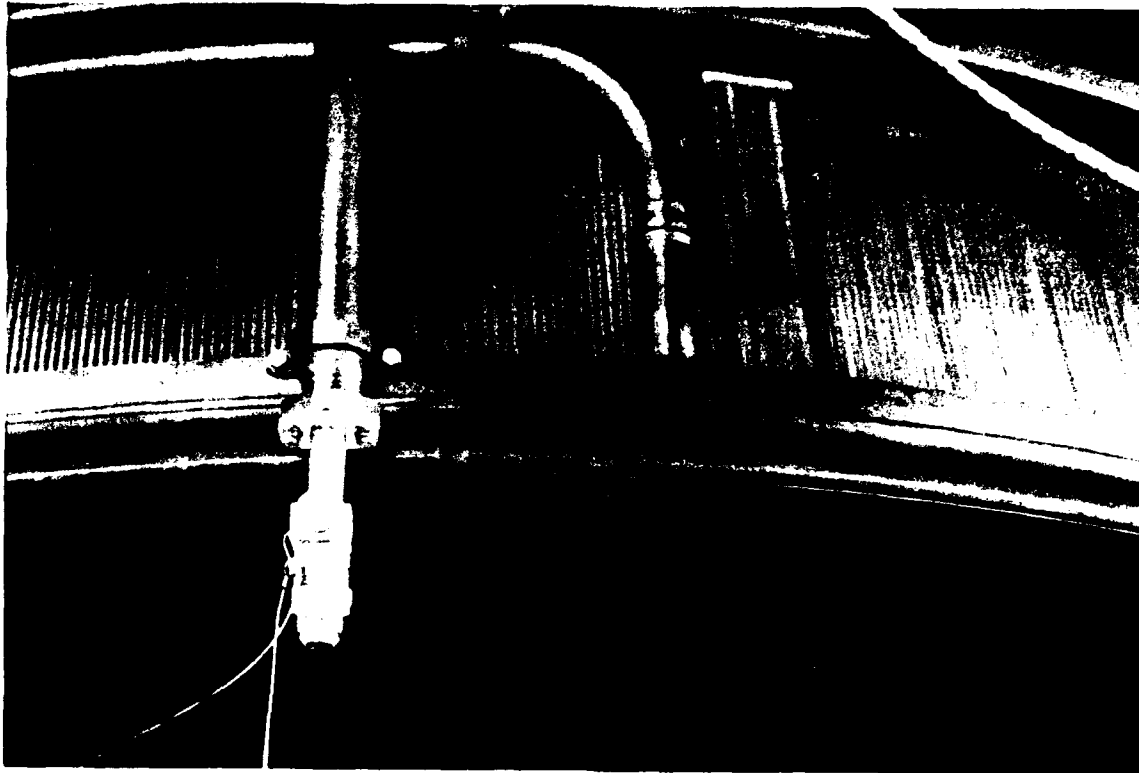


Figure 22. The Engine Optic Mounts to Two SLAM Holes on the Aft Manifold Between the Drain Line and Hydrogen Downcomer, and the Fiberoptic Cable is Anchored to the Drain Line.

#### 2.1.4 Subtask 1.4 Conceptual Designs

Two conceptual designs were prepared that satisfy the optical requirements from Subtask 1.1, the operating environment from Subtask 1.2, and the spectrometer interface definition from Subtask 1.3. The conceptual designs consisted of defining the optical system hardware configuration, cooling method, fiberoptic cable geometry, and mounting system. Preliminary ray trace optical, heat transfer, and mechanical analyses were performed.

Two design concepts were developed that should function in the SSME engine thermal and mechanical environment. The main difference between the two concepts are related to the entrance aperture. The concepts are illustrated in Figures 23 and 24.

Light from the chamber is transferred into a fiberoptic cable using a lens to match the viewing geometry with the fiber acceptance angle. Besides an f-number matching lens, a turning optic is required because the curvature of the aft manifold exceeds the largest acceptable bending radius for optical fibers. The required optical functions of a window, lens, and turning optic are combined into a single element. Although the prism angle would allow total internal reflection, a mirror coating will be specified so that the prism is not sensitive to surface contaminates.

The lens/prism element is mounted so that the outer surface is recessed into a cavity. Convection is reduced by keeping the window away from direct exposure to the plume flow field. The lens/prism is bonded into the optical mount using a high thermal conductivity adhesive, tentatively an RTV silicone silastic loaded with approximately 85% micron-sized silver particles.

A removable fiberoptic cable allows replacement if damaged or when a different spectrometer termination is required. A standard threaded connector attaches the fiberoptic cable to the optic mount. Continuous fibers extend through the cable connector forming a small diameter extension which is fed through the optical mount.

The optical mount is a single component which includes the aft manifold mounting interface, cable mount, and guide, and lens mount. Figure 25 shows either one or two bolts can be used to attach the probe to the aft manifold. A heat transfer enhancing agent at the optic/aft manifold mount interface will be used to increase contact area and decrease contact thermal resistance.

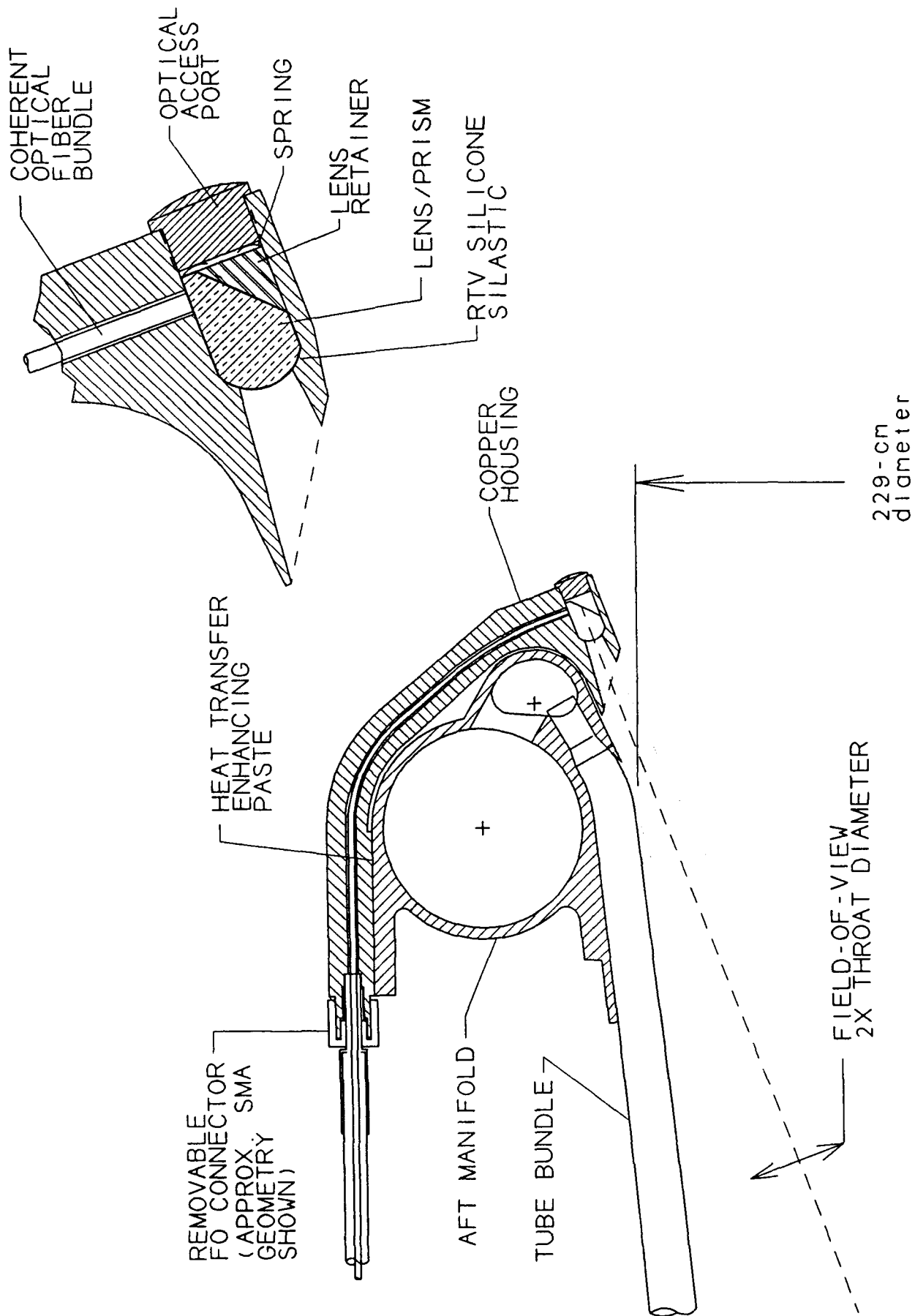


Figure 23. Recommended Subtask 1.4 Conceptual Design.

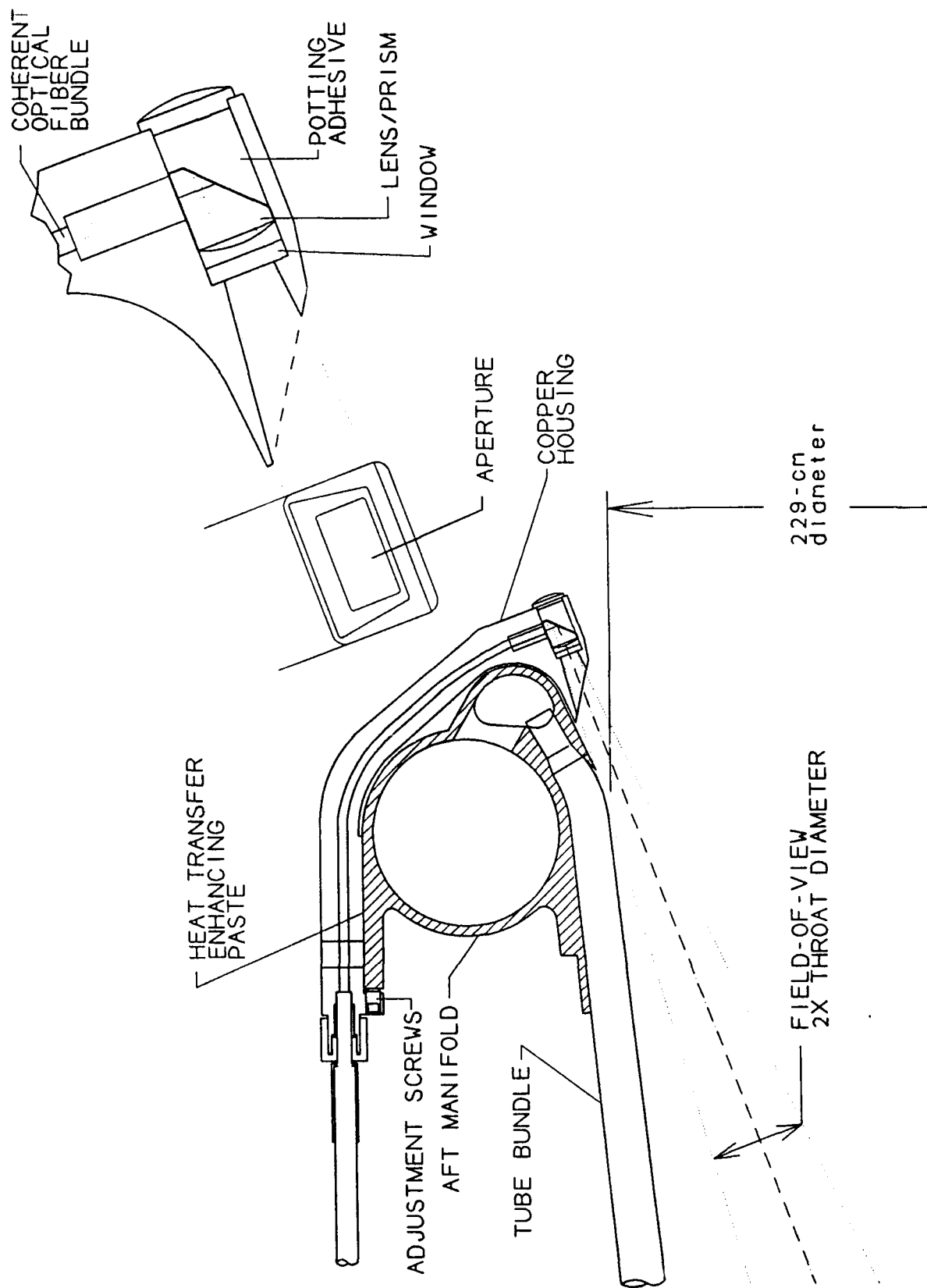
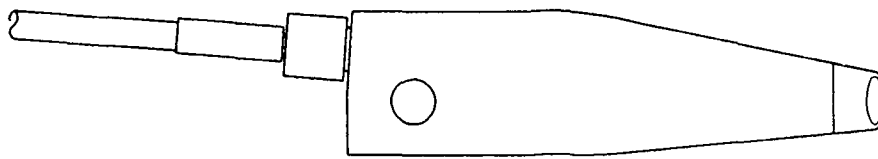
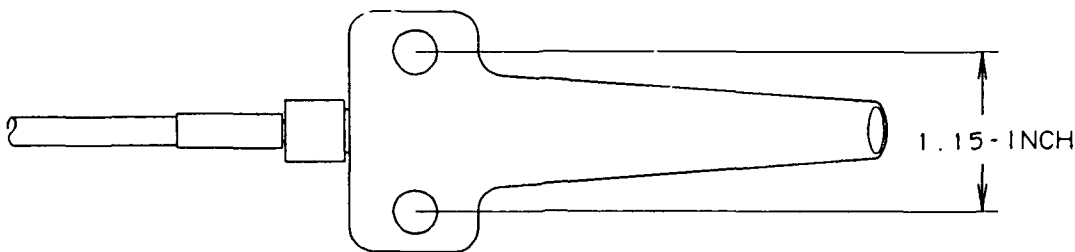


Figure 24. Alternative Subtask 1.4 Design Concepts Illustrated.



a) USES A SINGLE HOLE NEAR A VENT LINE



b) USES SLAM MOUNT HOLES NEAR A VENT LINE

Figure 25. Anchoring Approaches for Attaching Probe to Aft Manifold.

#### 2.1.5 Subtask 1.5 Baseline Design Selection

The two conceptual designs shown in Figures 23 and 24 were evaluated to determine their abilities to meet the optical, spectroscopic, and environmental requirements. A preferred conceptual design, shown in Figure 23, was recommended to the NASA Task Manager. The preferred design will provide superior thermal and mechanical performance. The design shown Figure 24 embodies a combination of alternate approaches to the recommended design. Comparisons of design features and basis for selecting design options are summarized in Table 3.



Figure 3. Comparison of Design Features for Recommended and Alternate Design

Design Feature	Recommended Design	Alternate Design	Justification for Recommendation
Window location	Recessed in mount	Flush in mount	Reduces window heat flux
Window/lens/prism	Integrated optic	Separate components	Reduces reflective losses, simplifies mounting, decreases costs
Lens location	Window surface	Near fiber	Decreases window size, reduces thermal loads
Optic Mounting	High conductivity adhesive	Mechanical bracket	Allows thermal expansion without damaging optic, increases heat transfer from optic to mount, minimizes vibration sensitivity, lower cost
Window sealing	Flexible adhesive	O-ring	More reliable seal in small geometry, adhesive also enhances heat transfer and provides mount for optic
Aperture shape	Circular	Rectangular	Simplifies mount and optic fabrication, provides better mounting features for optic
Aperture size	2.5-mm diameter	2.5 x 5-mm rectangle	Provides adequate signal with minimal exposed surface to flowfield
Fiberoptic cable mounting	Removable	Permanently attached to body	Provides flexibility for switching spectrometer interface, simplifies installation, allows recovery from damage
Fiberoptic cable interface	Extends from connector to optic	Has intermediate fiber bundle from connector to optic	Reduces losses at bundle-to-bundle interface
Field-of-view	Twice the throat diameter	Throat diameter	Provides alignment tolerance, allows for vibrational and thermal/strain deflection
Alignment toward engine axis	Bend mount	Flexure mount	Stiffer, less vibration sensitive, simple field operation
Alignment perpendicular to engine axis	Friction interface with aft manifold	Alignment screws	Less vibration sensitive, lower weight
Interface with aft manifold	Heat transfer enhancing paste	Contact heat transfer	Reduced optic temperature, reduced temperature gradients in aft manifold
Mounting method to aft manifold	Single bolt	Two bolts	Avoids drilling additional hole in aft manifold, depends on hole availability and cable anchoring

## 2.2 Subtask 2: Design and Analysis

Detailed design and analyses were performed based on the conceptual design selected in Subtask 1.5 and the environmental analysis from Subtask 1.2. The effort included detailed design calculations, optical element component selection, and preparation of assembly drawings. For this subtask, the probe engineering design was completed to a point where CDR, fabrication drawing preparation, and test and evaluation can begin.

### 2.2.1 Subtask 2.1 Flowfield and Heat Transfer Analysis

In this subtask, the convective and radiative heat transfer from the SSME plume flow field into the optic probe was analyzed. The analyses included engine start and shut-down transients, and over- and under-expanded cases. Convective heat transfer coefficients were determined for use in the probe thermal analyses.

The TDK analyses predict an average static pressure of 2.9 psi at the SSME nozzle exit plane for 109% power. At sea level operation, the back pressure is approximately 14.7 psi; therefore, the SSME is overexpanded at the sea level and a compression shock will form between the nozzle exit plane and the Mach disc. Figure 26 shows the proposed nozzle optic probe will be located outside of the compression shock boundary to avoid the shock impingement. Also the optical window was recessed to reduce convective heating from the hot gas to the optics.

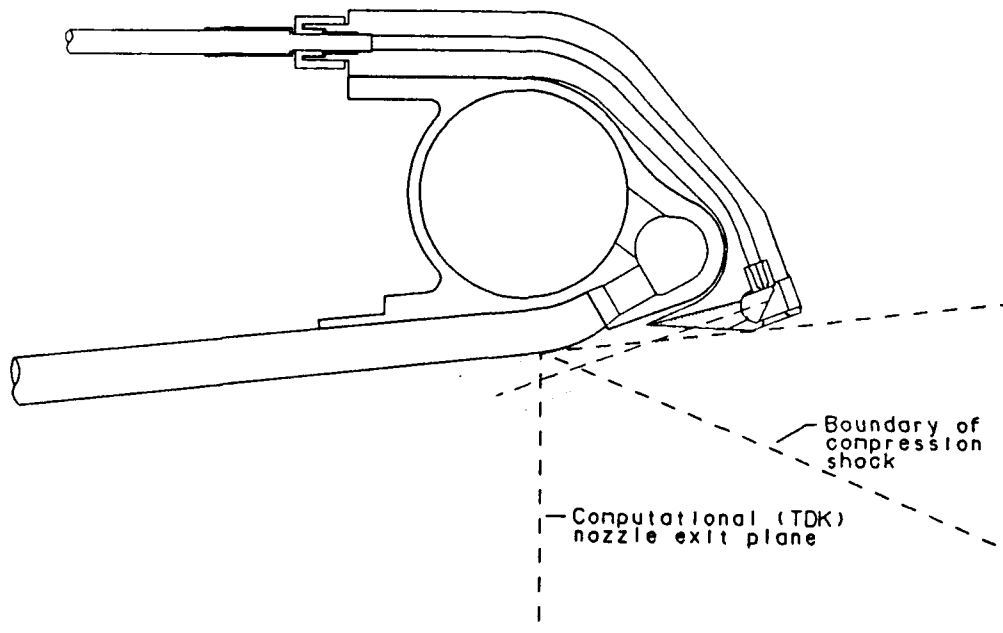


Figure 26. Nozzle Optic is Outside the Compression Shock Boundary.

At the nozzle exit plane, the displacement boundary layer thickness and Reynolds number based on this thickness ( $Re_x$ ) from TDK analyses are 0.26 inches (0.66 cm) and  $1.7 \cdot 10^7$  respectively. The Nusselt number correlation for the high speed flow from Reference [11],

$$Nu_x = 0.322 Pr^{1/3} Re_x^{1/2} \quad (4)$$

was used to calculate the convective heat transfer coefficient from the hot gas to the wall neglecting any impingement effect. The calculated convective heat transfer coefficient for this condition is  $0.000026 \text{ BTU/in}^2 \cdot \text{s} \cdot \text{F}$  ( $76.9 \text{ W/m}^2 \cdot \text{K}$ ). This coefficient does not include impingement or recess effects.

Since the displacement boundary layer thickness of 0.26 inches (0.66 cm) is greater than the protrusion of the proposed nozzle optics design, the approaching flow near the optics should be laminar. For laminar approaching flow, the largest heat transfer enhancement due to flow impingement is twice the unmodified value described above based on measurements reported by Zakkay and Wang[12]. So the largest value of the convective heat transfer coefficient to the optic probe is  $0.000052 \text{ BTU/in}^2 \cdot \text{s} \cdot \text{F}$  ( $154 \text{ W/m}^2 \cdot \text{K}$ ) when the flow impingement effect is included.

The proposed optical window design is recessed to reduce the convective heating. The heat transfer correlation for open cavities in supersonic flow [13] was used to estimate this effect. The correlation for the average heat transfer,  $Q_{avg}/Q_o$  is 0.16 so the average heat transfer rate to the optic window is  $4.16 \cdot 10^{-6} \text{ BTU/in}^2 \cdot \text{s} \cdot \text{F}$  ( $123 \text{ W/m}^2 \cdot \text{K}$ ). At the downstream recompression corner, the heat transfer rate will be almost three times the average heat transfer rate within the open cavity or  $1.1 \cdot 10^{-5} \text{ BTU/in}^2 \cdot \text{s} \cdot \text{F}$  ( $32.5 \text{ W/m}^2 \cdot \text{K}$ ). The calculated heat transfer coefficients, which were used in subsequent finite element analyses of the probe, are summarized in Table 4.

Test results from SSME engine 0208 were reviewed to assess possible effects of start and shut-down transients on the probe. The test data show a pressure spike may exist approximately 2 seconds after the start command and 1 second after the shut-down command. The movement of a normal shock past the pressure probe during the transient may cause the pressure spike[14].

Table 4. Heat Transfer Coefficients Calculated for the Engine Optic Interacting with the SSME Plume Flowfield.

Location	Heat Transfer Coefficient BTU/in <sup>2</sup> ·s·F
Sides of Probe	0.000026
Impingement Surface	0.000052
Cavity Wall	0.0000042
Lens Face and Base of Cavity	0.000011

The computed static temperature at the nozzle exit plane from TDK was 2580° R (1430K) since the static temperature measured for engine 0208 was only 1150° R (640K). The test data show a temperature spike as high as 3000° R (1667K) may occur for 1 to 2 seconds after the start or shut-down command. However, since the Mach number at the nozzle exit plane is approximately 4.65, the high speed recovery effect is the dominant factor in the calculation of recovery gas temperature. The computed recovery gas temperature used for the heat transfer analysis is 5900° R (3278K).

The recovery gas temperature and convective heat transfer coefficients were used to simulate the thermal test results observed with the pressure probe on engine 0208. With a convective heat transfer coefficient of 0.000026 BTU/in<sup>2</sup>·s·F (76.9 W/m<sup>2</sup>·K), the greatest probe surface temperature is less than 1850° F (1283K). Since hot gas flow impinges on the tip of the pressure probe, the flow impingement effect should be included. When the heat transfer coefficient increases to 0.000052 BTU/in<sup>2</sup>·s·F (154 W/m<sup>2</sup>·K), the maximum probe surface temperature exceeds the melting temperature of stainless steel (1533K) despite an optimistic radiation view factor of 1.0. Therefore, the analysis results are consistent with the actual test results and observed failure of the pressure probe on engine 0208.

At high altitude, the nozzle back pressure will be very low. The SSME nozzle will be underexpanded and a Prandtl-Meyer expansion flow rather than a compression shock will occur at the nozzle lip. An illustration of the Prandtl-Meyer expansion flow for the SSME nozzle at this operating condition is shown in Figure 27. The SSME nozzle design curves

gradually outward to have a smooth transition for the expansion flow. To simplify this analysis, a deflection angle of 22 degrees was used.

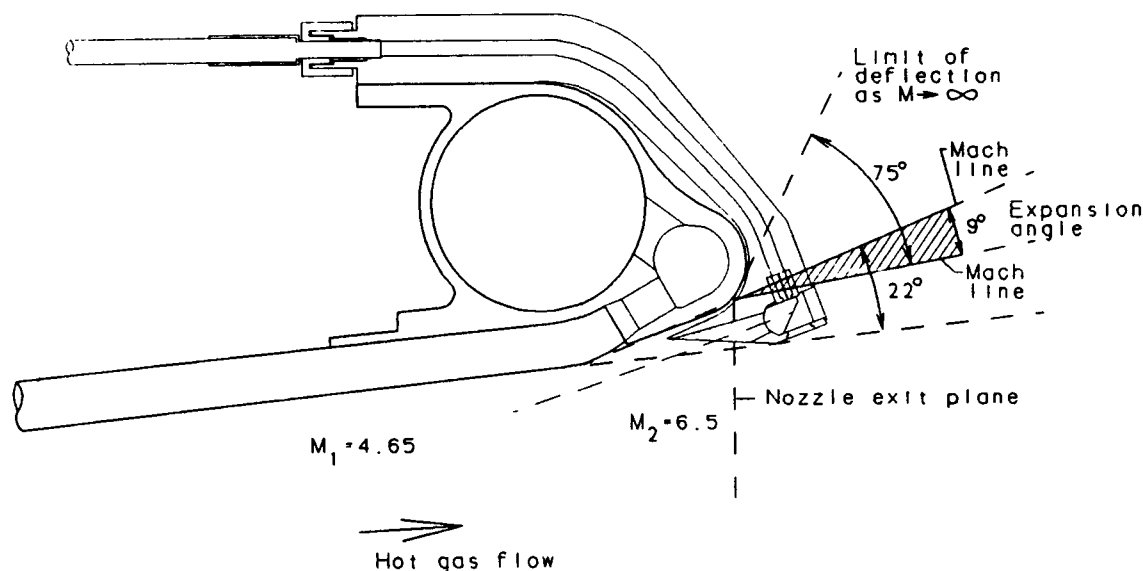


Figure 27. Prandtl-Meyer Expansion Flow of SSME Nozzle at High Altitude.

The analysis suggests the flow will be expanded and accelerated to a Mach number of 6.5 at the nozzle exit plane. Since the back pressure approaches at high altitude, this condition is the limiting case for the expansion flow. The final expansion angle will be approximately 75 degrees. The expansion region is the shaded area shown in Figure 27. Since the expansion is isentropic, the static pressure and static temperature after the expansion will be 0.22 psi (1500 Pa) and 1322°R (734K), respectively. In general, the Stanton number decreases when the Mach number increases so the convective heat transfer coefficient will decrease significantly in high altitude operation. The convective heat transfer coefficient with flow impingement at sea level operation will be the most severe operating condition.

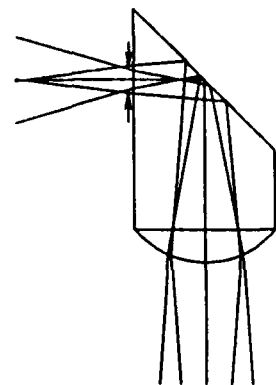
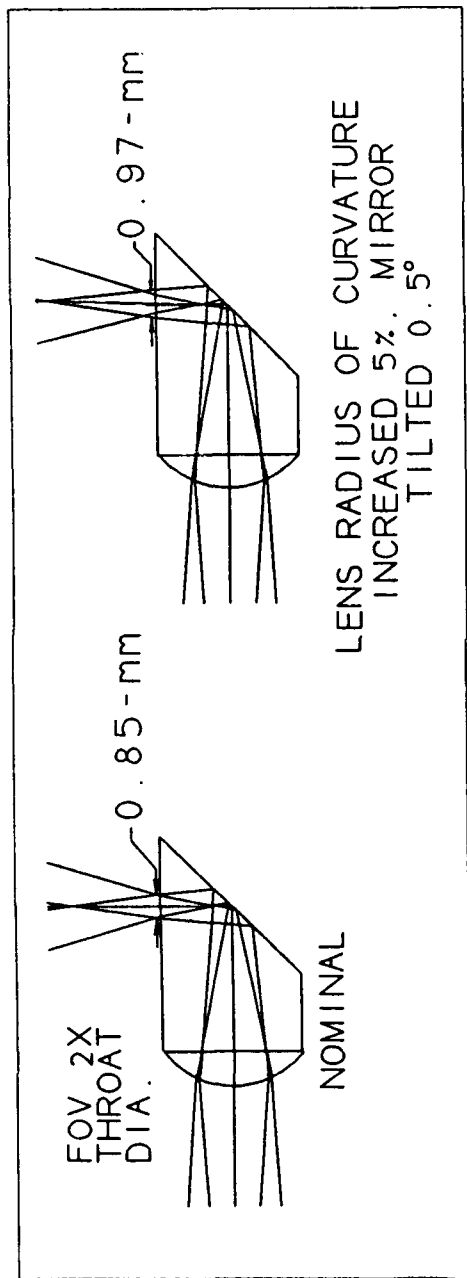
### 2.2.2 Subtask 2.2 Optical Design

Ray trace analyses were performed to find the allowable tolerances for lens dimensions. The series of ray traces presented in Figure 28 show how each lens dimension was perturbed and the effect on beam output diameter and location. Fabricability of optics to the tolerances determined was verified by contacts with optics manufacturers. The tolerances shown on Figure 28 are straight forward for the manufacturers to meet.

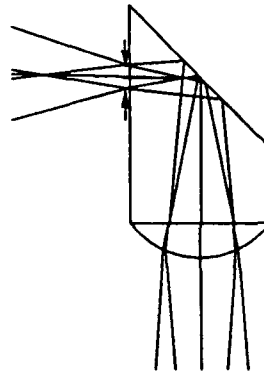
Figure 29 shows that chromatic effects are negligible from refractive index changes. Minor chromatic effects will be observed with the lens/prism mirror coating and the optical cable. The mirror coating reflectivity will be a function of wavelength. Also the fiberoptic cable transmittance will increase at longer wavelengths. Both the mirror reflectance and fiber transmittance affect the signal strength, not the field-of-view. The fiberoptic cable numerical aperture is greater at longer wavelengths although this will not effect the field-of-view since the probe body obscures light outside the 8 degree acceptance angle.

Differential thermal expansion will cause some distortion of the aft manifold and optic probe which will result in misalignment changes. The displacement results from the thermal/stress analysis were used to evaluate thermal expansion. Figure 30 shows the angular rotation at various points on the probe resulting from differential expansion. Most of the rotation is caused by temperature gradients in the aft manifold. This is a worst case analysis since the thermal model used has thermal contact near the bolt holes only which maximizes the temperature gradients in the aft manifold. The angular alignment change is roughly 10% of the allowable tolerance, therefore, the calculated differential expansion is acceptable.

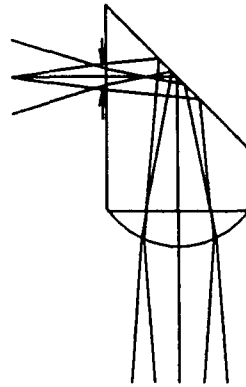
During engine start, the SSME nozzle undergoes significant mechanical distortion. Video tape observations place distortion of the major diameter at approximately 6 inches (15 cm). An analysis of the SSME aft manifold first bell mode distortion was done where the diameter in one direction was distorted 6 inches inward which increased the perpendicular diameter by a similar distance.



LENS RADIUS OF CURVATURE INCREASED 5%



0.5° MIRROR TILT



LENGTH INCREASED BY 0.5-mm

Figure 28. Ray Traces of Lens at Tolerance Limits.

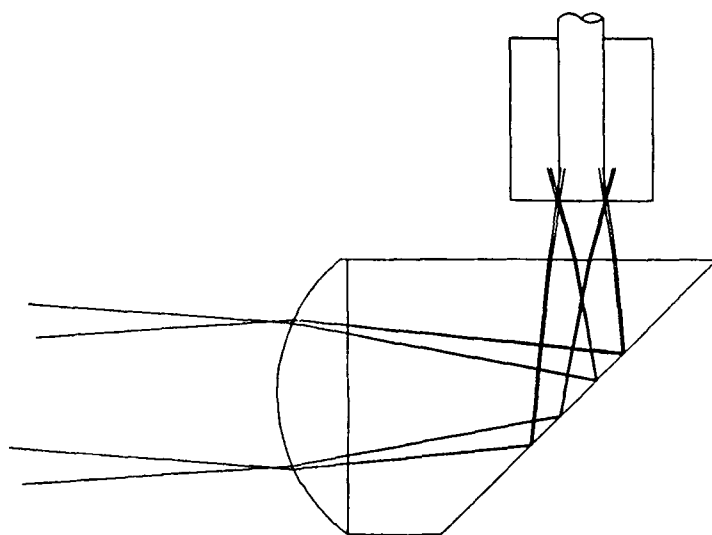


Figure 29. Trace of Marginal Rays for 300 and 700 nm.

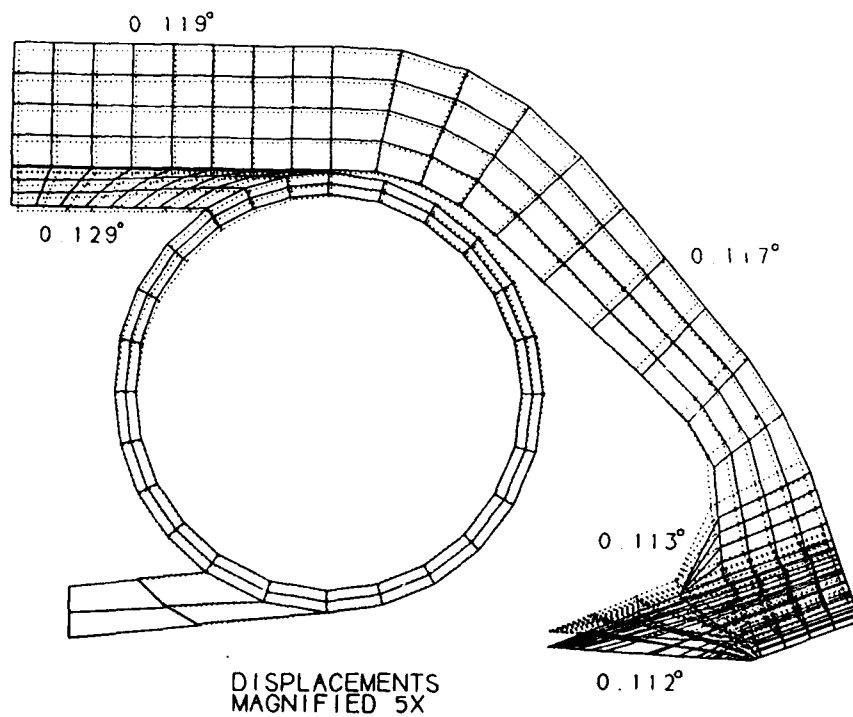


Figure 30. Angular Rotation Caused by Differential Expansion at Various Locations on the Probe.



The worst case alignment change of the engine optic was determined using the 6 inch (15 cm) distorted nozzle shape. Figure 31 shows how the optic field-of-view shifts due to the aft manifold distortion so that only a portion of the throat plane is observed. With this worst case distortion, greater than 50% of the emission signal will remain available. Distortion following the start transient is much smaller so that 100% of the throat plane signal may be observed.

A lesser alignment change will result from the probe rotating inward or outward at the distorted major and minor nozzle diameters during the start transient. The  $0.5^\circ$  rotation is within the allowable  $2^\circ$  rotation tolerance so no loss of field-of-view will occur.

Field-of-view displacement caused by random vibration is minor. Using the probe tip displacement calculated during the finite element (FE) random vibration analysis, the angular rotation of the probe is approximately  $0.02^\circ$  and  $0.28^\circ$  for the aluminum and copper probes respectively.

### 2.2.3 Subtask 2.3 Hardware Configuration

In this section two design alternatives are presented. Figures 32 and 33 show optic probes designed from 6101 T6 aluminum and zirconium-respectively. Both designs should perform the required throat optical monitoring. Tradeoffs exist between the designs. The aluminum design has superior structural features and has a weight which is approximately 1/2 that of the copper probe. The copper design will withstand substantially greater heat loads than the aluminum probe.

#### Probe Baseline Designs

The aluminum probe shown in Figure 32, will operate in the engine thermal/mechanical environment as previously defined. The most critical feature, peak temperature, is predicted to reach 74% of the melt temperature. The thermal analysis should be conservative since high estimates for convective heat transfer coefficients and bulk temperature were used. Without experimental verification, uncertainty remains in the thermal load analysis.

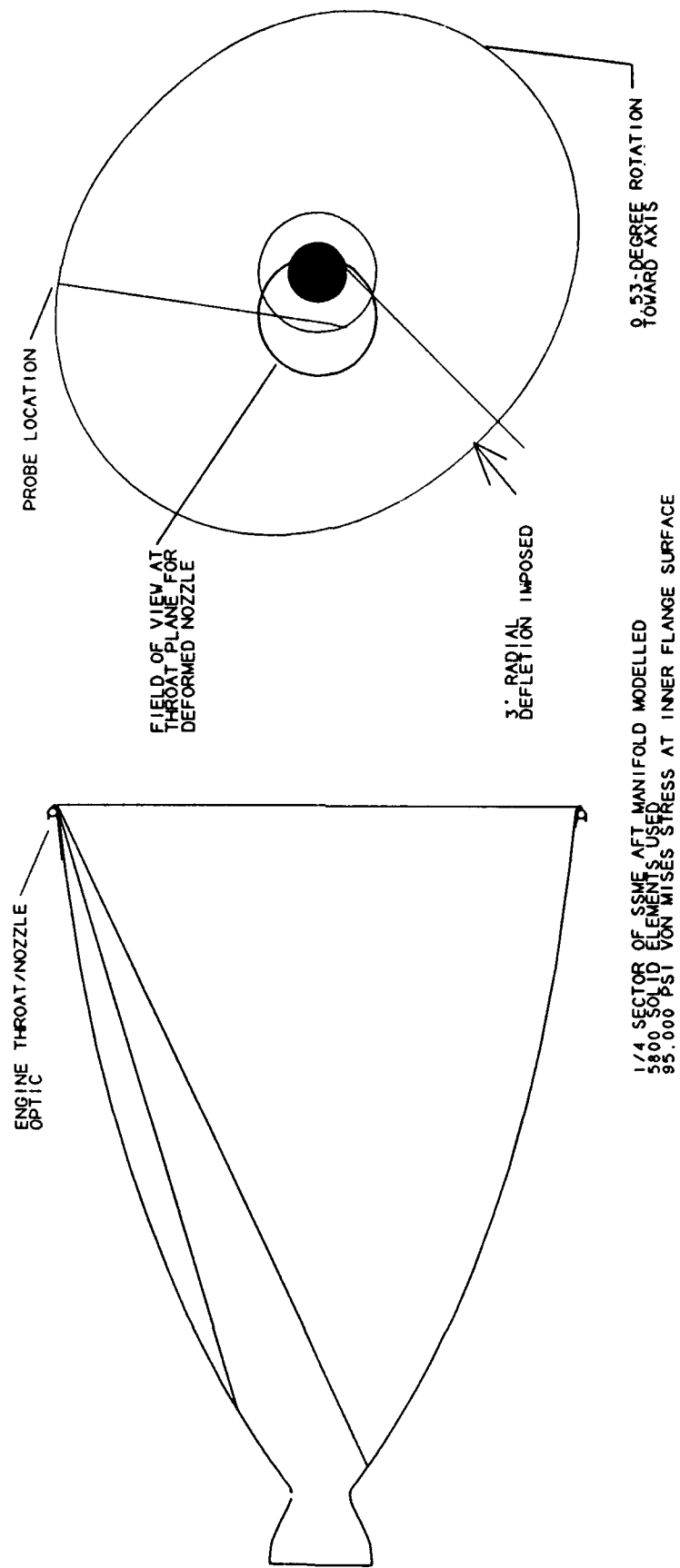
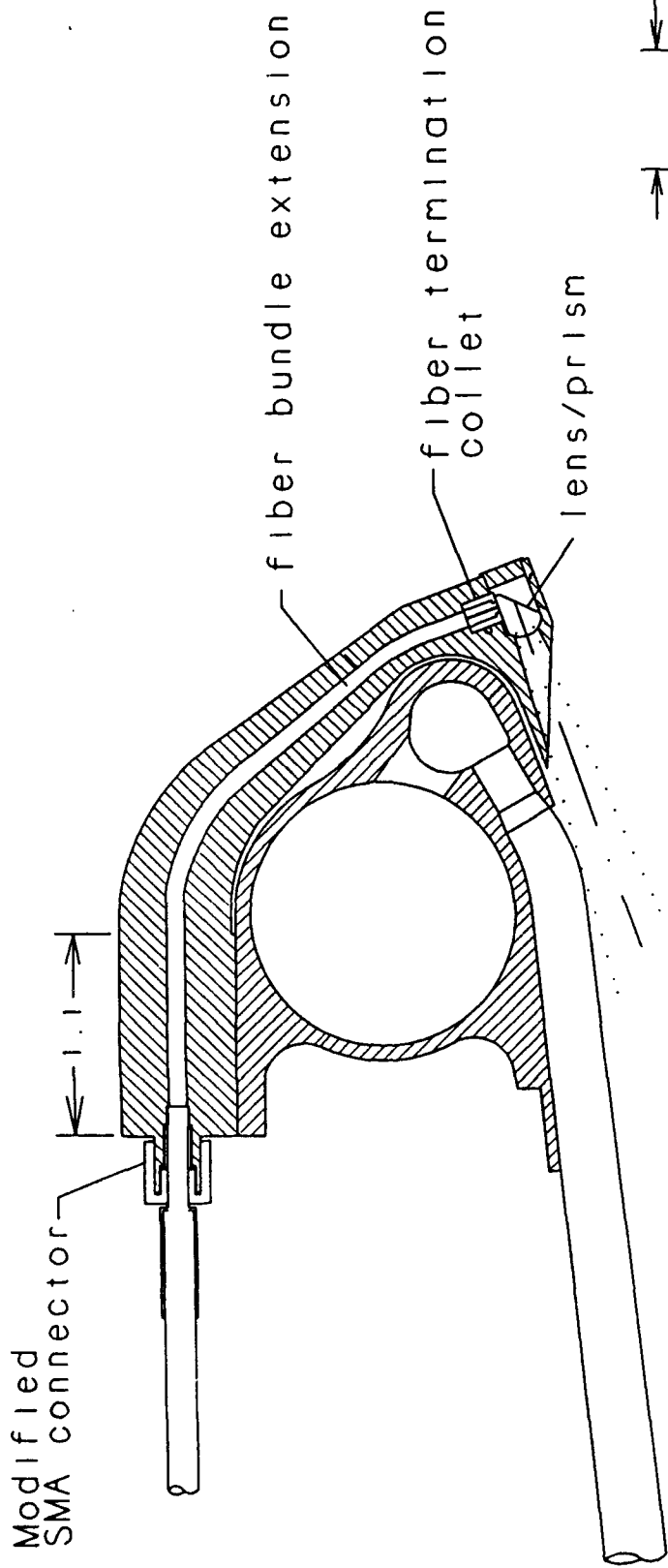
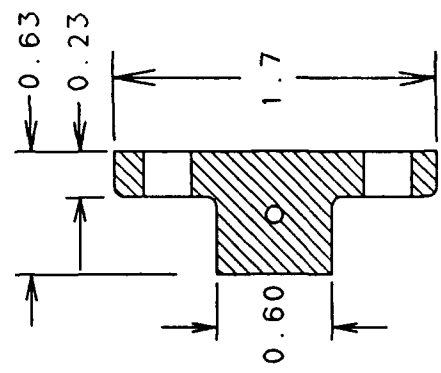
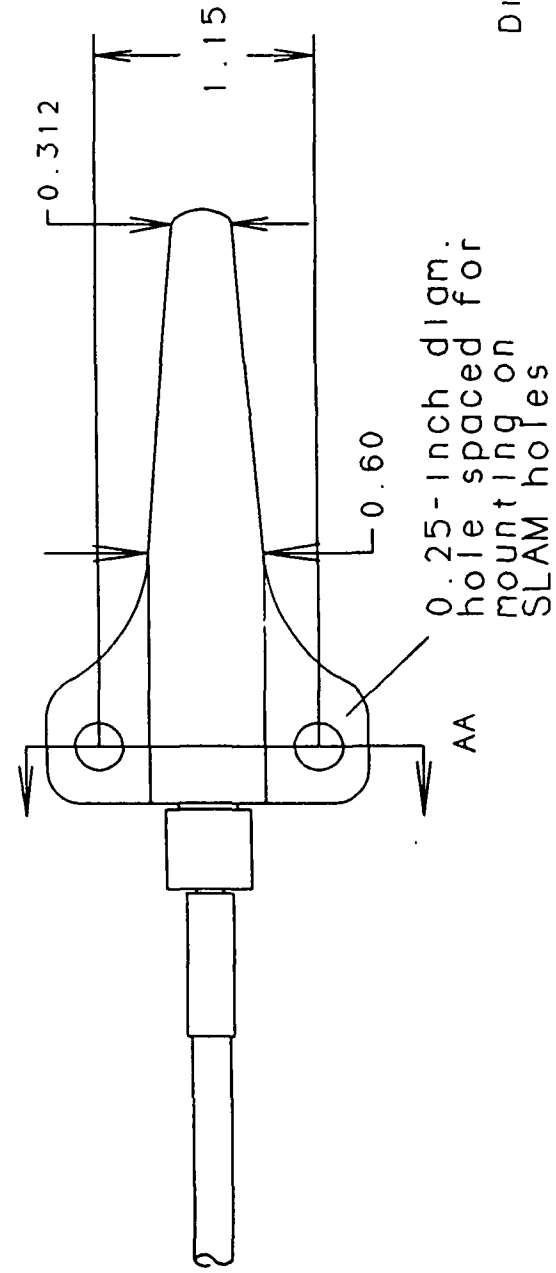


Figure 31. Field-of-View Shift From Aft Manifold Distortion During Start Transient.



45



SECTION  
AA

Dimensions in inches

Figure 32. 6101 T6 Aluminum Engine Optic Design.

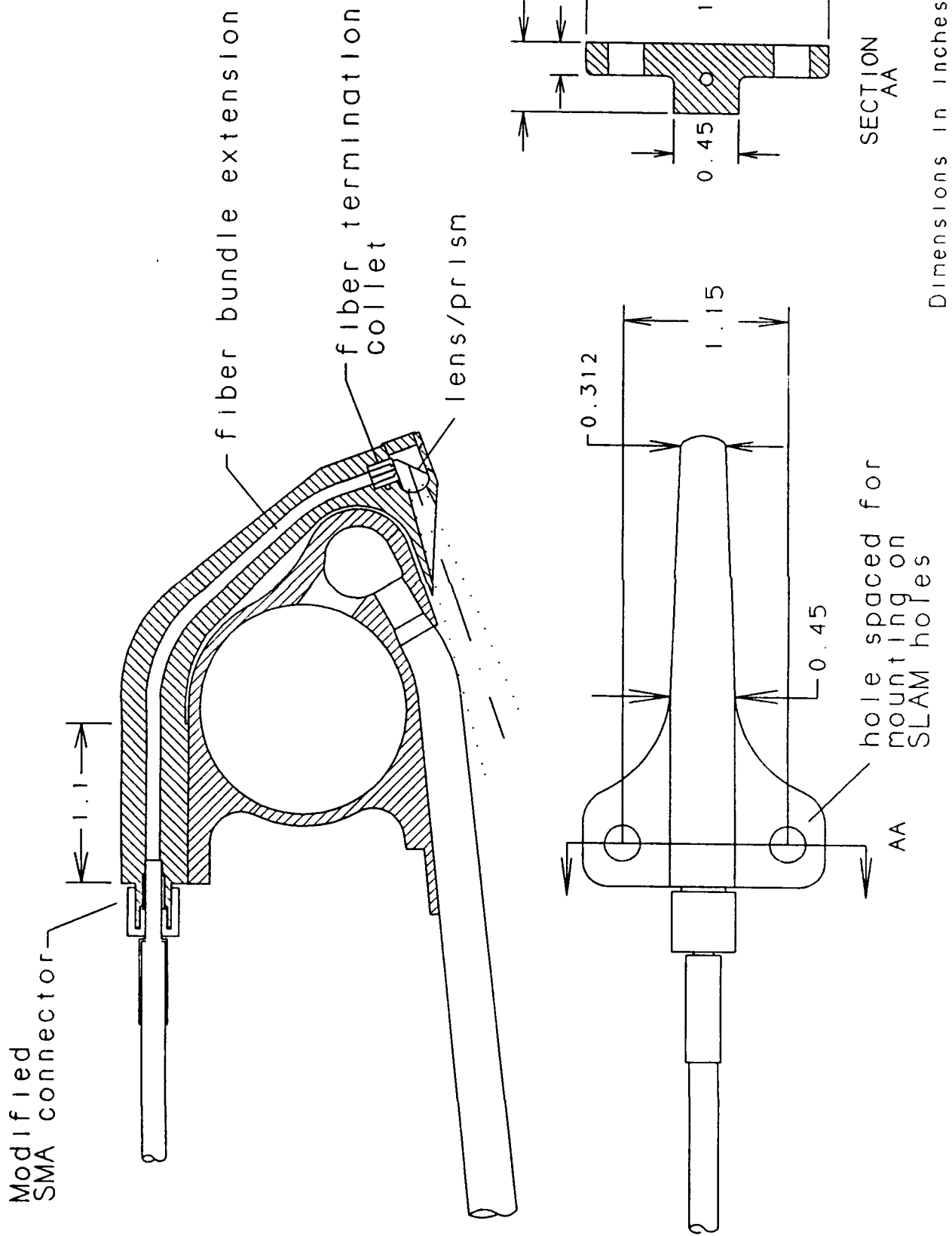


Figure 33. ZrCu Engine Optic Design.

The copper probe design shown in Figure 33 is a compromise between weight and mechanical strength. Using precipitation hardened Zr-Cu with a 40,000 psi (276 MPa) yield strength, the probe will withstand a 5000-g acceleration without significant yielding. The copper probe, with an 0.45 inch (1.1 cm) base width will weigh 0.25 lb (113 gm).

Both designs use a fused silica fiberoptic bundle with a modified SMA connector. The bundle extends through the SMA connector and is encased in a flexible sheathing. A metal band at the fiber bundle termination prevents relative motion between the fibers and provides reference surfaces for accurate termination alignment. Figure 34 shows the fiberoptic cable dimensions and specifications.

The fiber bundle termination is positioned and constrained by a small collet to prevent shifting of the fiber due to vibration and thermal expansion. The collet prevents the fiber termination from contacting the lens so that the hard fused silica fibers will not abrade the lens.

Figure 35 shows the probe objective lens design. Dimensions and tolerances were determined using the ray trace analyses. Since the lower operating wavelength is 300-nm, the lens may be made from optical grade fused silica.

### Materials Selection

A thermally treated aluminum alloy was selected so that the probe body can be strengthened following rough fabrication without additional cold working. Strain hardened alloys would lose strength by annealing during the heating and bending fabrication step which is required to create a curved hole through the probe. Heat treating of the selected 6101 aluminum can be done after initial fabrication and prior to final machining.

The 6000 series aluminum alloys use precipitated magnesium silicide to increase strength. The typical heat treating process requires treating at 515-525 °C to bring the magnesium silicide into solution followed by a rapid quench which precludes significant precipitation during cooldown. Some tempers are cold worked following quenching. The material can then be naturally aged or heated to a precipitation temperature of 170-180 °C for strengthening.

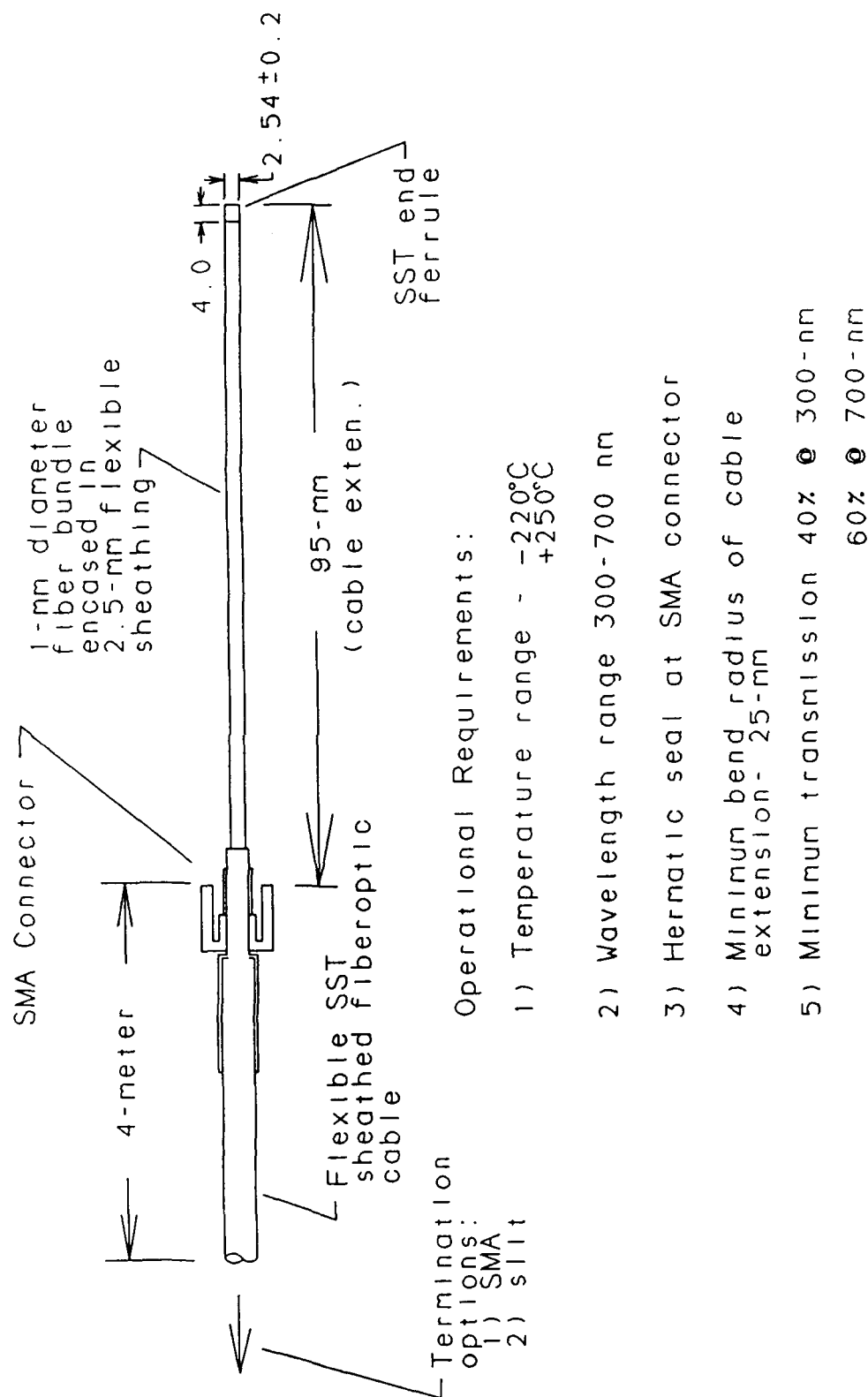


Figure 34. Fiber optic Cable Dimensions and Specifications.

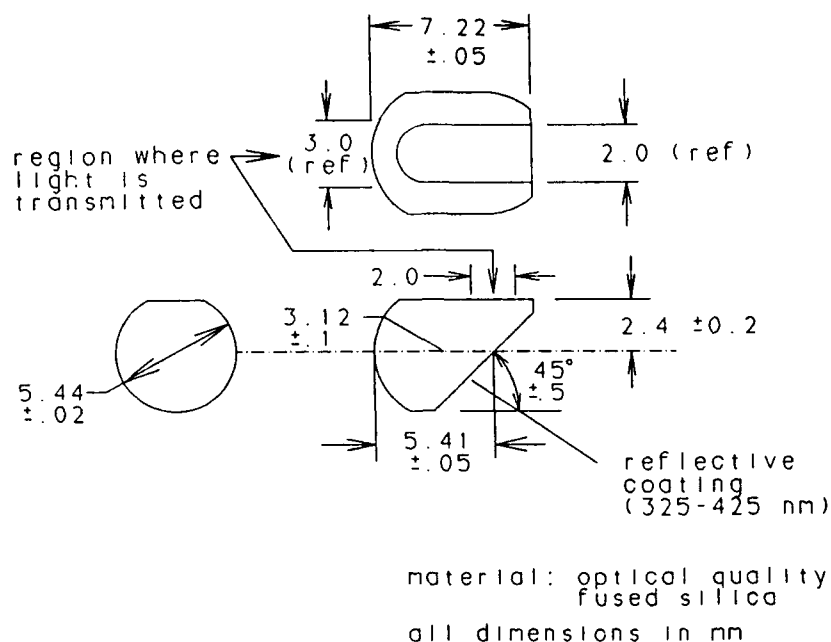


Figure 35. Objective Lens Dimensions and Specifications.

Among the 6000 series aluminum alloys, 6063 and 6101 show the highest thermal conductivity. The T4 temper for 6063 and T6 temper for 6101 do not require any cold working. The 6101 T6 yield strength is 28 ksi (193 MPa) compared to 13 ksi (89 MPa) for 6063 T4 so 6101 was selected for the probe material.

High purity copper has excellent thermal properties but has poor mechanical properties. Various alloys are available with improved mechanical properties. However, copper alloys typically have a thermal conductivity that is significantly lower than high purity copper. Zirconium-coppers are an exception. They have a thermal conductivity which is about 94% that of pure copper and a yield strength which is 4 to 7 times greater. Precipitation hardened zirconium-copper was selected for the copper probe material.

Table 5 shows the important thermal and mechanical properties for each selected material. Since weight is a significant design constraint, two key properties are the

specific thermal conductivity (thermal conductivity divided by density) and specific yield strength (yield strength divided by density). Note that aluminum is superior by both these measures. The principal advantage of copper is a higher melting temperature.

Table 5. Comparison of Zirconium-Copper and 6101 T6 Aluminum Thermal and Mechanical Properties

Property	Units	Zr-Cu	6101 T6 Alum	Alum/ Zr-Cu
Density	gms/cm <sup>3</sup>	8.94	2.68	.3
Thermal Conductivity	W/m·K	367	218	.59
Specific Thermal Cond.	W·m <sup>2</sup> /kg·K	0.041	0.081	1.98
Yield Strength	MPa	262	193	0.74
Specific Yield Strength	MPa·cm <sup>3</sup> /gm	29.3	72	2.46
Expansion Coefficient	1/°C	17.6 10 <sup>-6</sup>	23.4 10 <sup>-6</sup>	1.33
Melting Temperature	°K	1253	889	0.71

A heat transfer enhancing adhesive was selected to bond the lens to the probe body. Without good conduction cooling, the plume convection heat load into the lens could cause excessive heating. The adhesive must withstand the compressive strain resulting from differential expansion between the fused silica lens and metal probe. It must have a high operating temperature. Adhesives meeting these criteria have been developed for high power electronic components.

The adhesive baseline selected is Emerson & Cummings ECCOBOND Solder 59C or equal. ECCOBOND is a silicone based adhesive filled with roughly 85% micron sized silver particulate. It has a service temperature of 960°R (260°C) and a thermal conductivity of 6.6 BTU/ft·hr·°F (11.4 W/m·K).

A heat transfer enhancing material is essential between the aft manifold and probe. Without it, the contact heat transfer resistance is excessive and the probe could fail thermally. Some options are the ECCOBOND 59C type adhesive, a high conductivity grease, or a thermal activated joint compound sold by CrayoTherm. ECCOBOND and the CrayoTherm products will exhibit the lowest outgassing properties in space.



## Probe Manufacturing and Assembly

Manufacturing of the aluminum or copper probe would follow the same process. These are:

- 1) Rough machine the probe body exterior. Drill the fiberoptic cable passage to finish dimension.
- 2) Heat and bend the probe using a mandrel to control shape.
- 3) Heat, quench, and temper to final hardness.
- 4) Finish machine the probe using the ends of the fiberoptic passage for reference.
- 5) Black anodize the aluminum probe or nickel plate the copper probe.

Lens bonding is the most critical assembly step. Often ECCOBOND is applied using a wire mesh as a stencil. For the cylindrical portion of the lens cavity within the probe body, adhesive stenciling can be applied in sections to allow for withdrawal of the stencil without wiping away the adhesive. The lens is installed into the cavity after application of adhesive and allowed to cure.

### 2.2.4 Subtask 2.4 Engine Throat/Nozzle Optic Analysis

The purpose of this task was twofold: 1) to determine the survivability of the probe in the SSME aft manifold thermal and mechanical/acoustic environment, and 2) determine whether the probe may cause damage to the aft manifold. The environmental parameters used in the analyses were described in Section 2.2.1.

The copper and aluminum probe designs were analyzed. The aluminum probe design was developed in response to peak transient accelerations larger than initially expected. Initial design work, based on the 1983 SSME Structural Loads Criteria (SLC) document, shows a peak transient acceleration of 35 g. The peak transient acceleration was increased to 7500 g in latter versions of the SLC document. The 200 fold increase in transient acceleration required a reassessment of the probe design. The original baseline copper design would fail in bending (yield) whereas the aluminum design would withstand a 7500 g load in any direction without yielding. A modified copper probe was considered

which will withstand high transient accelerations of 5000 g without yielding but would fail at 7500 g. Designs for a copper probe to withstand 7500 g led to excessive probe weight and possible risk or damage to the SSME aft manifold.

Based on extensive FE analyses of the probe interaction with the SSME aft manifold combined with engine induced stresses in the aft manifold, it was concluded that neither the copper or aluminum probe designs selected will create a risk to the aft manifold.

### Probe Geometric Scaling

A parametric analysis was performed to optimize the probe cross section. The section of the probe near the bolt flange is the most highly stressed region. This cross section also controls heat dissipation and the probe weight. The geometry in the lens region was kept constant. The bending stress is given by:

$$\sigma = \frac{Mb}{2I} \quad (5)$$

where M is the bending moment exerted by the probe mass subjected to vibrational accelerations, b is the probe width near the bolt mount, and I is the area moment of inertia:

$$I = \frac{1}{12}b^4 \quad (6)$$

The center of gravity for the tapered section is located at 25% of the tapered section length measured from the bolt mount. Using equations (5) and (6):

$$\sigma_{bending} = \frac{6(m_l l + 0.25l m_t) a_v}{b^3} \quad (7)$$

where  $m_l$  is the mass of the probe lens region,  $m_t$  is the tapered section mass, l is the distance between the start of the tapered section and the window region center of gravity, and  $a_v$  is the vibrational acceleration.

Probe peak temperature was calculated using the conduction equation with a geometric shape factor to account for the taper:

$$\frac{q}{k\Delta T} = \left[ \frac{4\pi \left( l + \frac{la}{b} \right)^2}{b^2} \right] \left[ 4\pi \left\{ \frac{l^2 a}{b} + \left( \frac{la}{b} \right)^2 \right\} \right] \quad (8)$$

where (a) is the width at the small end of the tapered section.

Peak temperature, weight, and maximum bending stress are plotted as a function of probe width (b) for aluminum and copper in Figures 36 and 37, respectively. The baseline dimension of 0.6 inch (1.5 cm) for aluminum and 0.45 inch (1.1 cm) for copper are shown.

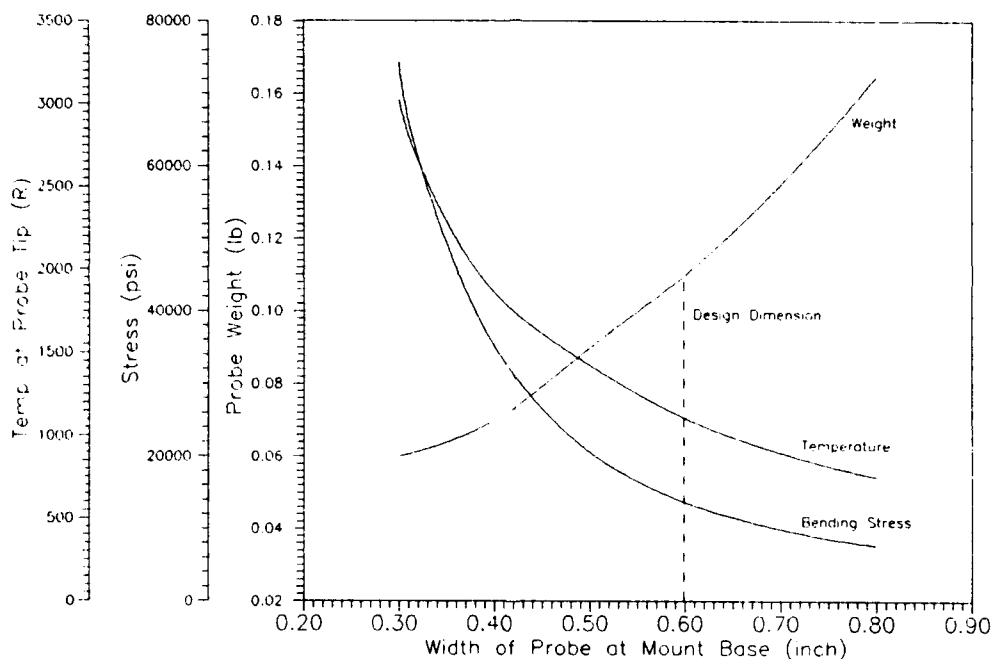


Figure 36. Peak Temperature, Weight, and Maximum Bending Stress as a Function of Cross Section Width for an Aluminum Probe.

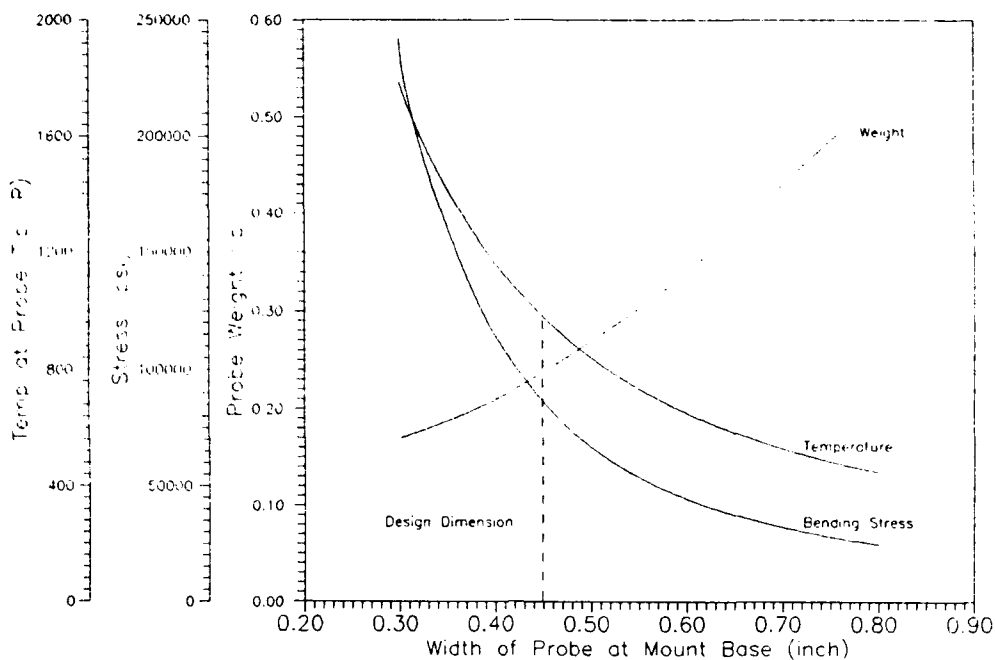


Figure 37. Peak Temperature, Weight, and Maximum Bending Stress as a Function of Cross Section Width for a Copper Probe.

The copper probe design geometry is governed by the mechanical behavior. From Figure 37, the copper probe cross sectional width must be greater than 0.6 inch (1.5 cm) to avoid yielding during the start transient if the aft manifold undergoes a 7500-g acceleration. The peak temperature is roughly 370K which is well below the melt temperature. The copper probe design geometry is governed by the mechanical behavior. At 0.6 inch (1.5 cm) the copper probe weighs about 0.38 lbs (172 gms).

From Figure 37 the bending stress initially drops sharply and then begins to level off. This is because the bending stress varies inversely with the third power of the probe width. Weight, which increases roughly with the second power of width, has an increasing slope beyond 0.45 inch (1.1 cm). Based on this parametric analysis, 0.45 inch (1.1 cm) provides a good balance between strength and weight for a Zr-Cu probe design.

In contrast to the copper probe, the aluminum probe base dimension is constrained both by the allowable peak temperature and the bending stress. A base dimension of 0.6 inch was selected as to provide a good balance between acceptable operating temperature, elastic stresses, and probe weight. The aluminum probe will weigh roughly 0.13 lb (59

gms). The 0.6 inch (1.5 cm) base dimension was used in the aluminum probe design and subsequent analysis.

### Probe Thermal Analyses at Steady State

The combined probe and aft manifold system were analyzed using finite element methods to determine local temperatures. The aft manifold inner surface was assumed to be at the 20K boiling temperature of liquid hydrogen. Low thermal resistance values were assumed at the interface between the probe and aft manifold. Operationally, this will require a heat transfer enhancing agent such as the Emerson & Cuming ECCOBOND 59C silver loaded silastic.

Convective heat transfer boundary conditions were applied to probe simulating the engine flowfield heat load as shown in Figure 38. Using the values shown in Table 4, a total heat load of approximately 160 W was applied. Convection boundary conditions were applied uniformly to the probe impingement face and to faces parallel to the gas flow (rather than using decreased values near the aft manifold surfaces). The impingement surface is nearly parallel to the flowfield so the  $>2$  increase in the heat transfer coefficient used to account for impingement is probably conservative. To account for uncertainties for convection within the lens cavity, the lens impingement coefficient was used for exposed lens surfaces and the conical recess in the probe body. the effects of these assumptions should be a conservative thermal design.

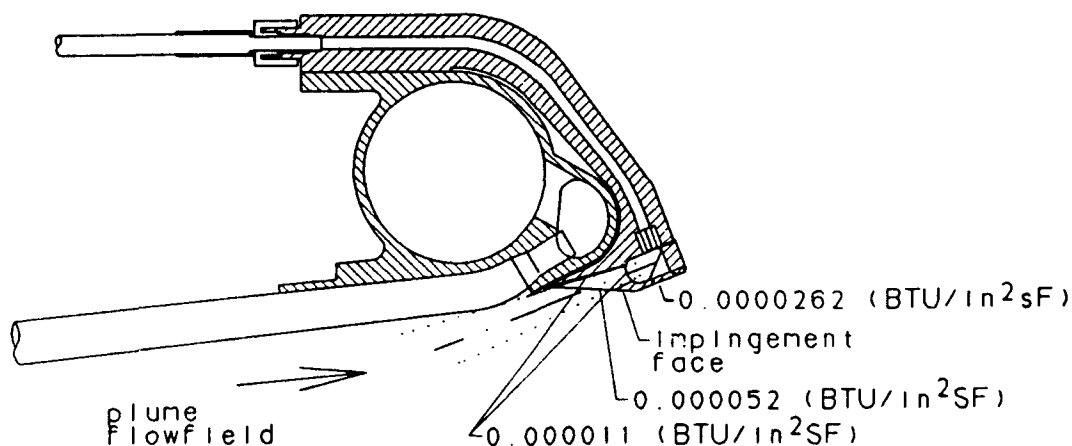


Figure 38. Convective Heat Transfer Coefficient Boundary Conditions used in Finite Element Analyses.

Predicted steady state temperature contours for the aluminum and copper probes are shown in Figures 39 and 40 respectively. These analyses assume that a heat transfer agent is used between the probe and manifold mating surfaces, and that contact occurs on the entire flat mounting face shown in Figures 32 and 33. If higher thermal contact resistance is encountered in service, the conservatism in the thermal design will be reduced.

The degree of contact between the aft manifold and probe was varied to simulate the worst case where thermal contact is limited to the region around the two bolts as compared to contact across the entire mounting face. The peak temperature increased from 1187 to 1470° R (659 to 817K) for the aluminum probe and from 713 to 1003° R (396 to 557K) for the copper probe. The aluminum peak temperature approaches its melt temperature which shows the importance of contact area. Without adequate heat transfer, the probe could fail thermally.

The models with heat transfer only near the bolts that were shown in Figures 41 and 42, were used for thermal/stress analyses since temperature gradients in the manifold for these models were greater than if a large contact area was used.

#### Probe Transient Thermal Analysis

Before engine start, the aft manifold is at roughly ambient temperature. Following engine start, the probe transfers heat to the aft manifold which is at ambient and latter at cryogenic temperatures. The possibility exists for an overshoot in the probe peak temperature. A transient heat transfer analysis was performed to determine the severity of a potential overshoot.

The minimal contact area FE mesh from the steady state analysis was used for a transient analysis. The aft manifold was started at ambient. The inner surface was dropped to 36° R (20K) upon engine start. Gas side convection was applied at engine start and maintained constant throughout the run.

Figure 43 shows the transient temperature response for the region of the probe which protrudes furthest into the plume. The steady state temperature is 1332° R (740K). No overshoot is predicted.

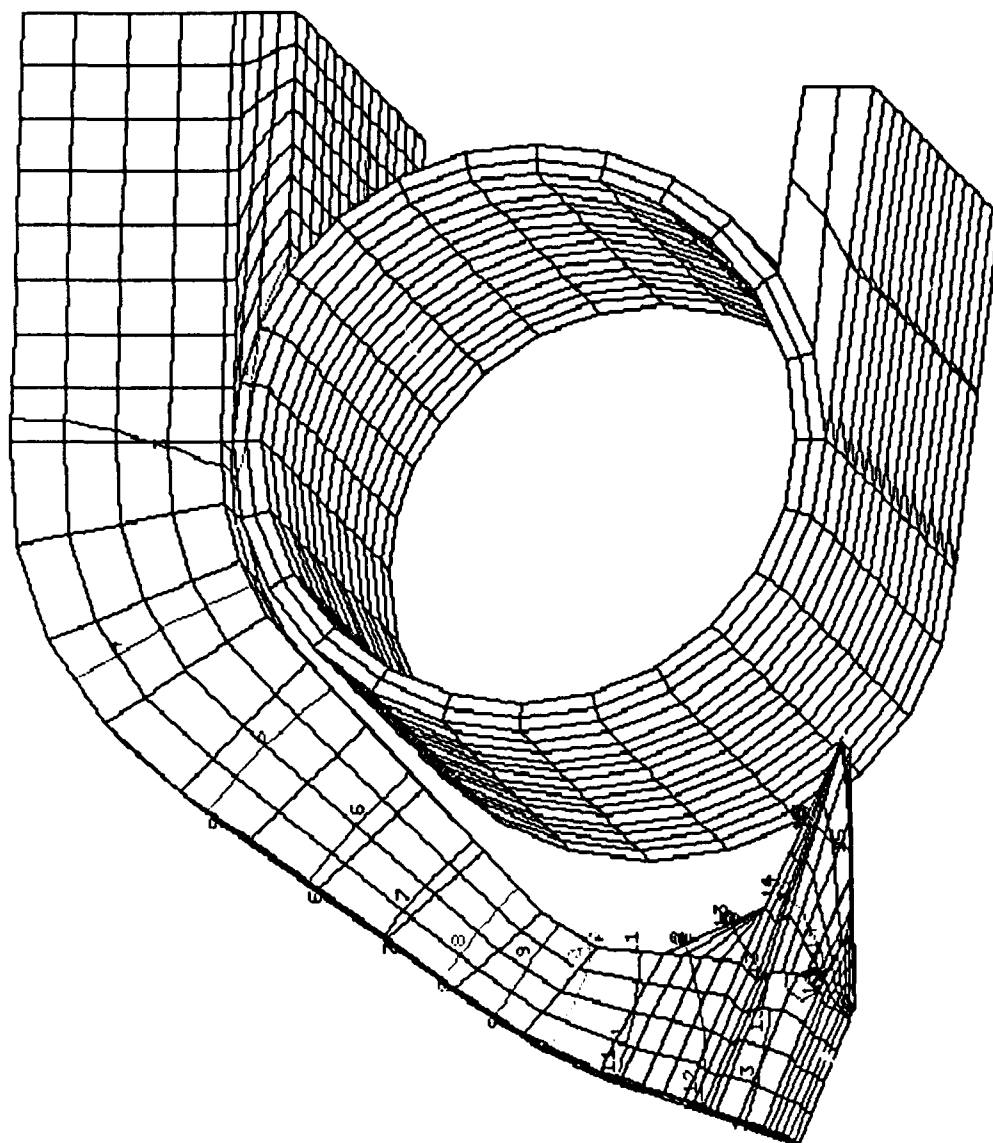
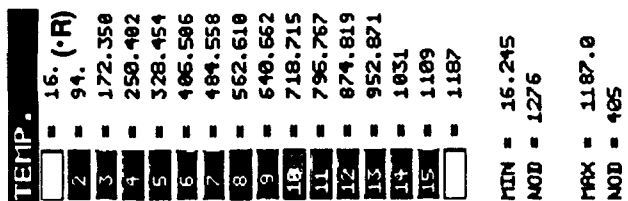


Figure 39. Steady State Temperature Contours for the Aluminum Probe with Maximum Contact Area.

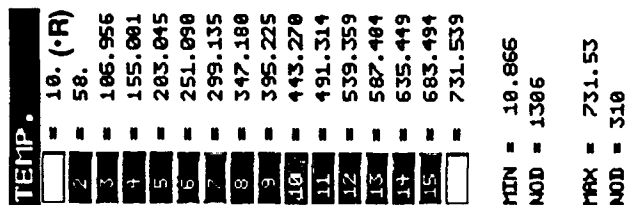


Figure 40. Steady State Temperature Contours for the Copper Probe with Maximum Contact Area.



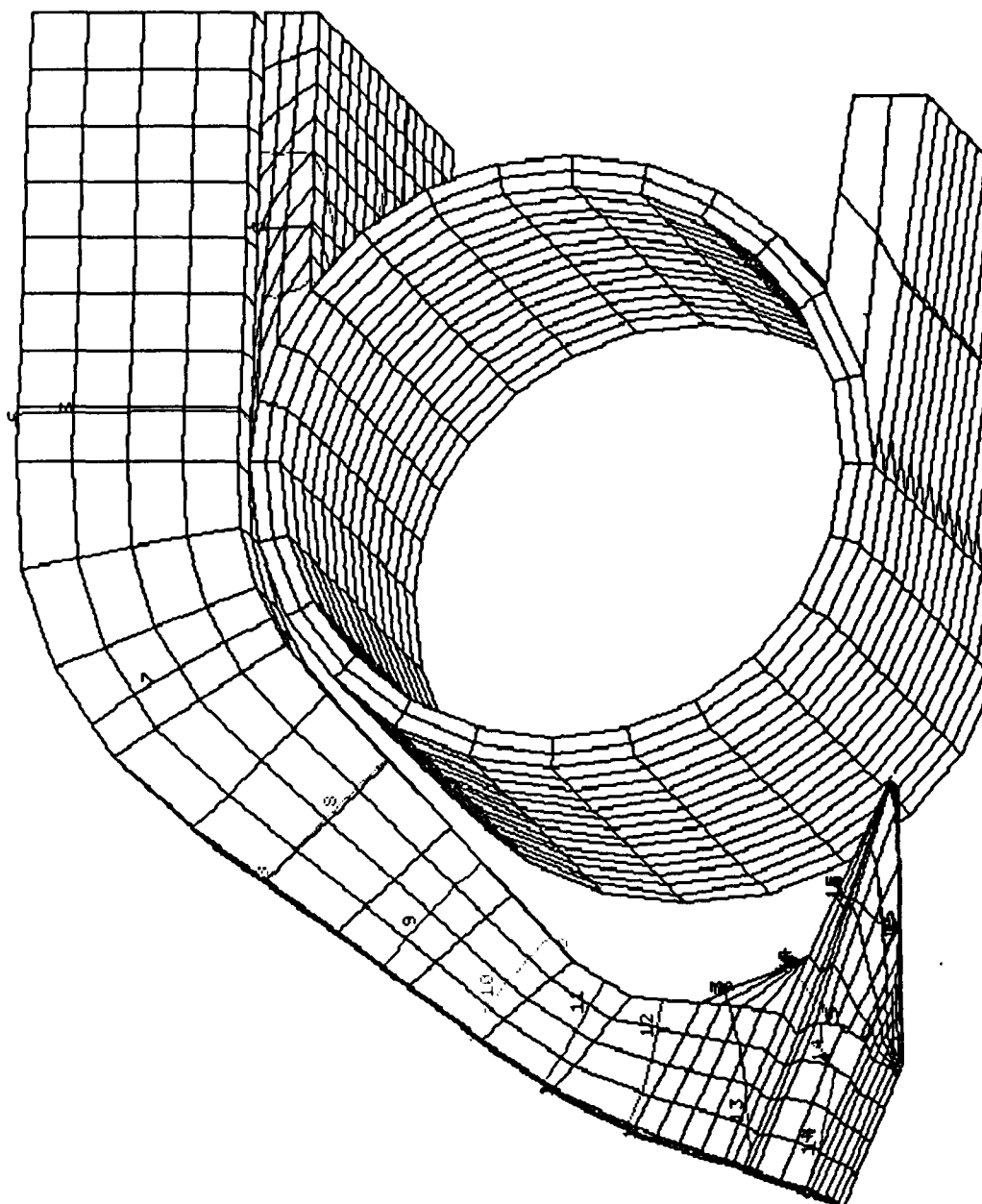


Figure 41. Steady State Temperature Contours for the Aluminum Probe with Contact Limited to Bolt Region.

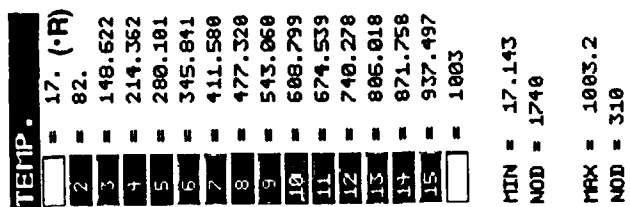
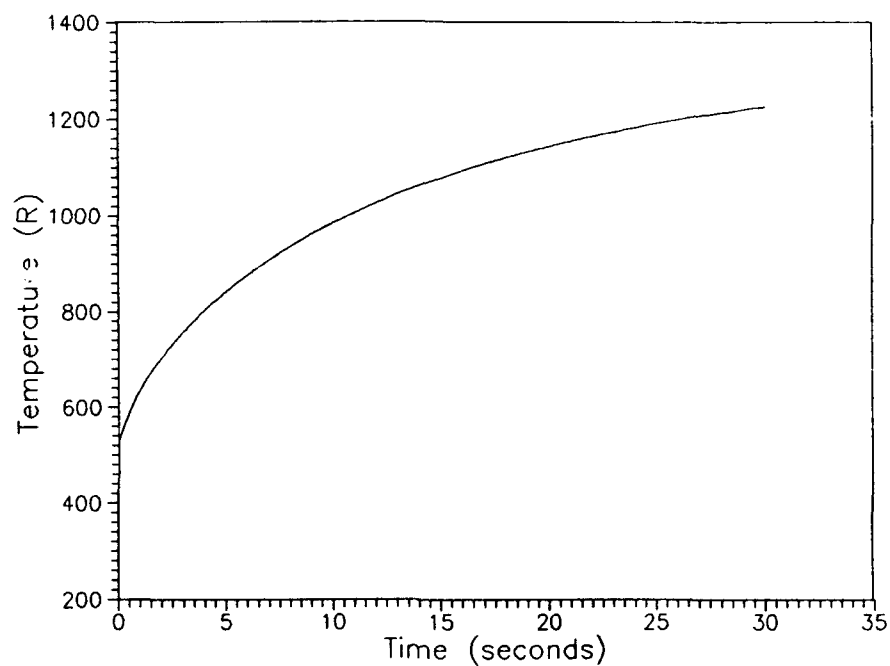


Figure 42. Steady State Temperature Contours for the Copper Probe with Contact Limited to the Bolt Region.



**Figure 43. Optic Probe Transient Temperature Response for Site with Maximum Protrusion into the Flowfield.**

### Probe Thermal/Stress Analyses

The steady state temperature field for the model with minimal contact area (Figure 41) was used to determine the stress levels which result from differential expansion. The system was assumed to be stress free at ambient conditions. As shown in Figure 44, differential expansion produces compressive stresses in the aft manifold near the flange mating with the manifold hydrogen duct. Compressive stresses of approximately 20,000 psi (138 MPa) were predicted in the aft manifold. Since the heat load and contact area for the copper and aluminum probes is similar, the resultant thermal stresses will be similar.

### Probe Static Stress Analysis

A static 7500 g acceleration was imposed in analysis of the two probe designs. The acceleration was selected at a 45-degree angle to the engine axis so that the largest bending moment on the probes could be determined. Figure 45 shows the copper probe has a peak bending stress of approximately 70,000 psi (483 MPa). This stress is substantially above the yield strength of Zr-Cu so the probe would fail. The aluminum probe bending stress is approximately 16,000 psi (110 MPa) at the extremes as presented in Figure 46, which is less than the 28,000 psi (193 MPa) yield strength of 6101. The aluminum probe will remain elastic.

Two factors contribute to the large difference in bending stress for each design: 1) the area moment of inertia for the aluminum probe is greater than the copper probe in the region where the peak bending moment occurs; and 2) the mass moment of inertia for the copper probe is larger than for the aluminum probe.

The bending moment generated by the probe produces stresses in the aft manifold wall. Bending stresses of approximately 15,000 psi (103 MPa) were predicted in the aft manifold with the aluminum probe attached. These stresses were approximately 17,000 psi (117 MPa) with the copper probe attached.

UON RISES  
 1 = 0.00000 (psi)  
 2 = 5667  
 3 = 13333  
 4 = 20000  
 5 = 26667  
 6 = 33333  
 7 = 40000  
 MIN = 75.647  
 MOD = 756  
 MAX = 66068.  
 MOD = 37

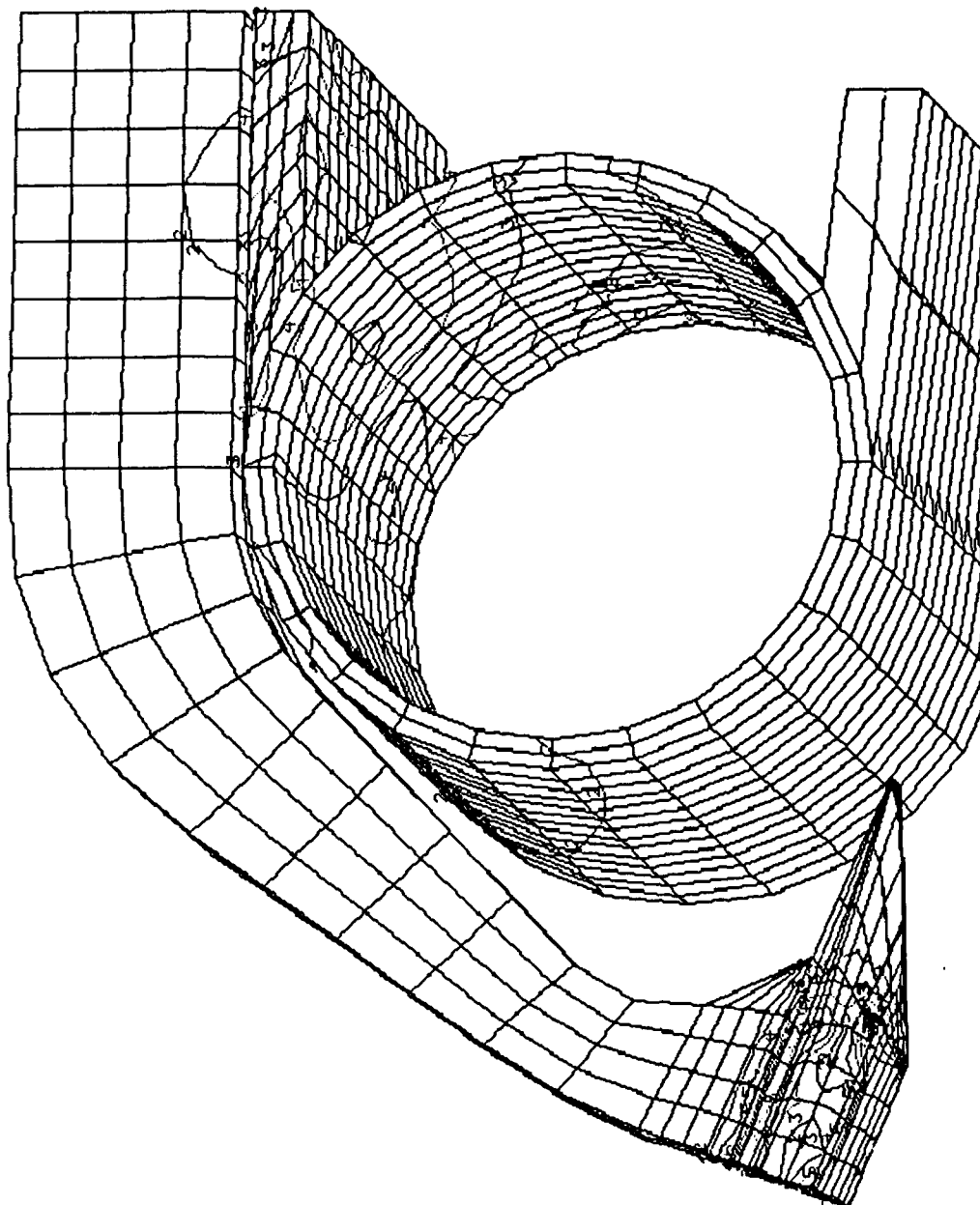


Figure 44. Thermal/Stresses in the Aft Manifold Resulting from the Probe Thermal Load.

**UON MISES (psi)**  
 1 = 33.982  
 2 = 22212  
 3 = 44391  
 4 = 66569  
 5 = 88747  
 6 = 110925  
 7 = 133104  
 MIN = 33.982  
 MOD = 352  
 MAX = 133103  
 MOD = 1017

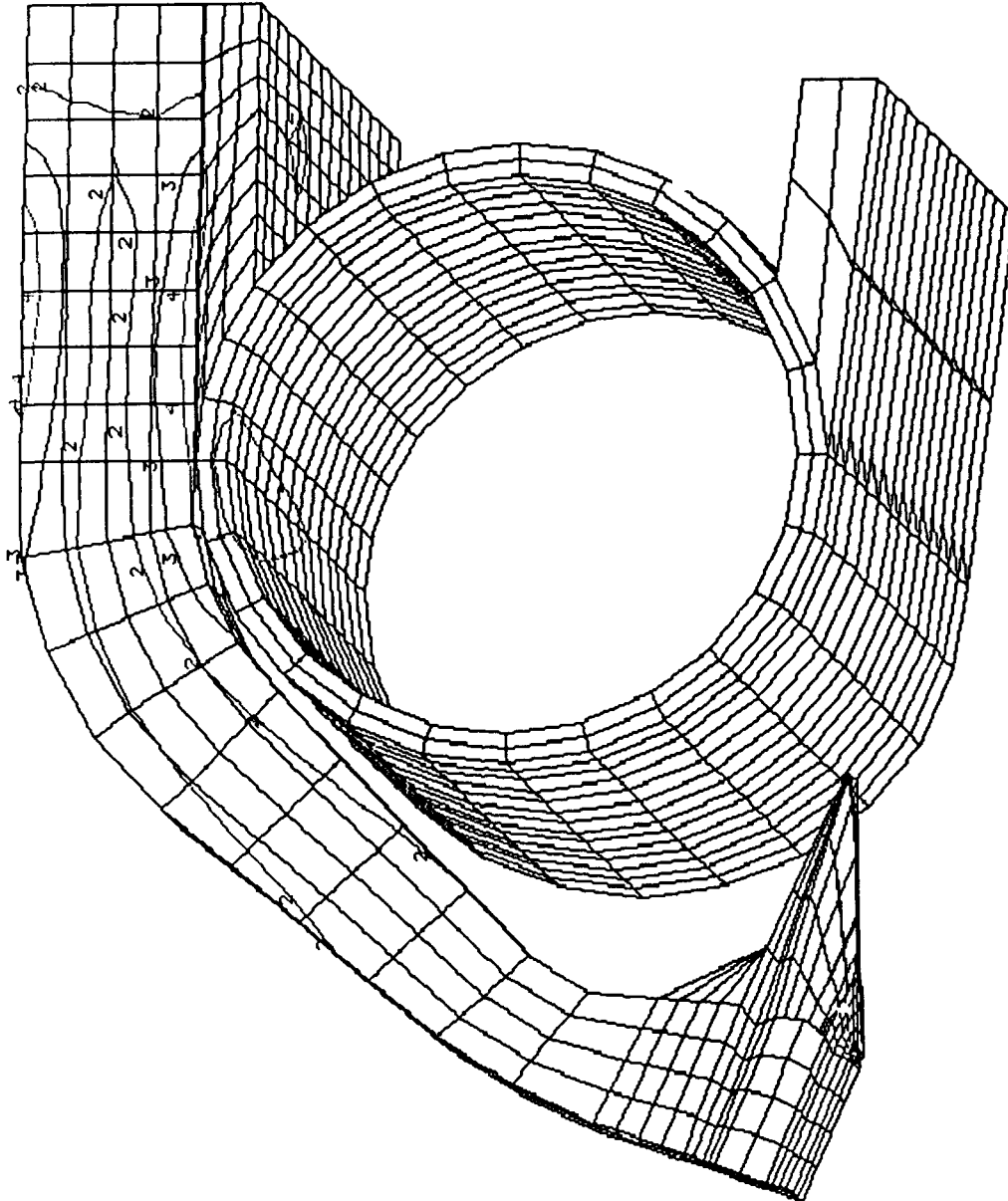


Figure 45. Bending Stresses in Copper Probe Resulting from 7500-g Static Acceleration.

UON HISES	
1	= 0.00000 (psi)
2	= 5000
3	= 10000
4	= 15000
5	= 20000
6	= 25000
7	= 30000
MIN = 226.82	
MOD = 9	
MAX = 39537.	
MOD = 884	

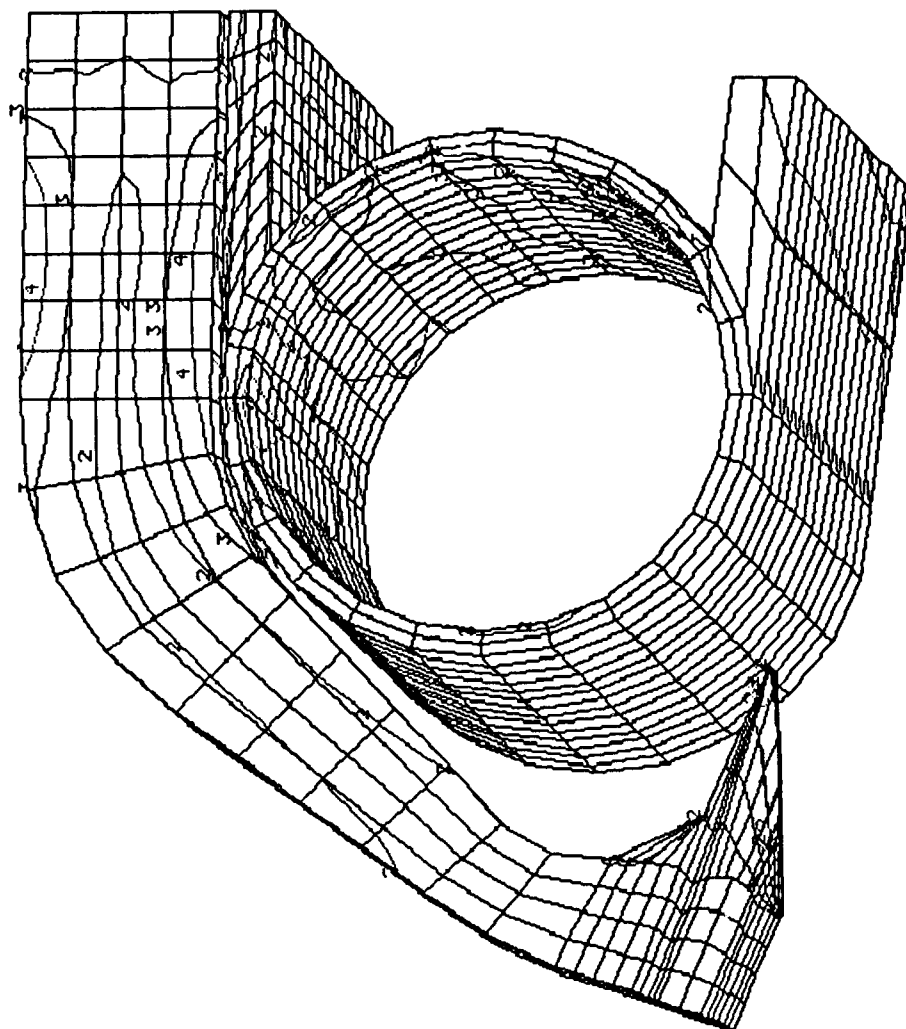


Figure 46. Bending Stresses in Aluminum Probe Resulting from 7500-g Static Acceleration.

## Probe Modal Analysis

Modal frequencies (eigenvalues) were calculated during the random vibration analysis. The frequencies were calculated for the probe attached to a section of the aft manifold and for a bare probe that was rigidly constrained at the mounting interface. Flexing in the aft manifold flange decreases the resonant frequencies relative to the rigidly attached probe. Only the first mode was calculated for the attached probe because model symmetry allows only the first bending mode. Tables 6 and 7 show the resonant frequencies for aluminum and copper probes, respectively.

Table 6. Natural Frequencies for Aluminum Probe

Mode	Frequency (attached to aft manifold) (Hz)	Frequency (bare probe) (Hz)	Description
1	1584	2073	Bending toward engine centerline
2	-	2179	Side-to-side bending
3	-	5589	Torsion and bending toward engine centerline
4	-	6012	Torsion and side-to-side bending

Table 7. Natural Frequencies for Copper Probe

Mode	Frequency (attached to aft manifold) (Hz)	Frequency (bare probe) (Hz)
1	913	818
2	-	828
3	-	2667
4	-	2738



## Random Vibration Stresses

Random vibration induced stresses were analyzed using complete probes to determine R.M.S. Von Mises stresses with contributions from multiple modes. Also analyses were performed using half sections of each probe attached to a section of the aft manifold. Due to imposed symmetry boundary conditions, only the first mode of vibration was allowed for the combined probe/manifold models. This is the mode which induces the greatest bending stresses in the aft manifold. The power spectral density for "Section C" (nozzle assembly) obtained from the SSME Structural Loads Criteria document was used as the excitation input. First the R.M.S. displacements are calculated, and then the R.M.S. stresses are determined using these displacement values. Random vibration induced Von Mises stresses were roughly 1700 psi (12 MPa) for the aluminum probe and 6500 psi (45 MPa) for the copper probe. Figures 47 and 48 show random vibration induced stresses in the aft manifold were 1500 and 4500 psi (10 and 31 MPa) for aluminum and copper, respectively. These low random vibration induced stresses are inconsequential for the probes and aft manifold.

## Aft Manifold Stresses

The aft manifold has stresses induced by many load sources. The primary loads and calculated stresses are presented in Table 8. Stresses were extracted from FE analyses which modeled the optic probe attached to the aft manifold. For random vibration and transient acceleration cases, the aft manifold was considered massless so that only stresses resulting from accelerations acting on the probe were evaluated.

The 6500 psi (45 MPa) liquid hydrogen pressure produces tensile hoop stresses in the aft manifold of approximately 60,000 psi (414 MPa). Asymmetry in the aft manifold due to two flanges causes variations in the stress levels. The hydrogen pressure induces tensile stresses along the manifold axis of roughly 29,000 psi (200 MPa).

Significant distortion of the aft manifold is observed during engine starts. The engine nozzle exhibits quasi random bell mode bending. Visual observations of roughly 6 inch (15 cm) changes in diameter have been noted. For this degree of mechanical distortion, bending stresses were calculated at 60,000 psi (414 MPa) using a 1/4 sector model of the aft manifold with symmetry boundary conditions imposed at each end. Note that the tubes forming the nozzle were not included in the model; therefore, the stress enhancement caused by the joining discontinuities in the aft manifold was not modelled.

**UON HISES**  
 = 2.979 (psi)  
 2 = 369.  
 3 = 735.  
 4 = 1101  
 5 = 1467  
 6 = 1833  
 7 = 2200  
 MIN = 2.979  
 NOD = 229  
 MAX = 2199.6  
 NOD = 1268

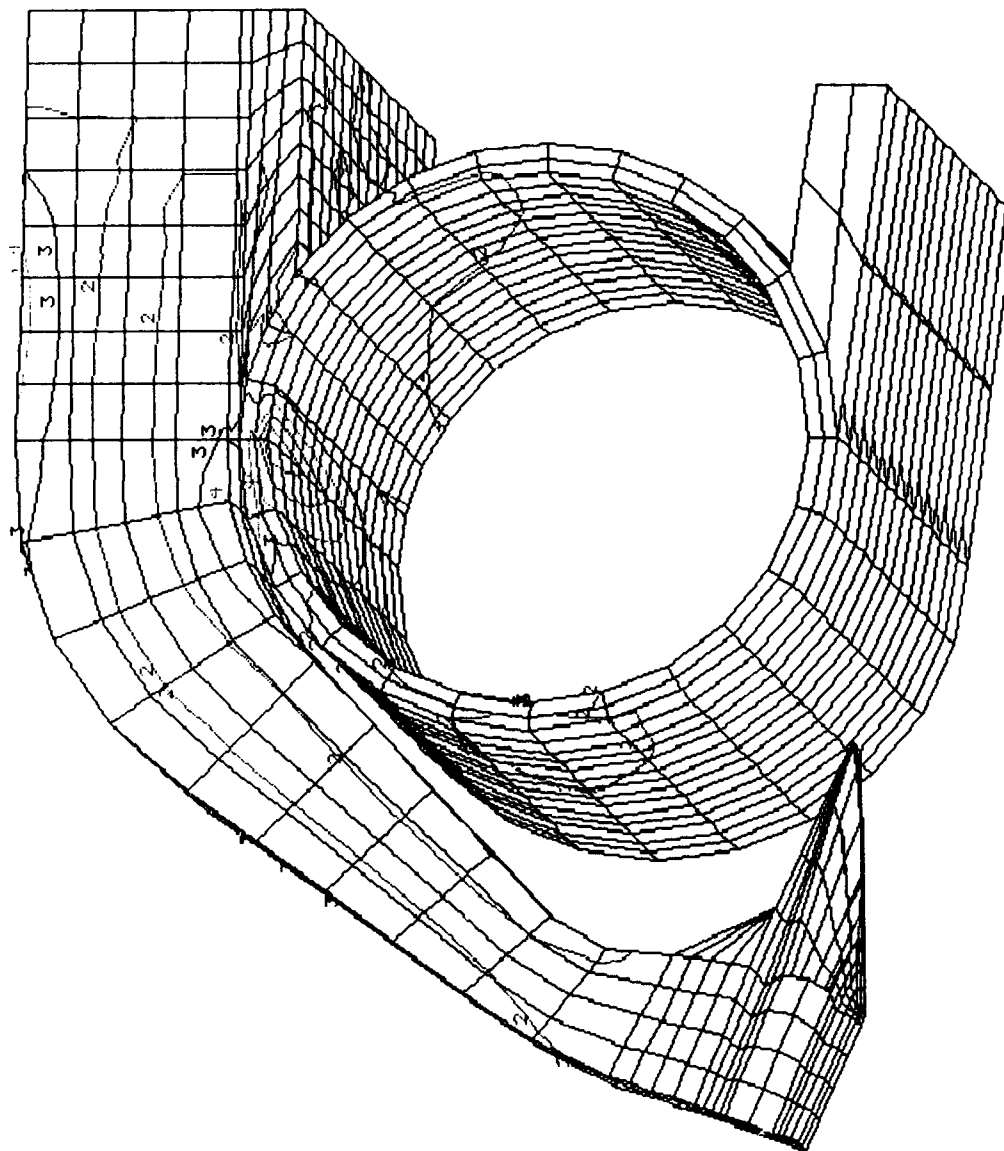


Figure 47. Stresses from Aluminum Probe Random Vibration.

UON MISES	
1	= 7.636 (psi)
2	= 1631
3	= 3254
4	= 4876
5	= 6499
6	= 8122
7	= 9745
MIN = 7.636	
NOD = 1	
MAX = 9745.3	
NOD = 1141	

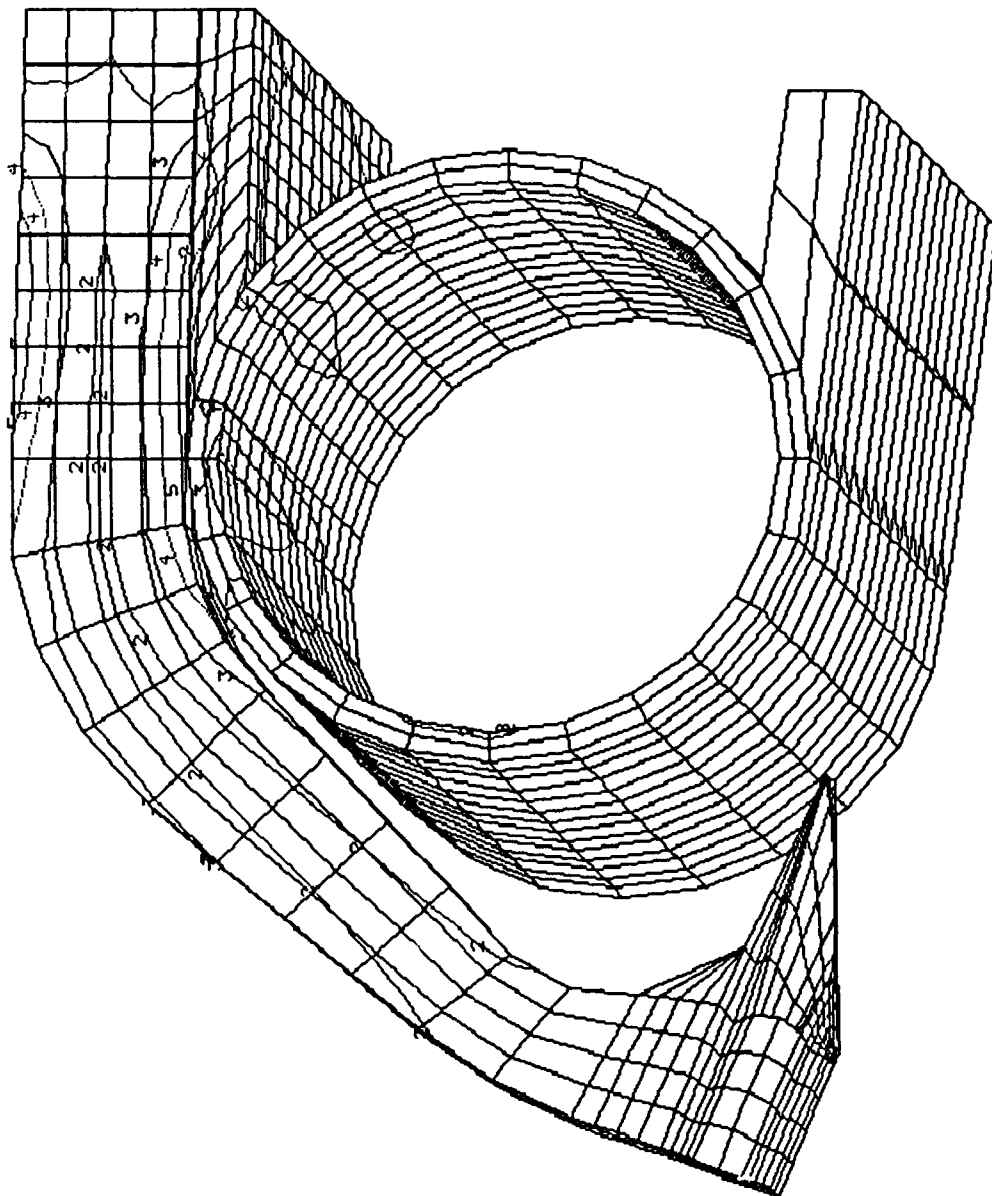


Figure 48. Stresses from Copper Probe Random Vibration.

Differential expansion, caused by temperature gradients, causes stresses in the aft manifold. Temperature gradients are produced in the manifold flange since this is the primary cooling path for the probe. Local flange temperatures surrounding the probe contact area are higher than the rest of the aft manifold which causes compressive thermal stresses in aft manifold wall.

Table 8. Stresses in the Aft Manifold Resulting from Various Loads.

Load	Direction	Amplitude (psi)	Tension/ Compression
Hydrogen Pressure (6500 psi)	Around aft manifold axis	60,000	Tension
	Along aft manifold axis	29,000	Tension
Thermal Stresses	Circumferential	20,000	Compression
	Along aft manifold axis	20,000	
Startup Bending Distortion	Along aft manifold axis	80,000	Tension
7500 g Transient Acting on Probe	Circumferential	15,000 Al	Tension/
		17,000 Cu	Compression
Random Vibration	Circumferential	<1000 Al	Tension/
		4500 Cu	Compression
Plume Pressure	Along aft manifold axis	10,000 est.	Tension

The aft manifold is fabricated from Inconel 718. It has an ambient yield strength of 172 ksi (1180 MPa). During the engine start transient, the combination of pressure and bell mode distortion will produce tensile stresses in the direction of the aft manifold axis (azimuthal around the engine axis) of approximately 110,000 psi (758 MPa). Pressure and transient accelerations will result in tensile stresses of roughly 45,000 psi (310 MPa) circumferentially in the aft manifold. The combination of these two stresses will not produce yielding in the aft manifold.

In summary, the probe induces thermal stresses, which are compressive locally around the mount region and tensile further away. These stresses do not significantly increase the tensile stresses in the manifold or flange. Random vibration induced stresses are insignificant. Circumferential stresses from bending during the start transient are the most

significant stress in the aft manifold induced by the probe. Induced tensile/compressive stresses of 15,000 psi (103 MPa) aluminum probe and 17,000 psi (117 MPa) copper probe pose negligible risk to the aft manifold. Once the start transient is completed, the manifold stresses drop below 100,000 psi (690 MPa) which provides a large safety margin.

#### Engine Throat/Nozzle Optic Probe Analysis Summary

Two design options for the engine throat/nozzle optic have been presented, a copper design which has excellent thermal properties and an aluminum probe with superior mechanical properties. Both probes are expected to operate without damage on the SSME. Properties of the copper and aluminum probes are compared in Table 9.

The high transient acceleration is the principal concern with the copper probe. It is not clear from the SLC document whether these accelerations may be expected at the aft manifold since Zone C encompasses the entire nozzle assembly. A 7500-g acceleration is extremely high, and it is not clear what mechanism might cause such a high acceleration other than shock waves in the liquid hydrogen. Generally, flexible structures such as the nozzle do not sustain or propagate such high accelerations. The copper probe, which will withstand more than 5,000 g, remains a good candidate for experimental validation on the TTBE.

The aluminum probe analysis shows that peak temperatures can approach the upper design limit for aluminum. Since conservative convection coefficients and the upper limit for stagnation temperature were used in the thermal analysis, the probe peak operating temperature is expected to be lower than predicted.

The analysis shows the probe poses negligible risk of damage to the aft manifold or engine. Stresses in the aft manifold are less than half the yield strength during main stage operation.

Table 9. Comparison of Operational Properties for the 6101 Aluminum and Zr-Cu Designs.

Feature	Units	Zr-Cu	6101 Al
Peak Temperature	K	396	660
Peak Temp / Melt Temp		0.3	0.74
First Resonant Frequency	Hz	913	1584
Peak Stress from Static 7500 g Accel.	MPa	482	110
Peak Stress/Yield Strength		1.8 (yields)	.57 (elastic)
Weight	gm	113	50
Fabricability		Fair	Good

#### 2.2.5 Subtask 2.5 Spectrometer Interface

Custom optical cables may be fabricated, tailored to each spectrometer interface, using the detachable fiberoptic cable feature. Fiberoptic cable vendors have common terminations available such as round-to-slit transitions for use with grating spectrometers, SMA connectors, and universal "rod" terminations.

For initial engine mounted optic testing, the two candidate spectrometers are a commercial OMA and the Fabry-Perot Interferometric Spectrometer. A round-to-slit transition is recommended for use with the OMA. An SMA termination is recommended for the interferometer. SMA connectors provide a logical development path toward a flight system because they are available with built-in seals and are compact.

### 2.2.6 Subtask 2.6 Alignment System

The alignment system is used to insure that the engine mounted optic is installed with the rocket engine throat centered in its field-of-view. To do this, a backlighting system is planned. A helium-neon laser will supply the light source for backlighting. The laser beam will be sent through the fiberoptic cable from the spectrometer termination. Light passing through the fiber will be defocused at the probe objective lens forming a cone of light illuminating the approximate field-of-view for the engine optic. The laser backlighting system is shown in Figure 49.

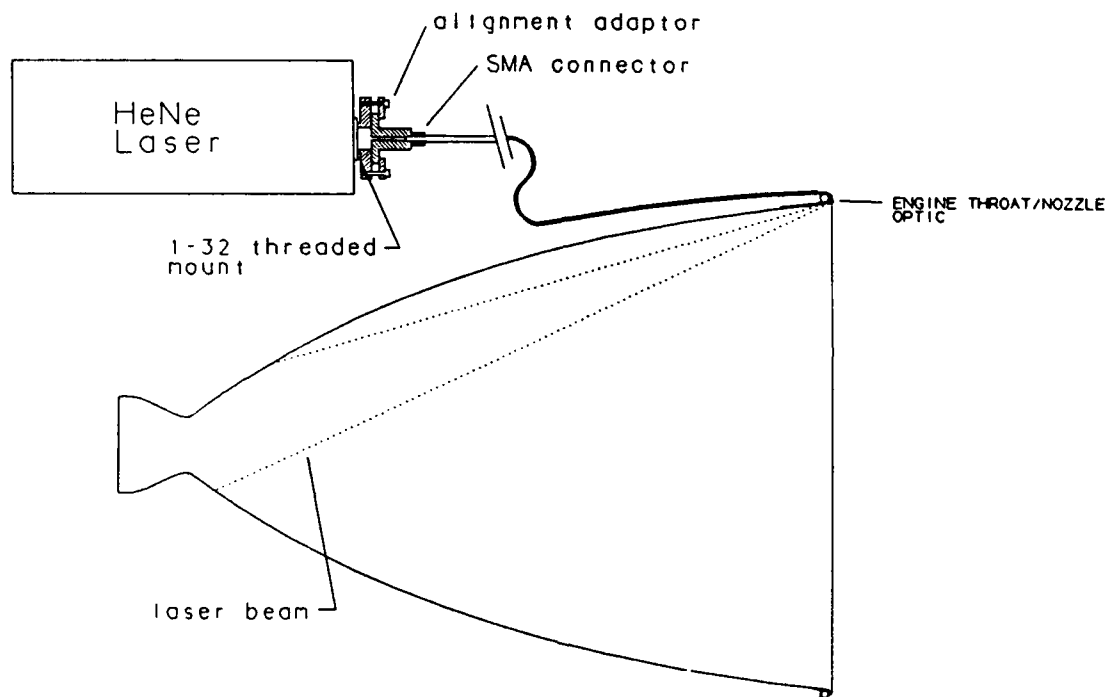


Figure 49. HeNe Laser Backlights Optic System to Check Probe Alignment.

Starting with a 5mW HeNe, losses from insertion, absorption in the fiber, surface losses at the objective lens, and reflective coating losses will result in approximately 1.8mW exiting the objective lens. The field-of-view at the throat plane will be approximately 500-mm in diameter. This provides 0.61 ft-candles ( $6.5 \text{ lumens/m}^2$ ) at the exit plane. To the human eye, this projection will be visible if the test stand is darkened, but may not be

visible in the daylight. If necessary, visibility can be enhanced by placing a target inside the SSME.

A 5mW HeNe is a Class IIIb laser meaning it can cause permanent eye damage. The maximum permissible exposure (MEP) as defined in ANSI Z 136.1-1980 is  $1 \cdot 10^{-3}$  watt/cm<sup>2</sup>. This flux exists for light exiting the probe up to 7 cm from the objective lens. Due to the contour of the SSME, when the beam is 7-cm from the objective lens, the center of the beam is 1.2-cm from the nozzle surface which means it is physically improbable that direct eye exposure to the beam can occur once the probe is mounted on the engine. Since this is not so prior to installation, standard ANSI safety practices should be enforced. When the probe is mounted on the engine, a Class II system will exist while no reflective tools are used near the probe which could turn the focusing beam toward personnel.

### **2.3 Subtask 3: Development Plan for Fabrication & Testing**

A plan was prepared for fabrication and test of the Zr-Cu and 6101 aluminum probe designs on the TTB. The effort includes fabrication experiments to develop procedures for forming the components. Probes are then fabricated and subjected to a series of environmental tests prior to installation on the NASA TTBE. A schedule proposed to complete the optic probe design, fabrication, and testing is shown in Figure 50.

#### **2.3.1 Nozzle Optic Fabrication and Check-Out**

1) Manufacturing experiments- Mechanical fabrication and bonding parameters will be defined and certified by experiment.

Probe fabrication requires a heating and bending step to be done after rough fabrication is completed. This operation produces a curved passage through the probe for the fiberoptic. Once bending is completed, the part is heat treated and then final machined. The heating and bending step will require experiments to develop a reliable procedure. These experiments will consist of building bending mandrels to select the final bend shape (which overbends the part because of elastic springback). Rough machined parts will be bent, stress relieved, and then sectioned. The hole location and change in hole cross section will be measured. This data will be used to adjust the contour of the bending fixture as required. These experiments will be performed for both the copper and aluminum alloys.



**NAS3-25883**



**Figure 50.**

A bonding technique to mount the lens into the probe body will be developed. Lens cavities will be drilled into copper and aluminum alloy test specimens. The gap between the lens and cavity wall will be varied. Fused silica rods, simulating the lenses, will be bonded into the cavities. The required "silk screen" fixtures and applicators will be built to provide repeatable application of adhesives. After bonding and curing is complete, the test specimens will be heated in an oven to the upper limit of the expected operating temperature. Bond strength will be evaluated at high temperature and ambient conditions.

A mockup of the collet region, used to anchor the fiber tip, will be built. This collet will be used to evaluate the fiber tip clamping capability to test the alignment and tolerancing.

2) Fabrication Drawing Package- A complete fabrication drawing package will be prepared for the aluminum and copper probes, fiberoptic cable, lens, clamping collets, alignment fixtures, and fabrication bending fixtures.

3) Procurement Package- A complete procurement package shall be prepared including specifications for the fiberoptic and lens, instructions for component fabrication, and inspection requirements.

4) Quality Assurance- Procure and inspect components. Assemble and align per specifications.

5) Verification Testing- Experiments will be conducted to test the engine throat/nozzle optic performance before and after environmental testing. The fixtures and procedures used during the experimental program will be used for acceptance testing of engine optics that will be installed and tested on TTB.

#### a) Field-of-View

Using a light source with known intensity, map the probe field-of-view by traversing the light source and measuring signal strength transferred to a detector. Using a lamp source, check field-of-view at wavelength extremes, i.e., Cu 324-nm and Cr 425-nm. Lamp sources may be hollow cathode lamps with narrow band filters so that only a single line is transmitted and the neon lines are blocked. Mount optic in a bracket, a fixed distance between the optic and source, and traverse source throughout a coordinate system making accurate relative position measurements between the optic and source.

Performed this test before and after environmental experiments. Use the resulting fixtures and setup for the remaining optical experiments.

#### b) Transmission Efficiency

Measure optical system transmission efficiency by measuring the flux arriving at optic and the optical power transmitted to a detector. Check transmission efficiency at wavelength extremes.

#### c) Backlighting Alignment

Use backlighting system to illuminate field-of-view coordinate field. Check to see that the back illumination matches the field-of-view. Check intensity of back illumination to be sure it will be visible on the engine test stand. See what special requirements might exist such as a target in the chamber, darkening of area, etc.

#### d) Water Deluge Test

Submerge engine optic into distilled water for a few minutes. Remove and dry the optic using dry nitrogen. Look for evidence of water leakage into the probe. Check optic transmittance to see if it has decreased.

#### e) Vibration Testing

Install the engine optic and cable on a bracket that simulates a section of the aft manifold and drain line. Perform vibration testing using the design power spectral density for the shaker table control function. Inspect cable and engine optic for signs of mechanical damage or changes in alignment. During the vibration testing, place a light source in the optic field-of-view and record transmitted intensity throughout the vibration testing.

#### f) Temperature Cycling

Mount engine optic (with fiberoptic cable attached) onto a mock aft manifold. Use the specified heat transfer agent at mounting interface. Submerge assembly in liquid nitrogen. Remove it from the  $LN_2$  and then heat optic to  $250^\circ C$ . Visually inspect optic for damage. Recheck the probe optical alignment and transmittance.

#### g) Heat Transfer into a Mock Aft Manifold

Mount optic assembly onto a cooled mock aft manifold with the specified heat transfer agent at the interface. Apply a heat flux to the lens end of the optic simulating the plume convective heat transfer (using either a hot gas source or resistance heater). Measure the probe surface temperatures near the lens and near the aft manifold. Repeat this experiment with a partial application of the heat transfer agent and without heat transfer agent.

### 2.3.2 Test Stand Instrumentation Packaging Design (Optional)

Design the instrumentation and support equipment required to test two engine optics on the TTB engine with one connected to an OMA and the other to the breadboard F-P interferometer.

#### 1) Fiberoptic Cable Routing

Design or specify an attachment system restraining the fiberoptic cable to the specified engine drain lines. Select a fiberoptic cable route so that the cable is not damaged and does not interfere with engine or test stand operation. Resolve mounting details with MSFC.

#### 2) Spectrometer Location and Mounting

Identify locations on the TTB test stand to install the OMA and F-P that is near the engine. Decide how the enclosures will be anchored to the test stand, where electrical power is available, routing for signal cables, etc.

#### 3) Spectrometer Explosion Proof Packaging

Design/specify explosion proof enclosures for the OMA and F-P spectrometer including a water tight and gas tight case, fiberoptic cable, power, and signal cable feedthroughs, vibration mounts, nitrogen purge, grounding provisions, etc.

#### 4) Test Stand Setup, Calibration, Testing Procedures

Write procedures for the electronics and optics installation on the test stand, optics alignment, electronics calibration, system checkout, data acquisition, and operation.

#### 5) Experimental Hardware Drawings and Specifications

Prepare drawings for explosion proof packaging, feedthroughs, mounting fixtures, and cabling diagrams. Prepare specifications for equipment.

### 2.3.3 Test Stand Design Review and Approvals

Provide technical support and planning throughout the approval process leading to integration of nozzle mounted optic assemblies on the TTBE. Prepare and present design information required to obtain approval for testing on TTB. Assist Marshall Space Flight Center in preparation of an engineering change proposal (ECP) and contractor change board (CCB) review. Prepare a written test plan and support the Marshall Space Flight Center test readiness review (TRR).

### 2.3.4 Test Stand Instrumentation Procurement, Assembly, and Inspection

Purchase and assemble the equipment required for the TTB experiments. Test the equipment using simulated test stand environments before shipment to MSFC.

1) Procure enclosures.

2) Mount OMA and Interferometer into enclosures including wiring, installing nitrogen purge, any grounding requirements, etc.

3) Test F-P and OMA equipment in the enclosure by mounting enclosure on a shaker table and applying test stand vibration spectra. Operate both spectrometers during the shaker test to evaluate vibration sensitivity.

4) Design, fabricate, and assemble narrow band radiometers to measure intensities for the 404-nm and 766-nm potassium lines from the Mach disc region of the plume. This data will be compared to throat plane measurements for performance verification.

### 2.3.5 TTBE Nozzle Optic Testing

Provide on-site support during the integration of the nozzle mounted optic with the TTBE and on-site instrumentation. Provide alignment and perform the necessary check-out tests to verify the optic system performance prior to hot-fire testing. Demonstrate the alignment and check-out procedures and provide written documentation of the same to the TTBE system engineers.

Perform post-test data reduction and interpretation. Use the spectrometer data sets to determine the background radiation and atomic emission intensity within the SSME.

- 1) Reduce OMA and F-P spectrometer data to determine molecular band intensities, continuum radiation, and the K 404-nm intensity. Compare the results to predicted values for emissions from within the SSME chamber. Compare the engine emission data to OMA data and narrow band radiometer data obtained looking at the plume. Reduce F-P data for K 404-nm line to determine line FWHM.

- 2) Compare thermocouple data from engine optic with calculated values. Back calculate heat fluxes that existed during the experiment.

Prepare final report and recommendations including a post-test assessment of the system mechanical and optical performance.

## **3.0 CONCLUSIONS**

Two engine throat/nozzle optic probe engineering designs have been completed. The designs were subjected to detailed thermal and mechanical analyses to decide if the probes would survive in the SSME environment and whether the probes posed a risk to the SSME aft manifold. Based on the design and analysis results, both probes are expected to perform as required. The copper probe provides a good thermal margin which accommodates uncertainties in the flowfield analysis. The copper probe has excellent structural margin during engine operation but there is uncertainty as to its performance during the start transient. If 7500 g accelerations truly occur at the aft manifold, the probe will yield in bending and lose alignment with the required field-of-view. If the start transient accelerations are 5000 g or less, the copper probe will not yield in the start transient and will function as required. Additional start transient structural margin

can be achieved by increasing the probe cross section with the penalty of increased weight and increased loads into the aft manifold.

The aluminum probe will survive the start transient and function as required throughout engine operation if thermal loads do not exceed those defined in Section 2.2.1. These values and the thermal analyses were very conservative and should provide a worst case scenario.

#### **4.0 RECOMMENDATIONS**

Fabrication and testing of both the Zr-Cu and 6101 aluminum probes is recommended. Considering the cost of SSME firings and long, detailed process required to place hardware on the test stand, the benefits and risk reduction from testing both designs outweighs the added cost.

## REFERENCES

1. Parsons, M.L., et. al., Handbook of Flame Spectroscopy, Plenum Press, 1975.
2. Duncan, D.B., Sakabu, R., Bickford, R., "Fabry-Perot Interferometric Spectrometer, Technical Narrative #1", Contract NAS3-25624, 1990.
3. White, H.E., Introduction to Atomic Spectra, McGraw-Hill Book Company, 1934.
4. Padley, P.J., T.F.S., 56, 449, (1960).
5. Dean, J.A., Stubblefield, C.B., Anal. Chem. [34], 382, (1961)
6. Zeegers, P.J., "Recombination of Radicals and Related Effects in Flames", PhD Thesis, Utrecht, Netherlands (1966)
7. Liveing, G.D., Dewar, J., P.R.S., [30], 580, (1880).
8. Reynolds, W.C., "The Element Potential Method for Chemical Equilibrium: STANJAN", Stanford University, June 1986.
9. Duncan, D.B., Sakabu, R., Bickford, R., "Fabry-Perot Interferometric Spectrometer, Technical Narrative #2, Contract NAS3-25624, 1990.
10. Dennis, H., personal communication (1990).
11. Kays, W.M., Crawford, M.E., "Convective Heat and Mass Transfer", 2nd Edition, McGraw Hill, Chap. 15, 1980.
12. Zakkay, V., Wang, C.R., "Applications of Active Cooling to Nose Cone," ARL 73-0143, 1973.
13. Lamb, J.P., "Analysis and Correlation of Convective Heat Transfer Measurements for Open Cavities in Supersonic Flow." AIAA-80-1526, 1980.
14. Dennis, H., personal communication, 1990.





## Report Documentation Page

1. Report No.	2. Government Accession No.	3. Recipient's Catalog No.	
4. Title and Subtitle Engine Throat/Nozzle Optics for Plume Spectroscopy		5. Report Date 1 February 1991	
		6. Performing Organization Code	
7. Author(s) R.L. Bickford D.B. Duncan		8. Performing Organization Report No. Task 2.0 Final	
		10. Work Unit No. Task Order No. 2	
9. Performing Organization Name and Address Aerojet Propulsion Division P.O. Box 13222 Sacramento, California 95813		11. Contract or Grant No. NAS 3-25883	
		13. Type of Report and Period Covered Task Final Report 03/23/90 to 01/23/91	
12. Sponsoring Agency Name and Address National Aeronautics and Space Administration Lewis Research Center 21000 Brookpark Road Cleveland, Ohio 44135		14. Sponsoring Agency Code	
15. Supplementary Notes <p>This final technical report describes the work performed under Task Order No. 2 of the Development of Life Prediction Capabilities for Liquid Propellant Rocket Engines program.</p> <p>The NASA technical monitor is G. Madzsar, LeRC/500-219.</p>			
16. Abstract <p>The throat and combustion chamber of an operating rocket engine provide a preferred signal source for optical spectroscopy based safety and health monitoring. As rocket engine components experience wear or failure, metallic materials may be entrained with the combustion products. These metallic species may be detected by spectroscopic instruments enabling prognosis and response to incipient rocket engine failures as well as diagnosis of degradation. The cost benefit of failure avoidance is significant.</p> <p>An optical system for imaging the throat and combustion chamber of a Space Shuttle Main Engine (SSME) from the nozzle lip has been designed. The optical system will couple light emitted from the throat and chamber into a fiberoptic bundle for transfer to one or more spectrographic instruments. Plans were developed to fabricate and test the optical element on the NASA Technology Test Bed Engine (TTBE).</p>			
17. Key Words (Suggested by Author(s))  Liquid Rocket Engines, Plume Phenomenology, Spectroscopy, Optics, Fiber Optics Failure Detection		18. Distribution Statement  Unclassified - Unlimited	
19. Security Classif. (of this report)  Unclassified	20. Security Classif. (of this page)  Unclassified	21. No. of pages  87	22. Price